EXPLORING HIGHER-ORDER ALPHA-HELICAL PEPTIDE ASSEMBLIES FOR BIOMATERIAL APPLICATIONS

by

Monessha Nambiar

A Dissertation

Submitted to the Faculty of Purdue University

In Partial Fulfillment of the Requirements for the degree of

Doctor of Philosophy

Department of Chemistry

West Lafayette, Indiana

December 2019

THE PURDUE UNIVERSITY GRADUATE SCHOOL

STATEMENT OF COMMITTEE APPROVAL

Dr. Jean Chmielewski, Chair

Department of Chemistry

Dr. David Thompson

Department of Chemistry

Dr. Chengde Mao

Department of Chemistry

Dr. Shelley Claridge

Department of Chemistry

Approved by:

Dr. Christine Hrycyna

To Mamma, Pappa and Ani

ACKNOWLEDGMENTS

First and foremost, I would like to thank my research advisor, Prof. Jean Chmielewski. Jean has been a tremendous source of support and encouragement during my graduate career at Purdue. She has always emphasized the importance of developing a comprehensive repertoire of both hard and soft skills, ensuring that her students are well-prepared to embark on their future careers. Her creative approach to new research ideas and keen attention to detail are qualities that I greatly admire and strive to attain on my path to becoming an independent scientist. I couldn't have asked for a better mentor and will be eternally grateful for her enduring faith in me. I would also like to acknowledge all my teachers and professors at HPS, Flinders and Purdue, for contributing to my cumulative years of learning and training in the natural sciences.

I would like to thank my committee members, Prof. David Thompson, Prof. Chengde Mao and Prof. Shelley Claridge for taking the time to provide valuable feedback on my OP, seminar and dissertation. I am deeply indebted to the technical staff and support on campus – Dr. Patricia Bishop (Research Instrumentation Center), Dr. Christopher Gilpin and Laurie Mueller (Life Science Microscopy), Dr. Andy Schaber (Bindley Imaging Facility), Bridget Haley (Cell Culture Facility) and Jessica Sargeant. They were pivotal in honing my skills and improving my understanding of various instrumental techniques. I also appreciate and thank the Department of Chemistry, the College of Science and the Purdue Graduate School for providing both fellowship and teaching opportunities, as well as travel grants during my graduate school tenure.

Our likelihood of success depends just as greatly on who we spend time with as much as how hard we work. I would like to express my sincere gratitude to members of the Chmielewski research group, both past and present. To Dr. Jeremy Gleaton, for taking me under his wing and showing me the ropes of peptide synthesis. To Dr. Anna Brezden, Dr. Manish Nepal and Dr. Neha

Agrawal, for always being available to answer questions and providing constructive feedback. The camaraderie that I've shared with the current cohort - Dr. Reena Blade, Jennifer Rowe, Vallabh Suresh, Moises Morales, Ryan Curtis, Samantha Zeiders, Thomas Deitsche, Corey Johnson, Vinay Menon and Michael Jorgensen, has been truly special. I shall fondly remember the jokes, champagne toasts, 5Ks, delicious meals and conference excursions that we've experienced together.

Last but not least, I could not have come this far without my close friends and family who are scattered all over the world. Over the years, I've come to associate 'home' with the people who have shaped me to be the person that I am today. To Reena, Kwaku and Carol, for their enduring friendship and support throughout my time at Purdue. I look forward to seeing how our careers evolve and where life takes us. To Abi and Subha, for taking the time to check up on me and for answering all my whatsapp calls, despite the inconvenient time differences. Finally, to my parents and brother, who never fail to keep me rooted. They taught me to view all past events in kind-sight and use them as a driving force to realize my dreams and above all, to approach life with passion, humor and style. Thank you all for cheering me on!

TABLE OF CONTENTS

LIST OF TABLES

LIST OF FIGURES

LIST OF SCHEMES

LIST OF ABBREVIATIONS

AFM	atomic force microscopy
CD	circular dichroism
DCM	dichloromethane
DIEA	diisopropylethylamine
DLS	dynamic light scattering
DMF	N, N'-dimethylformamide
DNA	deoxyribonucleic acid
EDS	energy dispersion spectroscopy
EDTA	ethylenediaminetetraacetic acid
FBS	fetal bovine serum
FIB	focused ion beam
Fmoc	9-fluorenylmethyloxycarbonyl
HBTU	N,N,N',N'-tetramethyl-O-(1H-benzotriazol-1-yl)uranium hexafluorophosphate
MALDI-TOF	matrix-assisted laser desorption ionization – time of flight
MAXS	medium-angle x-ray spectroscopy
MeCN	acetonitrile
MeOH	methanol
MOPS	3-(N-morpholno)propanesulfonic acid
Mtt	4-methyltrityl
MTT	3-(4,5-dimethylthiazol-2-yl)-2,5-diphenyltetrazolium bromide
MWCO	molecular weight cut off
NMR	nuclear magnetic resonance
NTA	nitrilotriacetic acid
PB	phosphate buffer
PBS	phosphate buffer saline
RP-HPLC	Reverse Phase- High Performance Liquid Chromatography

RPMI	Rosewell Park Memorial Institute
SEM	scanning electron microscopy
SPPS	solid phase peptide synthesis
SWAXS	small and wide-angle x-ray spectroscopy
$t_{1/2}$	half-life
TEM	transmission electron microscopy
TFA	trifluoroacetic acid
TIPS	triisopropyl silane
T_m	melting temperature
UV-Vis	ultraviolet-visible
WAXS	wide-angle x-ray spectroscopy

Amino Acids

Alanine (Ala, A); Arginine (Arg, K); Asparagine (Asn, N); Aspartic Acid (Asp, D); Glutamic Acid (Glu, E); Glutamine (Gln, Q); Glycine (Gly, G); Histidine (His, H); Homocysteine (HCys); Isoleucine (Ile, I); Leucine (Leu, L); Lysine (Lys, K); Methionine (Met, M); Tyrosine (Tyr, Y); Valine (Val, V);

ABSTRACT

Peptides are a fundamental building-block of living systems and play crucial roles at both functional and structural level. Therefore, they have attracted increased attention as a platform to design and engineer new self-assembled systems that span the nano-to-meso scales. The rules of peptide design and folding enable the construction of suitable building-blocks to develop soft materials for biomaterial applications. Herein we present the use of the alpha-helical secondary structure to create two distinct structural motifs, namely coiled-coils and helical bundles. These peptide components can differ in size and incorporate a host of different functional moieties, the effects of which are described through their hierarchical assembly.

First, we describe the self-assembly of coiled coil oligomers (trimer and tetramer) of the GCN4 leucine zipper peptide. The trimeric coiled coil was modified with varying number of aromatic groups (one to three) along each helical backbone, to facilitate higher order assemblies into banded nano- to micron-sized structures, the formation of which could be controlled reversibly as a function of pH. In addition, the electrostatic and aromatic interactions of the peptide material were harnessed for non-covalent binding of small drug molecules, followed by their subsequent pH-triggered release. Furthermore, these nanostructures are compatible with MCF-7 breast cancer cells, making them suitable drug-delivery agents for chemotherapeutics. In the absence of aromatic modifications, the coiled-coil trimer assembles into higher-order nanotubes that can be harnessed for selective encapsulation of high molecular weight biomolecules. With an increase in oligomerization from three to four, along with a single aromatic group modification on each helix, the tetrameric coiled-coil mutant successfully demonstrates a metal-assisted two-tier structural assembly into microbarrels and spheres.

Second, we present the higher-order assembly of short tetrameric and pentameric helical bundle proteins, covalently stabilized by a belt of disulfide bridges, with metal-binding ligands at each helix termini. The addition of metals like Zn(II) and Cu(II) promote the assembly of the bundles into a 3D globular matrix, which upon thermal annealing transforms into microspheres. Additionally, these microspheres also demonstrate the metal-assisted inclusion of His-tagged fluorophores. Thus, peptide-based materials can be constructed by self-assembly of alpha-helical building blocks into systems with sophisticated, diverse morphologies and dynamic chemical properties, that can be further modulated to enhance performance for medical applications.

CHAPTER 1. ALPHA HELICAL COILED-COIL PEPTIDE MOTIFS AND THEIR HIERARCHICAL ASSEMBLY FOR BIOMATERIAL APPLICATIONS

1.1 Introduction

Over the last few decades, the field of biomaterials has rapidly evolved into the design and creation of materials that interact with biological systems. A goal for materials chemists has been to generate synthetic materials with properties comparable to or superior to those seen in nature. However, when compared to the chemical and structural complexity of a cell, man-made materials are simplistic and struggle to meet clinical expectations. Therefore, there is a need for the advancement of more complex materials that not only interact with their biological environment, but also direct the body's response for maximum restorative power. Some essential properties that determine the effectiveness of such engineered biomaterials are strength and plasticity, control over degradation, the ability to accommodate various cell types and biocompatibility.[1] The applications of these types of materials would not only encompass bio-devices, but also extend to diagnostics and drug delivery systems. However, it remains a significant challenge to generate materials with higher-order assemblies down to the atomic level that have precisely tailored chemical heterogeneities and external stimuli-responsiveness.

Biomolecular self-assembly is the underlying mechanism responsible for the creation of many structures in nature, ranging from the cell membrane, to the extracellular matrix and structures such as silk and muscle fibres.[2] These constructions comprise a wide range of building-blocks, including polypeptides.[3-7] Self-assembly is an intrinsic feature of many peptides, and therefore, there is great interest in the use of this concept to assemble materials that transition across scales from the molecular level to the micro- and macroscale. Self-assembling peptides

have thus emerged as a potential avenue for the creation of novel biomaterials.[2, 8-12] Peptides offer numerous advantages in this regard. They consist of a sequence of amino acids, and therefore, generally possess inherent biocompatibility. Furthermore, tailormade modifications can be made at the synthetic level in the form of sequence alterations, incorporation of non-natural amino acids or added chemical functionalities. But the most crucial design feature that sets them apart is their sequence-to-structure relationship, including a range of secondary and super-secondary structures.

1.2 Coiled-Coil Peptide Building-Blocks

The coiled-coil is a structural motif that comprises two or more alpha helices and appears as a common feature among many proteins that are otherwise unrelated in sequence or function, enabling and supporting a wide range of biological roles. They typically provide structural stability through a very efficient burial of hydrophobic side chains so that, for the most part, these residues are not accessed by polar water molecules. The coiled-coil domain predominantly occurs in structural proteins that have to bear considerable stress, such as keratins, tropomycin, and laminin. Initial investigations into the coiled-coil structure began with Astbury's study of various protein fibers in the 1930s with the identification of a class of proteins he termed 'k-m-e-f', for keratin, myosin, epidermin, and fibrinogen.[13-15] These proteins showed strong meridional arcs of spacing 5.15 Å, indicating that the alpha helices are distorted to follow a long-pitch. It was only following Linus Pauling's discovery of the alpha helical structure two decades later, that Crick observed alpha helices wrapping together at a 20^{o} angle with close packing interactions of the hydrophobic residues.[16] He demonstrated the repetition of these interactions every seven residues or two turns of the alpha helix, thus accounting for Astbury's earlier observation. Crick coined the supercoil of α-helices, a 'coiled-coil' (Figure 1.1 A).[17] This result was independently confirmed that same year with the model of α–keratin proposed by Pauling and Corey.[13, 16, 18, 19]

1.2.1 Sequence and Structure

Coiled coils are characterized by contiguous heptad repeats that have the sequence form $(a\text{-}b\text{-}c\text{-}d\text{-}e\text{-}f\text{-}g)_n$ where in at least three quarters of the positions *a* and *d* are occupied by apolar or hydrophobic residues (Figure 1.1 B). This follows from the apolar residues being placed three and four residues apart to accommodate the 3.6 residues per turn in a right-handed alpha helical structure[16]. The thermodynamic driving force of the coiled-coil folding is the hydrophobic effect which causes the apolar residues which lie on the concave side of the right-handed helix to be buried with the formation of the left-handed supercoil. Residues at positions *e* and *g* are generally polar, helix favoring and preferentially charged in order to facilitate inter-helical salt bridges, providing added stability (Figure 1.1 B, C). This canonical *HPPHPPP* repeat constitute the majority of coiled-coils in nature. However, there are a few known right-handed supercoils, such as the tetrabrachion from *Staphylothermus marinus* that forms a parallel tetramer.[20] The peptides adopt a undecatad repeat, constituting 11 residues every three turns of the helix[18], with much larger cores than a typical left-handed tetramer.

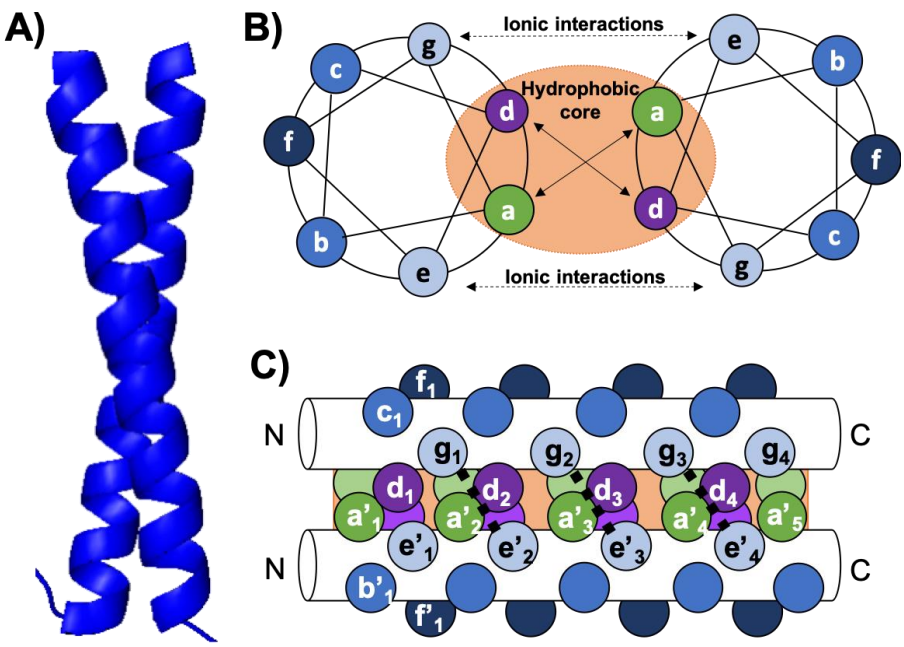

Figure 1.1 A) Cartoon representation of two coiled-coil forming a left-handed supercoil dimer, B) Helical wheel diagram (axial view) of the coiled-coil depicting hydrophobic (*a* & *d*) and ionic interactions (*e* & *g*) and, C) Lateral view depicting the burial of the *a* & *d* hydrophobic residues (shown in green and purple) with salt-bridges between *e* & *g* residues.

For the coiled-coils with a heptad configuration, the nature of the hydrophobic residues at *a* and *d* are typically aliphatic and not aromatic due to potential steric constraints posed by the latter.[21] The choice of residues typically determines partner selection, the degree of oligomerization and to some extent, the stability and helix orientation as well. This leads to another important characteristic of the coiled-coil helices - the 'knob-into-hole' (KIH) packing interaction. Side chains of the hydrophobic residues fit like a 'knob' into a pocket or 'hole' created by four side chains protruding from the partner helix (Figure 1.2 A).[22,23] For instance, in a coiled-coil dimer, the hydrophobic residue or knob at d_2 of one helix, packs into a hole created by the a'_2, d'_2, e'_2 and a'_3 residues of its partner helix. Likewise, a_3 of one helix, packs into a hole created by the d'_2, g'_2, a'_3 and d'_3 residues of its partner helix (Figure 1.2 B). The geometry of this packing interaction is

further illustrated in the context of the structure of the 31-residue leucine zipper region in the yeast transcription factor, GCN4.

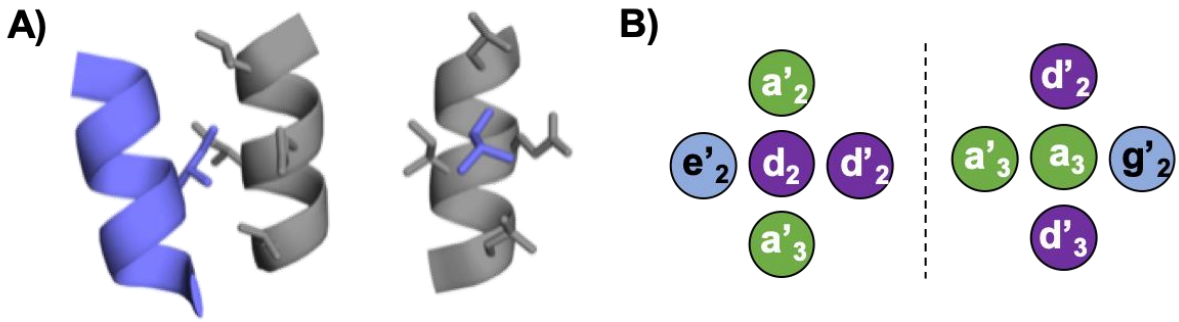

Figure 1.2 A) Side and head-on views of an isoleucine "knob" of the first helix packing between a diamond shaped "hole" formed by sidechains in the second helix[23] and, B) KIH interactions illustrated by the packing of d_2 and a_3 into their surrounding residues. (Modified from reference 23)

1.2.2 GCN4 Leucine Zipper: Accessing Different Oligomers

The GCN4 leucine zipper is a coiled-coil folding motif within a transcriptional activator protein. It is a parallel dimeric coiled-coil comprising 31 amino acids (~4 heptads), and is responsible for the dimerization of GCN4, leading to activation of more than 30 genes required for amino acid or purine biosynthesis. The dimeric coiled-coil structure of the GCN4 sequence had been experimentally determined and verified by Peter Kim in 1989.[24] Shortly after, Harbury *et al.*[25] systematically mutagenized the hydrophobic core of the dimeric leucine zipper to demonstrate how the peptide sequence affects the oligomeric state (number of alpha helices in the assembly). By substituting the four residues, Val-8, Asn-15, Val-22, Val-29 at the '*a'* position and four residues, Leu-4, Leu-11, Leu-18, Leu-25 at the '*d'* position to leucines, isoleucines or valines, different GCN4 variants were generated (Figure 1.3). In 1994, Peter Kim and his co-workers confirmed the nature of these interactions with the crystal structure of the isoleucine zipper trimer.[26] Sedimentation equilibrium analytical ultracentrifugation indicated that the peptide

variants could be mostly categorized into dimers (pIL), trimers (pII) or tetramers (pLI). The only notable difference between the three oligomers was the type of hydrophobic substitution at the '*a*' and '*d*' positions.

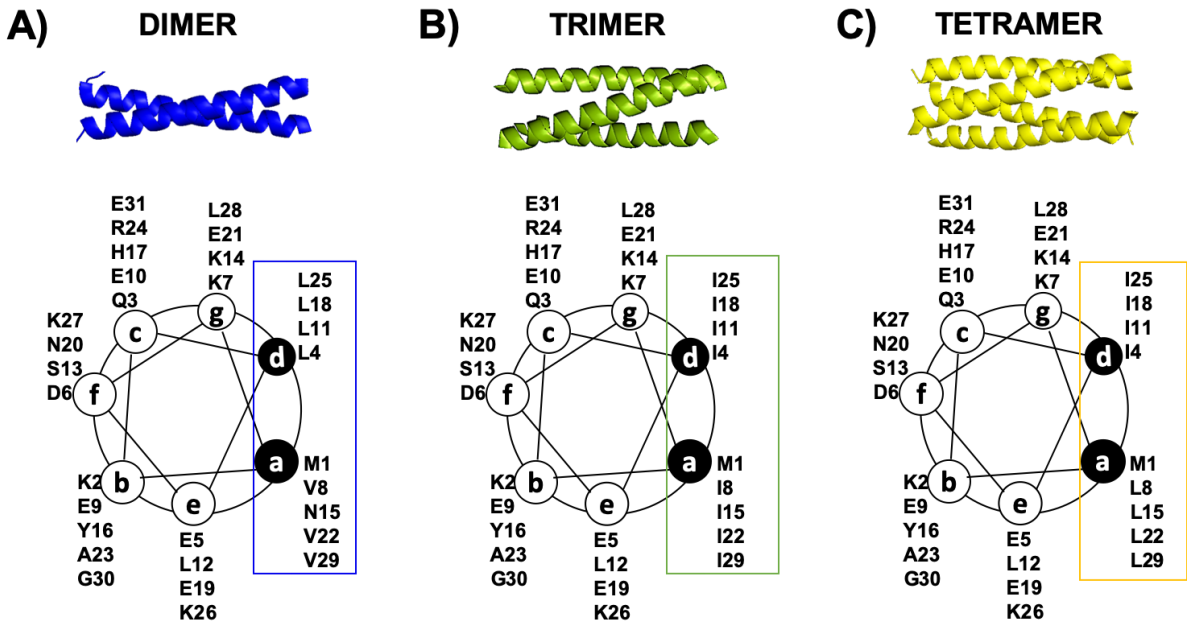

Figure 1.3 Helical wheel representation of the GCN4-p1 sequence illustrating the various oligomers A- Dimer (pVL), B – Trimer (pII) and C) Tetramer (pLI), formed with the substitution of different hydrophobic residues.

Therefore, the authors came to the conclusion that these packing interactions dictate the type of oligomerization. The dimer-pIL and tetramer-pLI differ by their hydrophobic residues at the *a* and *d* positions being interchanged, thus, resulting in an inversion of packing geometries, going from parallel-perpendicular to perpendicular-parallel, respectively (Figure 1.4 a, d, c & f). In contrast, the trimer-pII, which has isoleucine residues at both the *a* and *d* positions, has a geometric preference for packing at acute angles in both layers (Figure 1.4 b, e)[25]. In each layer, the Cα-Cβ bond of each isoleucine knob (red) forms an acute angle with the Cα-Cα vector (yellow) at the recipient, with a difference of 25^{o} between the two layers. Thus, the choice of residues at position

a and *d* dictate the aggregation of the resulting coiled-coil oligomer. The presence of beta-branched residues at *d* and *a* positions disfavors dimers and tetramers, respectively. However, the substitution of beta-branched hydrophobic groups at both *a* and *d* positions, like pII, favor the formation of a trimer.

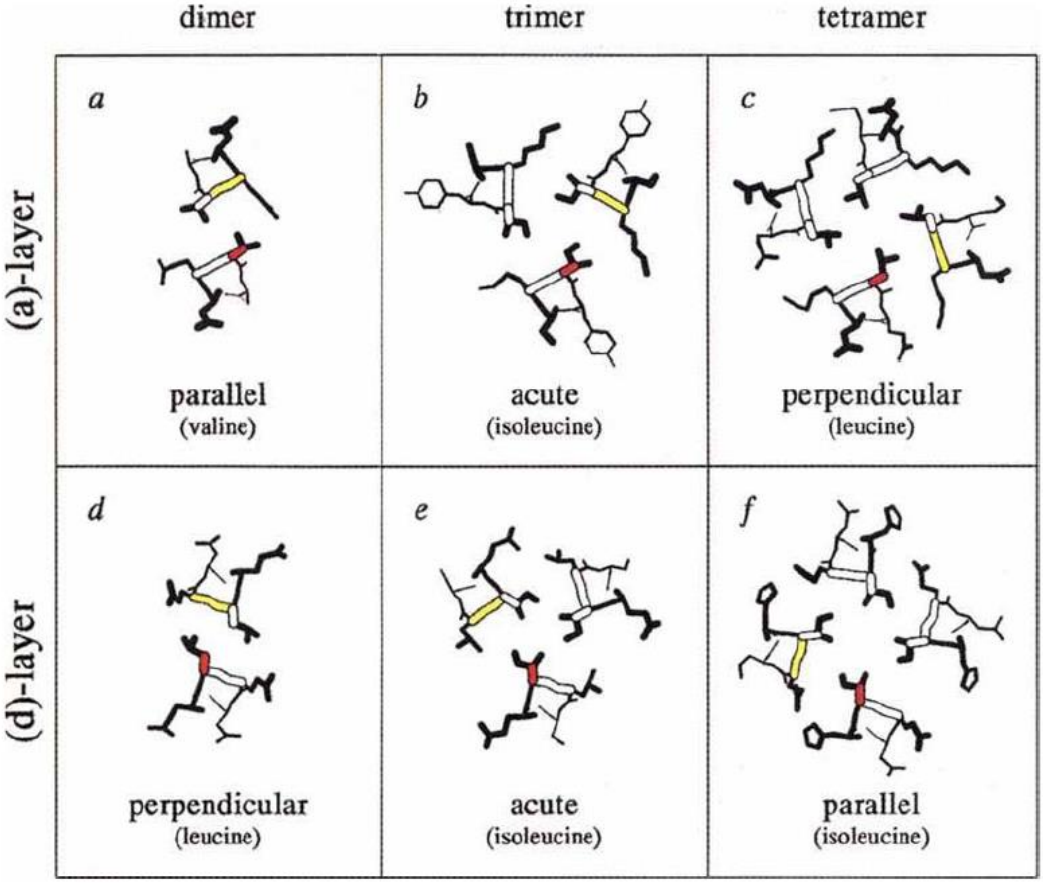

Figure 1.4 KIH packing geometries (looking down the axis from the *N* terminus) of the different GCN4 oligomers resulting from strategic hydrophobic group substitutions at the *a* and *d* positions (knobs = red, hole = yellow)[25]

1.2.3 Accessing Higher Oligomers: A Path to α-Helical Barrels

A consequence of increasing the oligomer state beyond four, is the added participation of the *e* and *g* residues within the hydrophobic core, which contribute to peripheral KIH interactions.[27] Therefore, all four residues at *a*, *b*, *e* and *g* positions act as knobs. This has been

demonstrated through the designed CC-Hex, a coiled-coil parallel hexamer, created by tactical mutations of the tetramer, CC-Tet (repeats of ELAAIKX). All the Lys residues at *e* were exchanged with Ala at *b*, which broadens the hydrophobic core to include a, d and e (Figure 1.5 a).[28] The packing geometry, that now accommodates a larger hydrophobic seam, deviates from the traditional KIH interactions and lies somewhere within the perpendicular and parallel packing distribution ranges observed for the tetramer (Figure 1.4). The resulting peptide which crystallizes into a parallel hexamer also leaves well-defined hydrophobic pore channels. Some of the side chains protruding into the pore have been mutated to aspartic acids and histidines,[29] demonstrating scope for chemically tunable coiled-coil channels.

There is also a heptameric coiled-coil, a GCN4-p1 mutant - CCHept, formed from substituting the *e* and *g* positions of the dimeric peptide with alanine residues (Figure 1.5 b).[30] The individual helices no longer pack in perfect alignment, instead the first and seventh helix are offset by a heptad (indicated by the arrows in Figure 1.5 b), which allows for inter-heptamer association (described later, Section 1.2.4.1 & Figure 1.10). The heptamer possesses an even larger channel, with a 9 Å diameter. The structures comprising six and higher oligomer states are more barrel-like, with their KIH packing interactions become less straightforward and their designs becoming harder to predict.

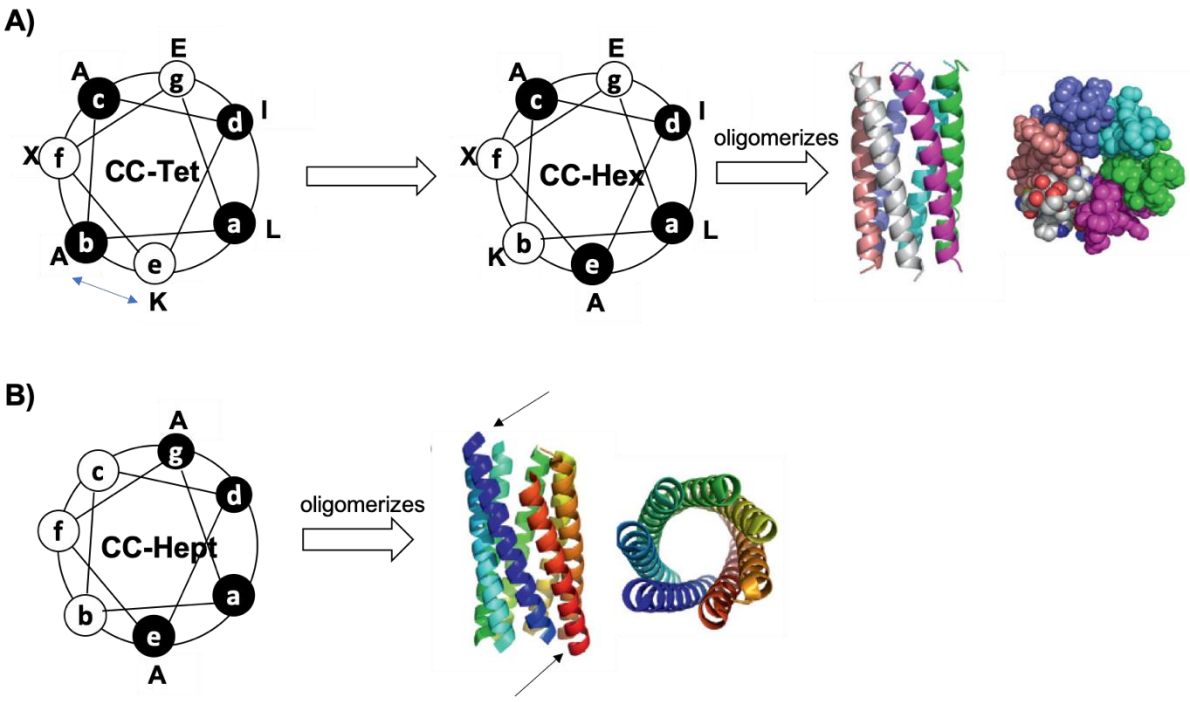

Figure 1.5 A) Helical wheel diagrams depicting the transformation of a coiled-coil tetramer into a hexamer bundle with a 6 Å pore channel, B) Helical wheel diagram of a heptameric mutant of the GCN4-p1 with a 9 Å pore channel. The arrows indicate the staggered alignment of helices within the bundle. (Modified from references 28 & 30)

1.2.4 Higher-Order Coiled-Coil Assemblies

The hierarchical assemblies of peptides result in structures that can be classified into either finite or infinite systems. This distinction usually reflects the physical nature of the resulting morphologies, which ultimately dictates the fate of their application. Infinite systems comprise fibrous structures that are typically one-dimensional, and 3D mesh networks that are capable of supporting cell growth and differentiation for tissue regeneration[31] and wound-healing applications. Finite systems, on the other hand refer to dimensionally compact structures such as spherical cages and crystals, used for applications in drug delivery and biosensing. Significant research has been directed toward developing self-assembling coiled-coil systems for the creation of synthetic scaffolds for biomaterial applications. Salient examples of the formation of such morphologies, as well as their potential applications, are discussed below.

1.2.4.1 Infinite 1D Assemblies

One dimensional assemblies, with high aspect ratios, possess a single dimension much higher than the others. They are some of the most widely reported peptide assemblies and exhibit a number of useful properties with potential for conductivity and biological interactions.

As one of the early pioneers of higher-order peptide assemblies, Woolfson *et al.* proposed the SAF (self-assembling fiber) system containing an off-set heterodimeric coiled-coil, comprising two short peptides SAF-p1 and SAF-p2 (Figure 1.6 a).[32,33] Each of these peptides, contain four heptads in a +, +, -, - pattern, such that the first two heptads are positively charged and the last two heptads are negatively charged (Figure 1.6 a). The peptides co-assemble to form a sticky-ended dimer (A-B interacts with charge complementary C-D, Figure 1.6 b), promoted by hydrophobic and electrostatic contacts. These dimers promote fibrillogenesis in a longitudinal fashion, forming the 1st generation fibers (Gen 1 = 43 ± 9 nm width; Figure 1.7 a - i) that are tens of micrometers long. Strategic mutations on the SAF-p2 (A4R, A7Q, H11R and Q21Y) were introduced to create a second generation SAF system, SAF-p2a (Figure 1.6 a).[32, 34] The co-assembly of SAF-p1 and SAF-p2a resulted in thicker and more stable 2nd generation fibrillar assemblies (Gen 2 = 69 ± 18 nm width) as result of increased lateral interactions. In order to introduce discontinuity in what appeared to be a linear structure, the assembly mixtures were doped with fiber-shaping (FiSH) peptides, CC^{NN} and DD^{CC}. The FiSH peptides are duplicated C and D units of the SAF-p2a sequence joined through their *C* and *N* termini, respectively. This sets up the possibility of single units of CC^{NN} and DD^{CC}, each interacting with two SAF-p1 peptides (Figure 1.6 c). The addition of CC^{NN} induced kinks within the SAF-p1 and SAF-p2a mixtures. Varying the concentration of CC^{NN} altered the number of kinks present and the overall length of the fibers (Figure 1.7 b – i, ii & iii). In contrast, the doping of DD^{CC} induced the formation of splits/branches, respectively within

the fibers (Figure 1.7 c). Interestingly, with the addition of CC^{NN} to the original SAF-p1 and SAF-p2 system, a greater number of kinks were apparent (Figure 1.7 a - ii). This suggests that the thinner, more flexible Gen 1 fibers are more accommodating of structural irregularities.

In order to further increase the overlap of the alpha-helices, a 3rd generation SAF system – SAF-p1-ext and SAF-p2a-ext (Gen 3, Figure 1.6 a), were designed with the incorporation of an additional heptad within each sequence. The Gen 3 fibers (Figure 1.7 d – i & ii), though highly ordered, were thinner (58 ± 10 nm width)[34] than the Gen 2 fibers. However, after three generations of peptide design, there was a marked improvement in the stability and thickness of the fibers: critical peptide concentration for assembly decreased from 60 μM to 4 μM and T_m increased from 22 °C to 65 °C.[34] The SAF system was also modified to produce thinner, more flexible fibers by introducing electrostatic networks of arginine and glutamic acid residues to the surfaces.[35]

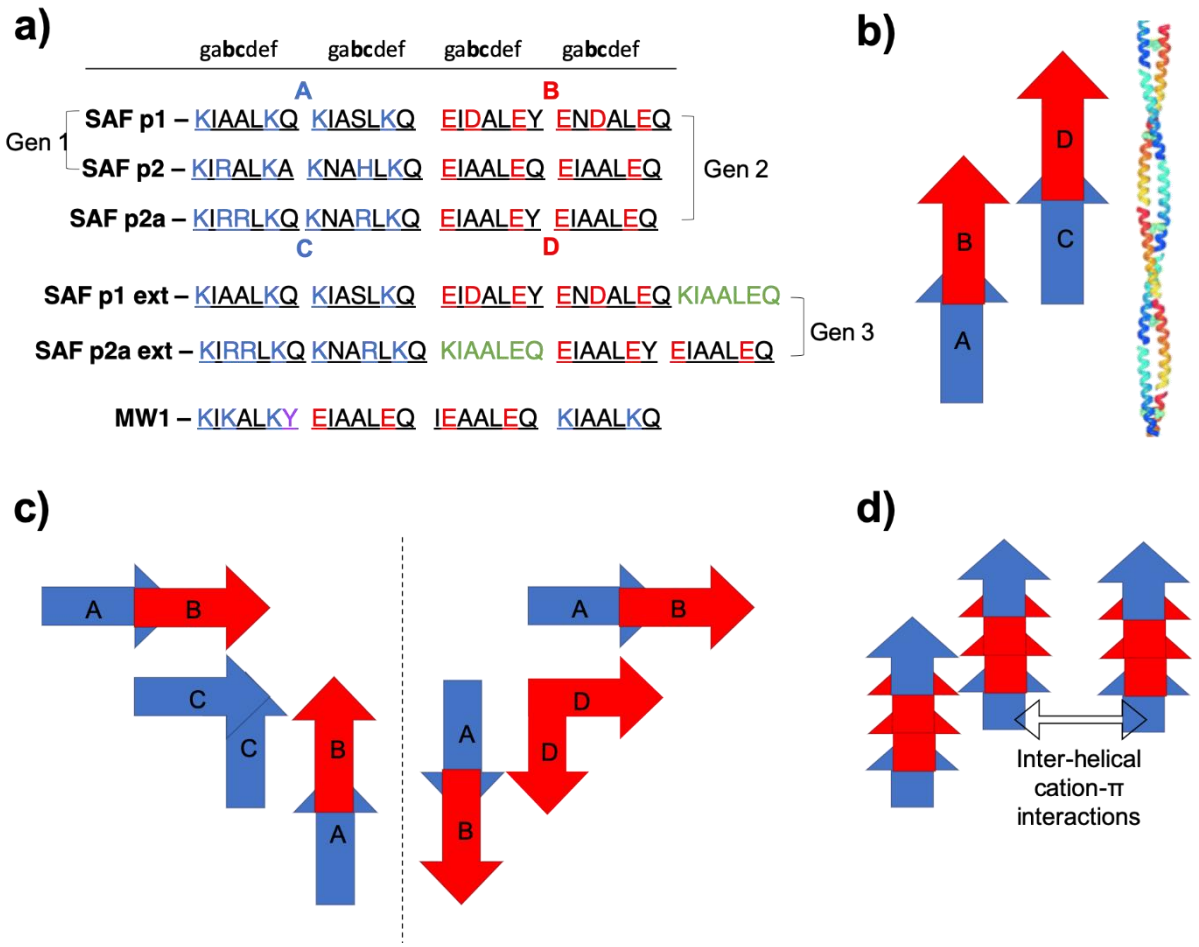

Figure 1.6 **a)** Peptide sequences of SAF-based and MagicWand (MW) coiled-coils, **b)** Illustration of the co-assembled SAF peptides forming sticky-ended dimers, **c)** Illustration of kinked fiber assembly induced by the addition of CC^{NN} and DD^{CC} peptide units and, **d)** Illustration of MW1 assembly. The direction of the arrows within the peptide subunits indicate *N* to *C* direction. (modified from references 32-34 & 36).

In contrast to the co-assembled peptide systems outlined above, a single peptide sequence (MagicWand, MW1) with cationic terminal quarters and anionic central halves (+, -, -, + pattern) was demonstrated to form highly ordered nano-to-mesoscale fibers.[36] The palindromic design relies on hydrophobic residue pairing within the coiled-coil core and charged residues flanking the core to form the off-set dimer (Figure 1.6 a and d). In addition, inter- and intra-helical cation-π interactions between the K3 and Y7 residues, contribute to both fiber thickening and stability. The fibers were also reported to be far more stable than the third generation SAF design, with a T_m of

73 ºC (Figure 1.7 e-i). The resulting fibers were microns long and tens of nanometers thick (Figure 1.7 e-ii), without any branching, capturing many of features from the SAF design but with a more straightforward single peptide design. Various generations of the SAF peptides have been decorated with fluorescent labels and streptavidin-gold nanoparticles through the conjugation of biotin, thus, paving the way for functional multi-component systems.[37, 38]

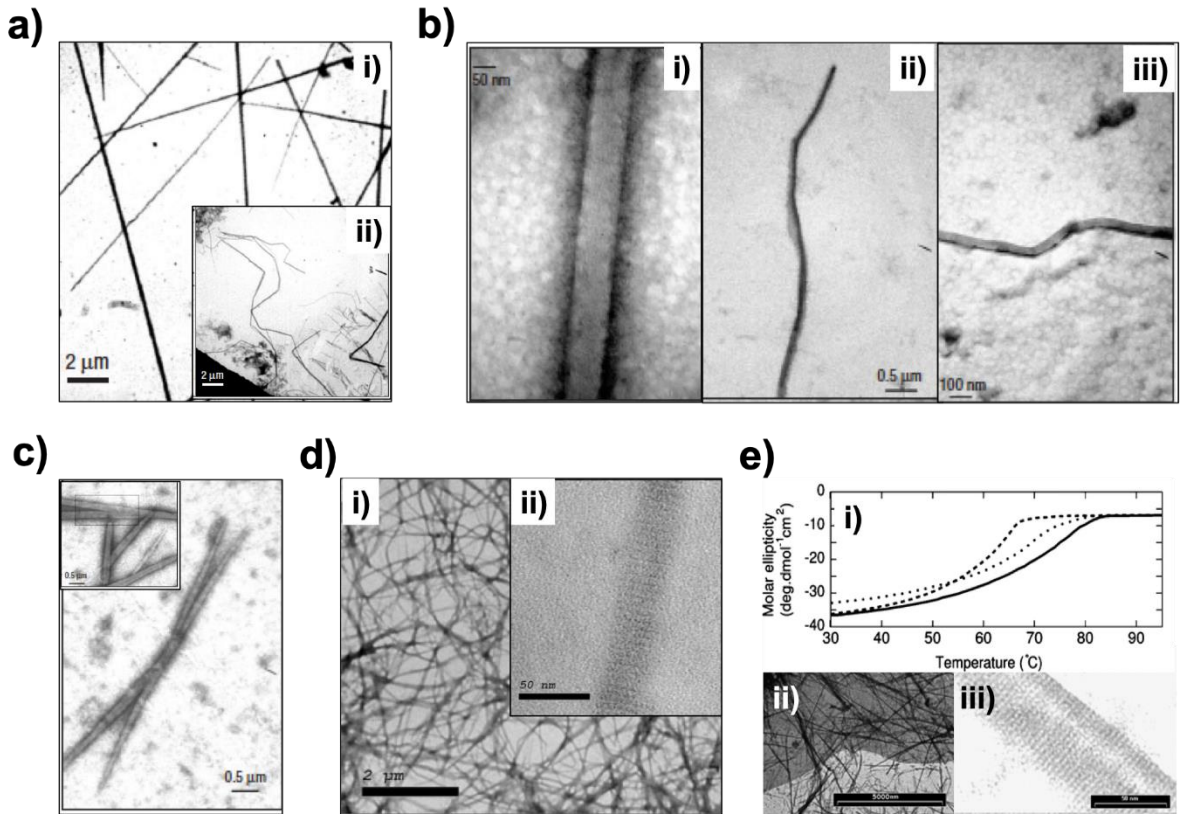

Figure 1.7 TEM images of fibers formed from **a)** (i) 1:1 SAF-p1:SAF-p2, (ii) I doped with CC^{NN} FiSH peptide, **b)** (i) 1:1:1, (ii) ≥ 0.1:1:1 & (iii) < 0.1:1:1 ratios of CC^{NN}:SAF-p1:SAF-p2a, **c)** ≥ 0.01:1:1 DD^{CC}:SAF-p1:SAF-p2a mixtures, **d)** extended SAFs depicting banding pattern within the fiber (inset) and, **e)** (I) CD melting curve of MW1 peptide, (II) TEM of fibers (III) with their corresponding banding pattern (Modified from references 32-34 & 36).

Conticello and co-workers proposed a coiled-coil trimer, based on the GCN4-pII design, which utilizes its charged residues to promote inter-helical complementary electrostatic interactions when arranged in a staggered alignment to form sticky ends (Figure 1.8).[39]

Substitution of isoleucine residues with histidine on alternate heptads (TZ1H) led to a pH-dependent association of the helices, leading to the formation of long aspect ratio fiber bundles with widths of 40-100 nm. These bundles consisted of thinner fibril assemblies spanning 3.3 ± 0.7 nm (Figure 1.8 C). Both the assembly of the fibers as well as the coiled-coil motif were demonstrated to be pH reversible. The same peptide sequence was also subjected to metal-assisted assembly, with Ag^{+}, to produce fibers with high aspect ratios of similar morphology.[40] It is worth noting that again, the metal played a role in the formation of the coiled-coil itself and the inter-coil electrostatic interactions mediated the assembly growth. Further modification of the sequence with cysteine residues in the *a* positions of the 2^{nd} and 5^{th} heptads to form TZ1C2, that can adopt two distinct orientations of its helices. As a sequence variant of TZ1H, the staggered (out-of-register) helices can form similar high aspect ratio fibrils. But with the substitution of cysteine residues and subsequent ligand coordination with Cd(II), the trimer demonstrates a registry shift leading to an alignment of the helices within the coiled-coil trimer. The addition of Cd^{2+} thus, disrupts the assembly (Figure 1.8 E).[41] This interaction was found to be reversible as the subsequent addition of EDTA chelated the Cd^{2+} and reformed the fibers.

A)

		abcdefg	abcdefg	abcdefg	abcdefg	abcdefg	abcde
TZ1H	AcNH-E	IAQHEKE	IQAIEKK	IAQHEYK	IQAIEEK	IAQHKEK	IQAIK $CONH_2$
TZ1C2	AcNH-E	IAQIEEE	CQAIEER	IAQIEYR	IQAIEEK	CAQIKEK	IQAIK $CONH_2$

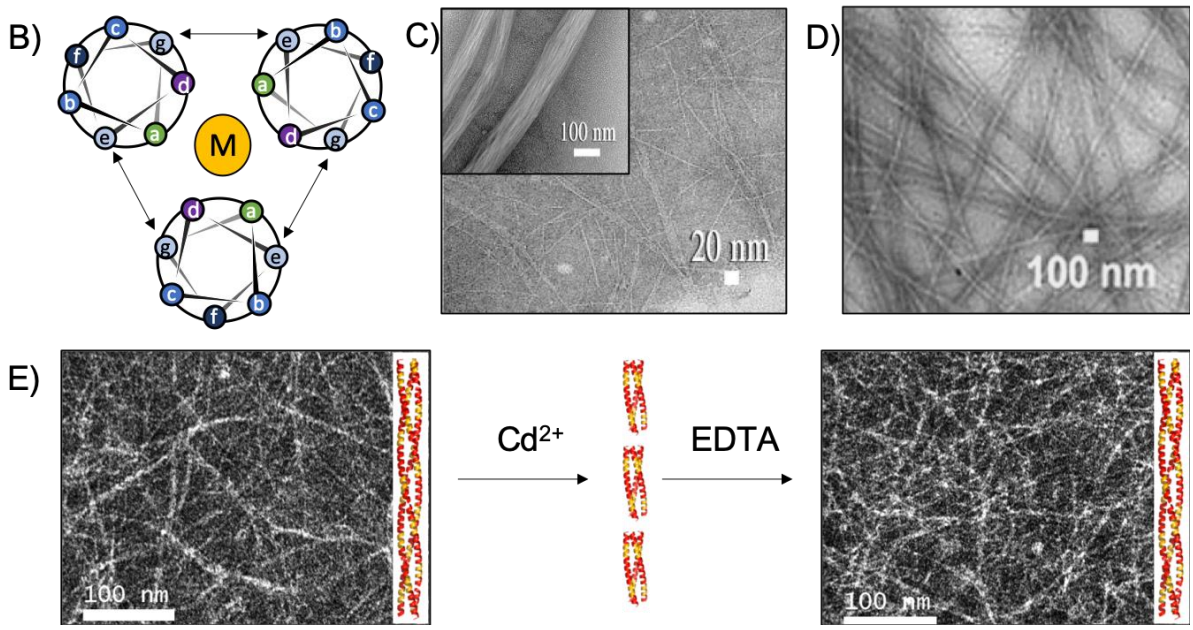

Figure 1.8 A) Peptide sequences of trimeric coiled-coils TZ1H and TZ1C2; B) Representative helical wheel diagram of trimeric coiled-coil; TEM images of fibers assembled from TZ1H C) in the absence of silver and D) in the presence of silver; E) TZ1C2 assembled fibers dissolved as a result of a Cd^{2+} induced register shift, followed by subsequent reformation with the addition of EDTA. (Modified from references 39-41)

Some other prominent examples include reports by Montclare *et al.* who demonstrated the formation of helical fibers via differential binding of divalent metals to the coiled-coils, His_6-C and His_6-T40A, with N-terminal hexahistidines (C represents the coiled-coil domain of the cartilage oligomeric matrix protein). Here, metal binding is used to control the conformation of the assemblies.[42] Both His_6-C and His_6-T40A form fibers, 10-15 nm in diameter, in the absence of metal (Figure 1.9 A-B). However, with the addition of Zn(II), though the fiber dimensions remained consistent, His_6-T40A demonstrated a higher density of fiber growth (Figure 1.9 D).

In order to generate thicker, more stable fibers, the effects of substituting fluorinated amino acid residues within similar coiled-coil sequences was investigated. The fluorinated derivatives of

peptides Q and C, via the incorporation of 5,5,5,-trifluoroleucine (TFL), produced thicker, more stable fibers than their non-fluorinated counterparts (Figure 1.9 E-H).[43] The enhanced stability of the fluorinated fibers in the presence of Zn(II), allows for binding to small molecules like curcumin. Also, the engineered homopentameric coil (Q) has been demonstrated to form mesoscale fibers (up to 560 nm in width) in the presence of hydrophobic molecules (Figure 1.9 I-J).[44] The ability of these fibers to bind small molecules like curcumin under physiological conditions, in conjunction with their response to external soluble metal ions, demonstrate their potential for the development of novel biomaterials.

	His-tag	abcdefg	abcdefg	abcdefg	abcdefg	abcdefg	abcdefg	
His_6-C	MRGS**HHHHHH**GSGDL	APQMLRE	LQE***T***NAA	***L***QDVREL	LRQQVKE	ITFLKNT	VMESDAS	GKLN
His_6-T40A	MRGS**HHHHHH**GSGDL	APQMLRE	LQE***A***NAA	***L***QDVREL	LRQQVKE	ITFLKNT	VMESDAS	GKLN
Q	MRGS**HHHHHH**GS I EGR	VKE	ITF***L***KNT	APQM***L***RE	***L***QETNAA	***L***QDVRE***L***	***L***RQQSK***L***	
Q+TFL	MRGS**HHHHHH**GS I EGR	VKE	ITFT_{FL}KNT	APQMT_{FL}RE	T_{FL}QETNAA	T_{FL}QDVRET_{FL}	T_{FL}RQQSKT_{FL}	
C	MRGS**HHHHHH**GS I EGR	APQM***L***RE	***L***QE***T***NAA	***L***QDVRE***L***	***L***RQQVKE	ITF***L***KNT	SK***L***	
C	MRGS**HHHHHH**GS I EGR	APQMT_{FL}RE	T_{FL}QE***T***NAA	T_{FL}QDVRET_{FL}	T_{FL}RQQVKE	ITFT_{FL}KNT	SKT_{FL}	

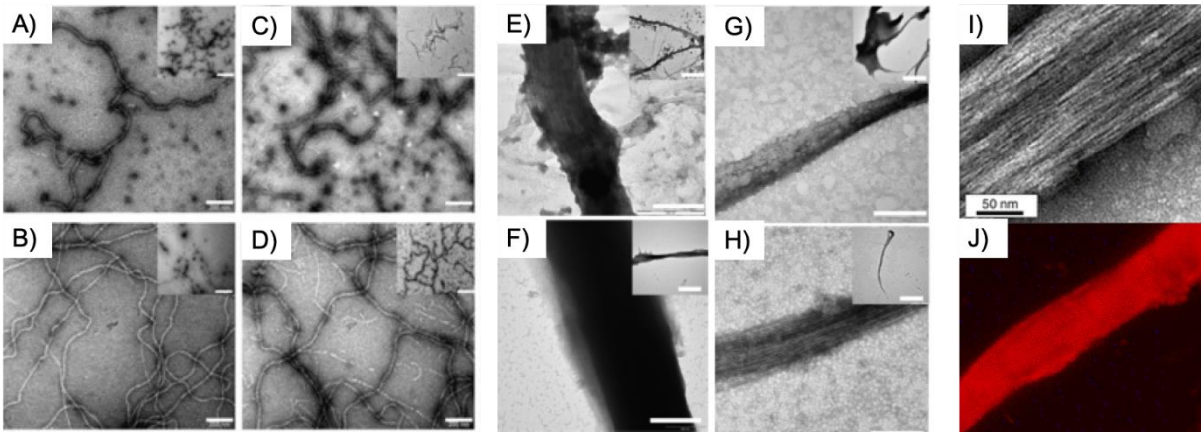

Figure 1.9 Table with coiled-coil peptide sequences; Fibers formed at pH 8.0 from A) His_6-C, B) His_6-T40A, C) His_6-C in the presence of Zn(II), D) His_6-T40A in the presence of Zn(II); Fibers formed from E) C in the presence of Zn(II), F) Q in the presence of Zn(II), G) C+TFL in the presence of Zn(II), H) Q+TFL in the presence of Zn(II); Fibers formed at pH 4.0 from I) Q and, J) 3D reconstruction of confocal data depicting the Q-fiber assembly in the presence of curcumin (Modified from references 42-44)

Coiled-coil dimers proposed by Ogawa *et al.*, were assembled via coordination of a square planar Pt(II) complex to form one-dimensional fibers with lengths on the order of several hundred nanometers, but with widths ranging from 4 to 10 nm.[45] There is also an interesting report of leucine zipper peptides that fuse into a dendrimer core, which further self-organize into fibers.[46]

Fiber-like tubes assembled from coiled-coil building blocks have also been reported. Extended filamentous nanotubes were formed from a 29 residue peptide, containing two off-set hydrophobic faces (a/d, c/f) by Conticello *et al.*[47] The bifaceted hydrophobic faces was proposed to drive coiled-coil assembly into cylindrical filaments with the alpha-helices lined parallel to the fiber axis. More notably, a substitution pattern of placing smaller hydrophobic groups (alanines) on the outer interface (a/f) and larger groups (leucines and isoleucines) on the inner interface (c/d) would decrease the curvature between interacting helices, affording larger diameter tubes. The Form I peptide formed long cylindrical tubes of 60 Å width. However, by mutating the arginines in their Form 1 sequence to lysines (Form II), they demonstrated a transformation from a single-walled to a double-walled nanotube with a 120 Å width (Figure 1.10 B-C). The arginine and lysine residues occupy the b and e position on the helical wheel, which participate in inter-bundle local interactions. These interactions are further propagated to the global structure as a result of helical repetition within the assemblies, accounting for the difference in resulting morphology. The Form I peptide has been conjugated at the *N* terminus to various epitopes, creating a vaccine delivery platform that would be useful in the design of biomaterial-based immunotherapies.[48]

Conticello and his co-workers also designed a 7-helix bundle structure, derived from the GCN4-pAA sequence, that resembles supramolecular lock washers.[49] The heptameric coiled-coil consists of a hydrophobic face that spans positions *g*, *d*, *a* and *e* of the heptad (Figure 1.10 D) with a continuous central channel of 7 Å dia. In addition, there is a single-residue registry shift between

adjacent helices with uncapped, complementary interaction sites at the *N* and *C* termini. These lock washers self-associate into long tubes with high aspect ratios and sub-nanometer pore sizes (Figure 1.10 E-F).[50]

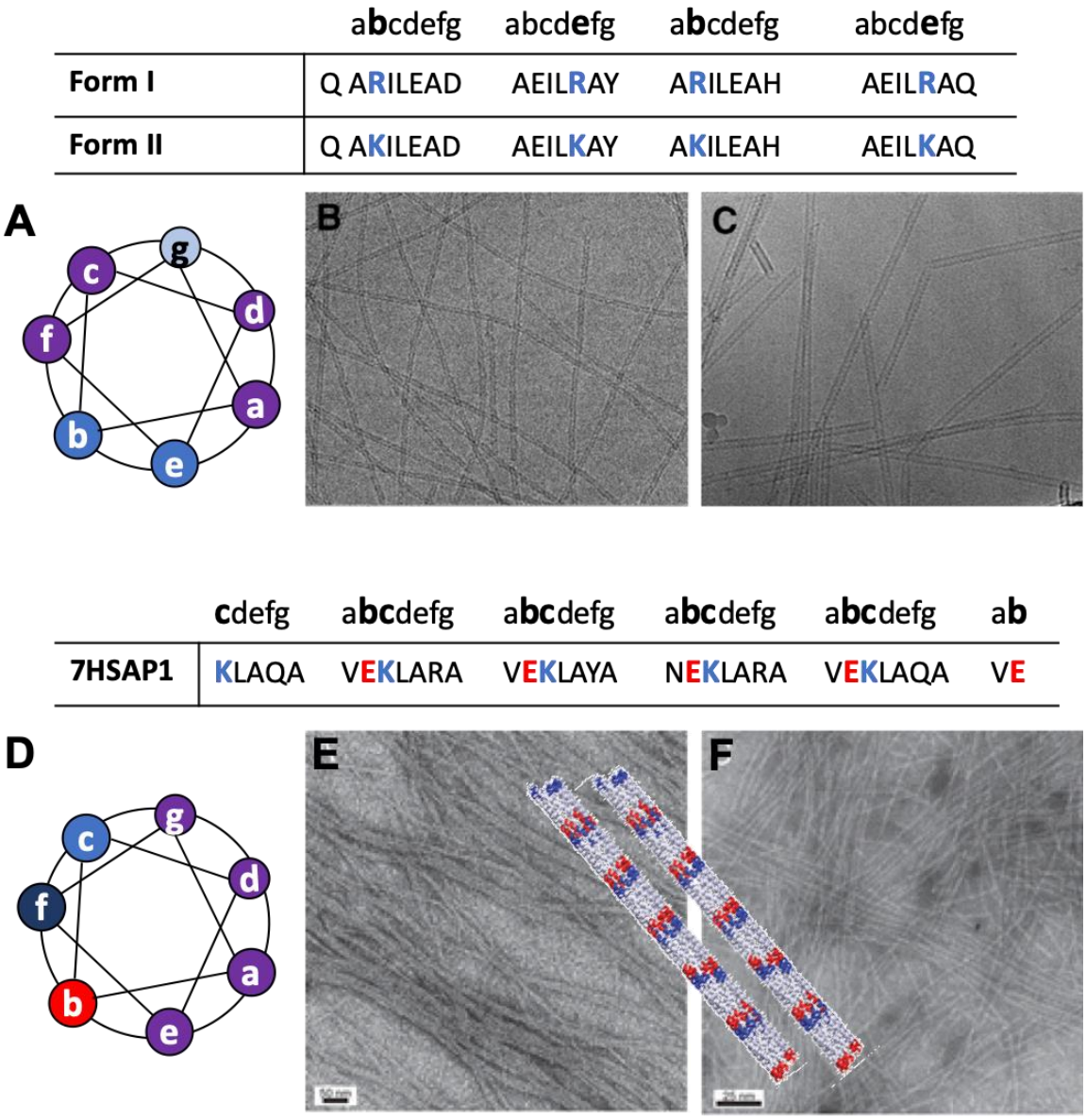

Figure 1.10 Top – Peptide sequences and A) helical wheel diagram of the Form I and II peptides; B) single-walled nanotubes formed from Form I and C) doube-walled nanotubes formed from Form II; Bottom – Peptide sequences and D) helical wheel diagram of 7HSAP1; E) TEM and F) STEM images of 7HSAP1 at pH 6.0. Placement of hydrophobic residues on the helical wheels are indicated in purple. (Modified from references 47-49)

Woolfson and co-workers also demonstrated the assembly of multichannel tubes from hexameric coiled-coils barrels.[51-52] The CC-Hex-T (Figure 1.11) barrels associate both longitudinally and laterally to form thickened peptide nanotubes (PNTs) at pH 7.0, with 6 Å pore channels. Annealing of these fibers, by heating from 5 to 95 ^{o}C over 180 min and subsequent cooling to 25 ^{o}C for 20 min, produced highly ordered structures, 70 nm in diameter.[52] These tubes were observed to be pH sensitive, as protonation of the glutamic residues at low pH caused a disruption in the lateral assembly. As a result, thinner fibers of 3-4 nm in width were obtained (Figure 1.11 B). Since increasing the number of positive charges on the outer surface of these bundles led to thinner fibrils, mutation of the Q6 and Q27 residues to lysines (CC-Hex-T+) produced the similar sized fibers at neutral conditions (Figure 1.11 C).[51] To ensure further stability, the barrels were covalently linked to one another via native chemical ligation.[51] In this way, a third peptide, CC-Hex-T+co was synthesized to include an *N*-terminal cysteine and a *C*-terminal thioester. Thus, different assembly modes were probed via strategic peptide design modifications. Such tubular structures with nanopore channels have the potential to accommodate size-appropriate cargo.

		abcdefg	abcdefg	abcdefg	abcdefg	
CC Hex-T	H	LKAIAQE	LKAIAKE	LKAIAWE	LKAIAQE	-OH
CC-Hex-T +	H	LKAIAKE	LKAIAKE	LKAIAWE	LKAIAKE	-OH
CC-Hex-T +co	H	CKAIAKE	LKAIAKE	LKAIAWE	LKAIAKQ	-SBzl

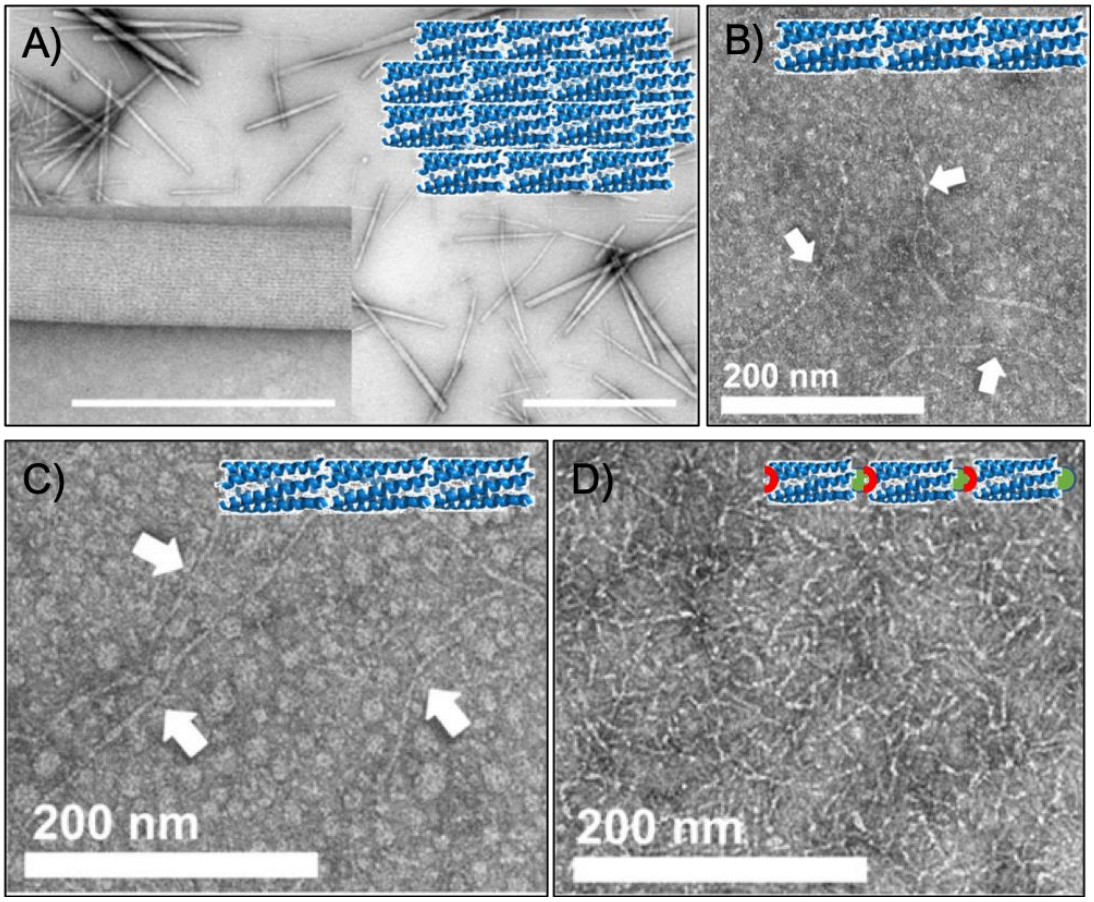

Figure 1.11 CC-Hex peptide sequences and the nanotube structures formed from A) annealed CC-Hex-T at pH 7.0 B) CC-Hex-T at pH 5.0 C) CC-Hex-T+ and, D) CC-Hex-T+ co. The white arrows point out the single PNTs. (Modified from references 51 & 52)

More recently, Pochan *et al.* described the pH dependent assembly of a de novo designed homotetrameric coiled-coil, AC (Figure 1.12 A) that forms nanotubes with inner diameters of 13 nm at pH 4.5 (Figure 1.12 B).[53] TEM and X-ray analysis revealed tubes with consistent pore diameters in the order of 13 nm with tube wall thickness of ~ 3 nm, made from a single layer of peptide bundles in a tilted arrangement (Figure 1.12 C). The tilt is caused by inter-bundle repulsion

of the residues at each N-terminus i.e., charge of the amino groups at the N-terminus and Arg 3 located at the end of the bundle. Modification of the arginine residue to a lysine (R3K, Figure 1.12 A), also resulted in the formation of tubes but with smaller tube diameters (11.7 nm) and a thicker wall of 4 nm. The replacement with lysine, which has a lower pKa and smaller side chain, results in a reduction in tilt angle (Figure 1.12 C). The reduced tilt angle accommodates a tighter packing of bundles and therefore, a smaller tube width.

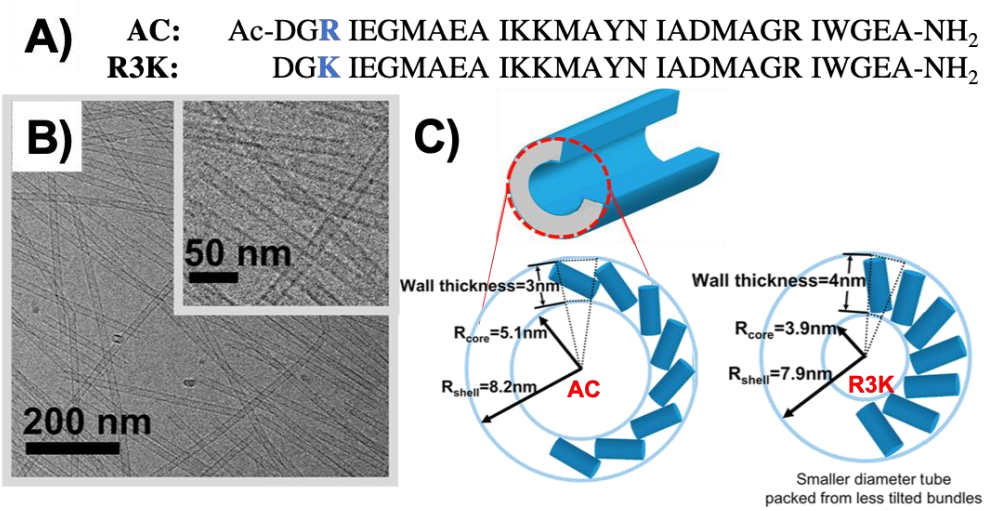

Figure 1.12 Coiled-coil tetramer-based tubes, platelets and needles formed from pH variation. (Modified from reference 53)

1.2.4.2 Infinite 3D Assemblies

Hydrogels, formed from cross-linked polymers into a three-dimensional water-swollen network, have a wealth of potential applications as substitutes for the extracellular matrix, wound treatment and drug-delivery. Often these 3D networks are formed from 1D structures that entangle. The most common hydrogels derived from coiled-coils follow an ABA triblock architecture, first developed by Petka *et al.*[54] The design was further developed by Xu and Kopeček.[55] The triblock comprises coiled-coil endblock domains (CC_A & CC_B) and a hydrophilic random coil domain (RC)

(Figure 1.13). Self-association of the CC-domains, driven by their hydrophobic collapse, initiates cross-linking of the triblock segments into a water-swollen network. The gel to sol transition of these hydrogels was demonstrated to be reversible, and their physical characteristics were highly tunable with minute sequence alterations. David Tirrel's lab introduced the ABC copeptide system, wherein the coiled-coil domains are less likely to associate heteromerically, thereby inhibiting the formation of intramolecular loops otherwise prevalent in the ABA system.[56] In addition, hybrid systems containing coiled-coil peptides and synthetic polymers have also been employed to create hydrogels that demonstrate dynamic physical responses in response to temperature[57] and light.[58]

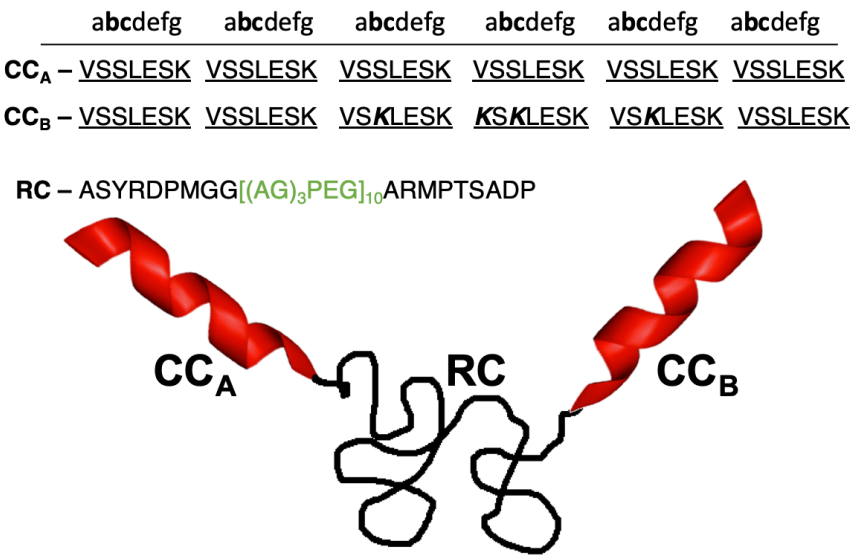

Figure 1.13 Graphical representation of the ABA triblock copeptide system (Modified from references 54-56)

Thus far, the coiled-coil was used primarily as a recognition motif to initiate the cross-linking. The flexibility of the swelling was provided by the hydrophilic group. Woolfson and coworkers have also employed their SAF system to create hydrogels solely from the coiled-coil dimers. The Gen 1 SAF peptide (Figure 1.6 a) was modified to incorporate either alanine and glutamic acids at

b, ***c*** and *f* positions to form hSAF peptides. The hSAF peptides form hydrogels driven by weak hydrophobic and hydrogen-bonding interactions along their polar interface.[60] $hSAF_{QQQ}$ and $hSAF_{AAA}$, containing glutamine and alanine residues, respectively form interconnected fibers when assembled on ice (Figure 1.14 A-B). Upon warming to room temperature, the $hSAF_{AAA}$ forms a more homogeneous network (Figure 1.14 D). The control sequence $hSAF_{AAQ}$ did not yield any fibrous structures (Figure 1.14 C). As the coiled-coil motif retains its structural integrity even with sequence mutations and chemical modifications, RGDS has been successfully incorporated within the aforementioned hydrogels, with demonstrated potential for tissue engineering applications.[61,62]

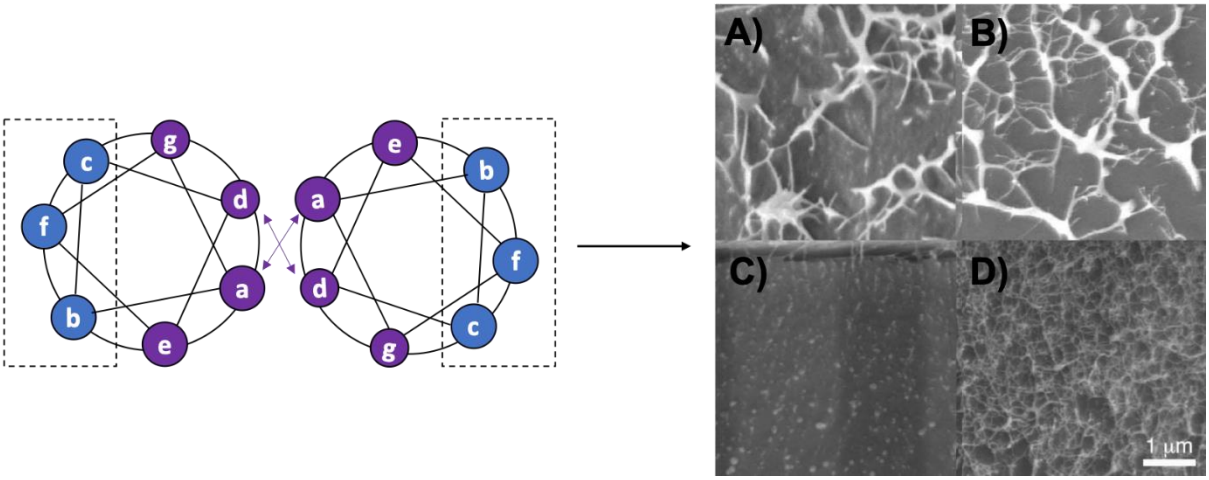

Figure 1.14 hSAF peptides with modified *b*, *c* & *f* residues with limited interactions on the polar face resulting in thinner, flexible gel-like fibers. Network gel fibers prepared from A) $hSAF_{QQQ}$, B) $hSAF_{AAA}$, and C) $hSAF_{AAQ}$, assembled on ice in 15 min. D) $hSAF_{AAA}$ fibers prepared on ice and cooled to room temperature. (Modified from reference 60)

1.2.4.3 Finite 2D & 3D Assemblies

There have also been some reports of more unique higher-order assemblies, the sizes of which are confined in at least two out of the three dimensions. Interestingly, the coiled-coil tetramer, AC (Figure 1.12) that was earlier described to form 1D nanotubes at pH 4.5, forms 2D

platelet-like assemblies at pH 7.0.[53] At neutral conditions, the repulsive interactions, which were dominant at acidic conditions, are weakened. Inter-bundle salt-bridges between lysine and aspartic acid residues aid in the formation of coiled-coil sheets that stack into platelets. At pH 10, the salt-bridge is weakened as a result of partial deprotonation, destabilizing the bundle-bundle interface. This transforms the assembly into needle-like structures (Figure 1.15).

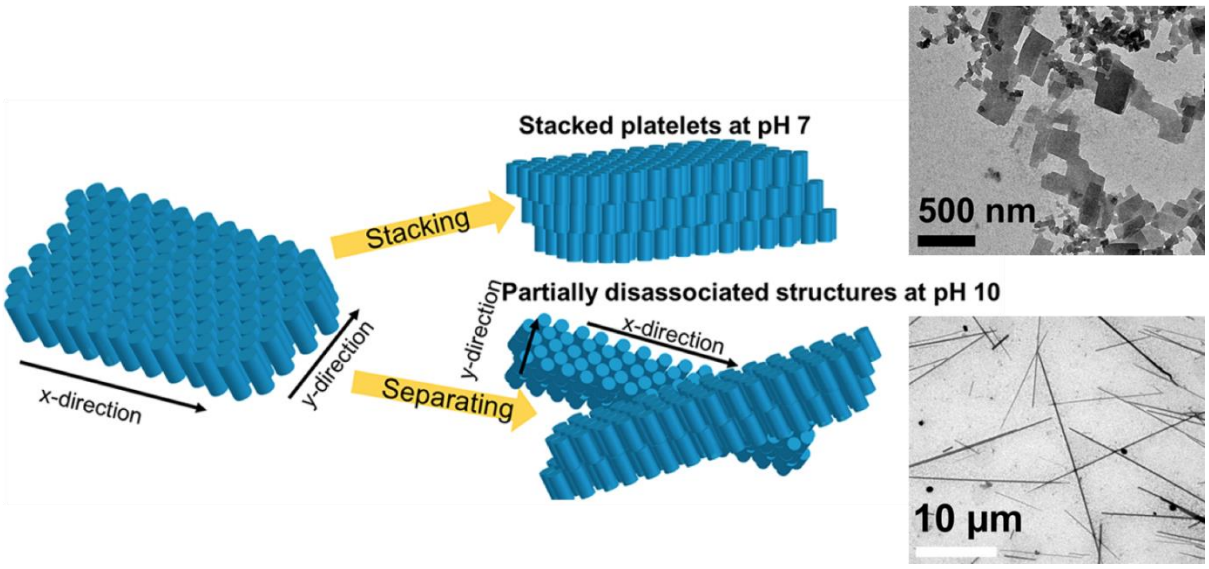

Figure 1.15 Illustration of pH-dependent assembly of a coiled-coil tetramer into platelets (pH 7.0) and needle-like structures (pH 10). (Modified from reference 53)

Woolfson *et al.* proposed a design that incorporates the disulfide cross-linking of heterodimeric (CCTri) and homotrimeric (CCDiA-B) bundles (Figure 1.15 a). Cysteine residues in the central heptads were used to link CC-Tri and CCDiA or CCDiB via disulfide bonds. This resulted in the formation of two distinct complementary hubs, CCTri-CCDiA and CCTri-CCDiB, which, driven by the association of A and B helices to form a dimer, tesselate together to form a hexagonal network (Figure 1.15 b). The hexagonal patterned net, with pores of 5-6 nm, still contain unsatisfied coiled-coils along its edges, which drive the hubs to close and form cages, ~ 95 nm in size (Figure 1.15 c - top).[63] The rigidity of the hub and localized curvature contribute to a tight size

distribution of the particles. To probe the flexibility of the hub, the asparagine residues of the heterodimer were mutated to isoleucine residues to ensure higher affinity for dimerization without altering the resulting hub geometry. The modified nanocages had diameters of ~ 68 nm (Figure 1.15 c - bottom). This illustrates a modular approach towards creating routes for closed systems with potential for encapsulation and subsequent drug-delivery applications.

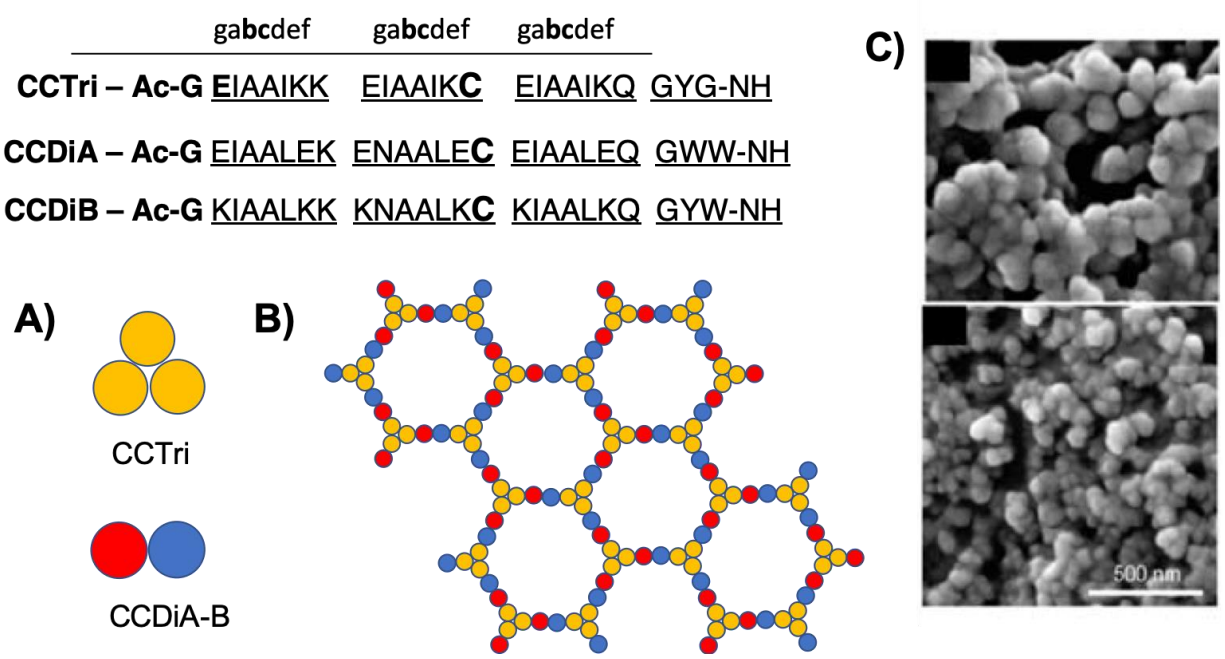

Figure 1.16 Self-assembly of A) coiled-coil homotrimers and heterodimers that tesselate to form B) a hexagonal network with pores of 5-6 nm and, C) collapse into spherical cages. (Modified from reference 63)

There are other reports that include the use of cross-linkable coiled-coils to form micron sized clusters that evolve into fractal structures[64] and non-covalent dendrimer-type architectures towards the design of a polynanoreactor used to synthesize silver nanoparticles.[65] In addition, the assembly of a polypeptide tetrahedron, assembled from coiled-coil forming fragments has also been described.[66]

More recently, the Chmielewski group used the GCN4-based coiled-coil trimer (Figure 1.3 B) with strategic ligand modifications (NTA and His_2) at the termini to enable metal-mediated assembly of hexagonal microcrystals (Figure 1.17).[67] The crystal morphology was controlled by variation in the peptide:metal ratio, resulting in hexagonal discs to longer hexagonal crystals. X-ray diffraction studies revealed a hexagonal honey-comb packing lattice with adjacent coiled-coils arranged in antiparallel orientations. The crystals also provided the means to direct His-tagged guest molecules at specific sites within the crystal boundaries, thereby enhancing their potential applications as drug-delivery agents, probes and sensors. A variation of this design incorporated the decoration of aromatic moieties along the backbone to produce banded micro- and nano-structures (discussed in Chapter 2).[68]

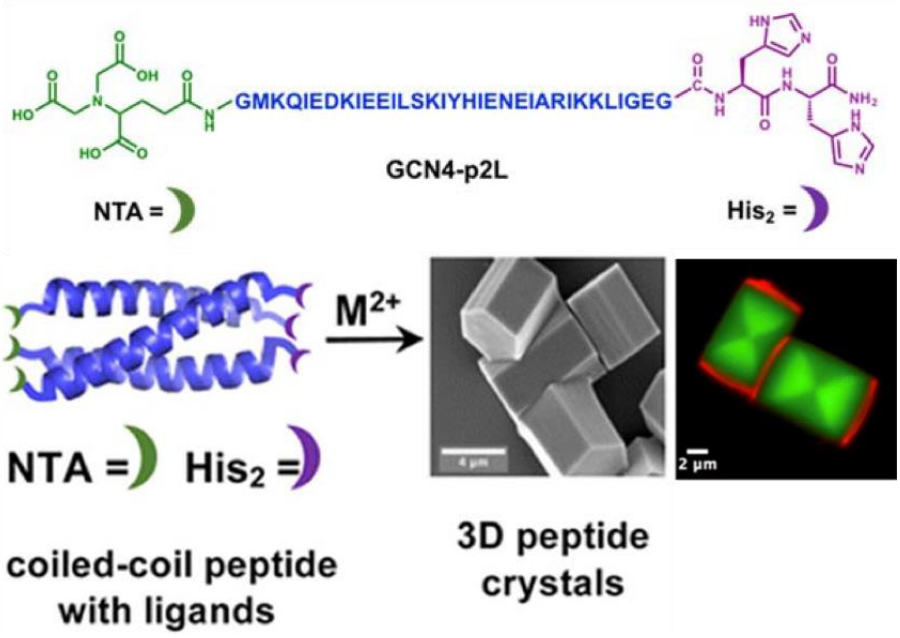

Figure 1.17 Metal promoted head-to-tail assembly of a coiled-coil trimer (GCN4-p2L) into hexagonal crystals displaying site-specific inclusion of His-tagged fluorophores. (Modified from reference 67).

1.3 Conclusions

The alpha-helical peptide motif can be chemically programmed to differ in size and functionalities to create a toolbox of novel material building-blocks. Examples in the literature clearly demonstrate how subtleties in fine-tuning the molecular structure can translate to macroscopic properties, rendering the ability to precisely design peptide-based materials to suit specific functions. This thesis aims to elucidate A) the use of coiled-coil design principles to create modular structural and functional tertiary motifs and, B) the construction of tunable hierarchical assemblies that can be harnessed for biological applications. Recent technological advances coupled with a wealth of newly developed strategies in peptide design, chemistry and assembly, are expanding our abilities to meet the ever-increasing need for functional biomaterials.

1.4 References

1. Saini, M.; Singh, Y.; Arora, P.; Arora, V.; Jain, K. Implant Biomaterials: A Comprehensive Review. *World J. Clin. Cases* **2015,** *3* (1), 52-57.

2. Deming, T. Peptide-Based Materials. In *Topics in Current* Chemistry; 1st ed.; Springer, Berlin, Heidelberg, 2012; Vol. 310, pp. 27-69.

3. Wilson, C. J.; Bommarius, A. S.; Champion, J. A.; Chernoff, Y. O.; Lynn, D. G.; Paravastu, A. K.; Liang, C.; Hsieh, M.-C.; Heemstra, J. M. Biomolecular Assemblies: Moving from Observation to Predictive Design. *Chem. Rev.* **2018,** *118* (24), 11519-11574.

4. Pieters, B. J. G. E.; Van Eldijk, M. B.; Nolte, R. J. M.; Mecinovi, J. Natural Supramolecular Protein Assemblies. *Chem. Soc. Rev.* **2015,** *45* (1), 24-39.

5. Lai, Y.-T.; King, N. P.; Yeates, T. O. Principles for Designing Ordered Protein Assemblies. *Trends Cell Biol.* **2012,** *22* (12), 653-661.

6. Fegan, A.; White, B.; Carlson, J. C. T.; Wagner, C. R. Chemically Controlled Protein Assembly: Techniques and Applications. *Chem. Rev.* **2010,** *110* (6), 3315-3336.

7. Bai, Y.; Luo, Q.; Liu, J. Protein Self-Assembly Via Supramolecular Strategies. *Chem. Soc. Rev.* **2016,** *45* (10), 2756-2767.

8. Castillo-León, J.; Sasso, L.; Svendsen, W. E. *Self-Assembled Peptide Nanostructures: Advances and Applications in Nanobiotechnology,* 1st ed.; CRC: Boca Raton, FL, 2012; pp. 39-259.

9. Zhao, X.; Pan, F.; Lu, J. R. Recent Development of Peptide Self-Assembly. *Prog. Nat. Sci.* **2008,** *18* (6), 653-660.

10. Woolfson, D. N. Building Fibrous Biomaterials from Alpha-Helical and Collagen-Like Coiled-Coil Peptides. *Biopolymers* **2010,** *94* (1), 118-127.

11. Przybyla, D. E.; Chmielewski, J. Higher-Order Assembly of Collagen Peptides into Nano- and Microscale Materials. *Biochemistry* **2010,** *49* (21), 4411-4419.

12. Durao, J.; Gales, L. Peptide Self-Assembly for Therapeutic Applications. *Curr. Org. Chem.* **2015,** *19* (19), 1874-1881.

13. Lupas, A. N.; Gruber, M. The Structure of a-Helical Coiled Coils. *Adv. Protein Chem.* **2005,** *70*, 37-78.

14. Beck, A. K.; Brodsky, B. Supercoiled Protein Motifs: The Collagen Triple-Helix and the a-Helical Coiled Coil. *J. Struct. Biol.* **1998,** *122*, 17-29.

15. Astbury, W. T. On the structure of biological fibres and the problem of muscle. *Proc. R. Soc. Lond. B. Biol. Sci.* **1947,** *134* (876), 303-328.

16. Parry, D. A.; Fraser, R. D.; Squire, J. M. Fifty Years of Coiled-Coils and Alpha-Helical Bundles: A Close Relationship between Sequence and Structure. *J. Struct. Biol.* **2008,** *163* (3), 258-269.

17. Crick, F. H. C. Is α-Keratin a Coiled Coil? *Nature* **1952,** *170* (4334), 882-883.

18. Mason, J. M.; Arndt, K. M. Coiled Coil Domains: Stability, Specificity, and Biological Implications. *ChemBioChem* **2004,** *5* (2), 170-176.

19. Pauling, L.; Corey, R. B.; Branson, H. R. The Structure of Proteins: Two Hydrogen-Bonded Helical Configurations of the Polypeptide Chain. *Proc. Natl. Acad. Sci. U. S. A.* **1951,** *37* (4), 205-211.

20. Stetefeld, J.; Jenny, M.; Schulthess, T.; Landwehr, R.; Engel, J.; Kammerer, R. A. Crystal Structure of a Naturally Occurring Parallel Right-Handed Coiled Coil Tetramer. *Nat. Struct. Biol.* **2000,** *7* (9), 772-776.

21. Woolfson, D. N. The Design of Coiled-Coil Structures and Assemblies. *Adv. Protein Chem.* **2005,** *70*, 79-112.

22. Woolfson, D. N.; Bartlett, G. J.; Bruning, M.; Thomson, A. R. New Currency for Old Rope: From Coiled-Coil Assemblies to Alpha-Helical Barrels. *Curr. Opin. Struct. Biol.* **2012,** *22* (4), 432-441.

23. Rhys, G. G.; Wood, C. W.; Lang, E. J. M.; Mulholland, A. J.; Brady, R. L.; Thomson, A. R.; Woolfson, D. N. Maintaining and Breaking Symmetry in Homomeric Coiled-Coil Assemblies. *Nat. Comm.* **2018,** *9* (1), 1-12.

24. O'Shea, E. K.; Rutowski, R.; Kim, P. S. Evidence That the Leucine Zipper Is a Coiled Coil. *Science* **1989,** *243*, 538-542.

25. Harbury, P. B.; Zhang, T.; Kim, P. S.; Alber, T. A Switch between Two-, Three-, and Four-Stranded Coiled Coils in GCN4 Leucine Zipper Mutants. *Science* **1993,** *262* (5138), 1401-1407.

26. Harbury, P. B.; Kim, P. S.; Alber, T. Crystal Structure of an Isoleucine-Zipper Trimer. *Nature* **1994,** *371*, 80-83.

27. Walshaw, J.; Woolfson, D. N. Extended Knobs-into-Holes Packing in Classical and Complex Coiled-Coil Assemblies. *J. Struct. Biol.* **2003,** *144* (3), 349-361.

28. Nathan, R. Z.; Bertie, C.; Andrew, R. T.; Aimee, L. B.; Gail, J. B.; Marc, B.; Noah, L.; Richard, B. S.; Paula, J. B.; Brady, R. L.; Derek, N. W. A De Novo Peptide Hexamer with a Mutable Channel. *Nat. Chem. Biol.* **2011,** *7* (12), 935-941.

29. Alan, J. K. Protein Structure: Charting a New Course in Coiled Coils. *Nat. Chem. Biol.* **2011,** *7* (12), 859-860.

30. Liu, J.; Zheng, Q.; Deng, Y.; Cheng, C.; Kallenbach, N.; Lu, M. A Seven-Helix Coiled Coil. *Proc. Natl. Acad. Sci. U. S. A.* **2006,** *103* (42), 15457-15462.

31. Boyle, A. L.; Woolfson, D. N. De Novo Designed Peptides for Biological Applications. *Chem. Soc. Rev.* **2011,** *40*, 4295-4306.

32. Ryadnov, M.; Woolfson, D. Engineering the Morphology of a Self-Assembling Protein Fibre. *Nat. Mater.* **2003,** *2* (5), 329-332.

33. Pandya, M. J.; Spooner, C. M.; Sunde, M.; Thorpe, J. R.; Rodger, A.; Woolfson, D. N. Sticky-End Assembly of a Designed Peptide Fiber Provides Insight into Protein Fibrillogenesis. *Biochemistry* **2000,** *39* (30), 8728-8734.

34. Smith, A. M.; Banwell, E. F.; Edwards, W. R.; Pandya, M. J.; Woolfson, D. N. Engineering Increased Stability into Self-Assembled Protein Fibers. *Adv. Funct. Mater.* **2006,** *16* (8), 1022-1030.

35. Papapostolou, D.; Smith, A. M.; Atkins, E. D. T.; Oliver, S. J.; Ryadnov, M. G.; Serpell, L. C.; Woolfson, D. N. Engineering Nanoscale Order into a Designed Protein Fiber. *Proc. Natl. Acad. Sci. U. S. A.* **2007,** *104* (26), 10853-10858.

36. Gribbon, C.; Channon, K. J.; Zhang, W.; Banwell, E. F.; Bromley, E. H. C.; Chaudhuri, J. B.; Oreffo, R. O. C.; Woolfson, D. N. Magicwand: A Single, Designed Peptide That Assembles to Stable, Ordered Alpha-Helical Fibers. *Biochemistry* **2008,** *47* (39), 10365-10371.

37. Mahmoud, Z. N.; Gunnoo, S. B.; Thomson, A. R.; Fletcher, J. M.; Woolfson, D. N. Bioorthogonal Dual Functionalization of Self-Assembling Peptide Fibers. *Biomaterials* **2011,** *32* (15), 3712-3720.

38. Mahmoud, Z.; Grundy, D.; Channon, K.; Woolfson, D. The Non-Covalent Decoration of Self-Assembling Protein Fibers. *Biomaterials* **2010,** *31* (29), 7468-7474.

39. Zimenkov, Y.; Dublin, S. N.; Ni, R.; Tu, R. S.; Breedveld, V.; Apkarian, R. P.; Conticello, V. P. Rational Design of a Reversible pH-Responsive Switch for Peptide Self-Assembly. *J. Am. Chem. Soc.* **2006,** *128*, 6770-6771.

40. Dublin, S. N.; Conticello, V. P. Design of a Selective Metal Ion Switch for Self-Assembly of Peptide-Based Fibrils. *J. Am. Chem. Soc.* **2007,** *130*, 49-51.

41. Anzini, P.; Xu, C.; Hughes, S.; Magnotti, E.; Jiang, T.; Hemmingsen, L.; Demeler, B.; Conticello, V. P. Controlling Self-Assembly of a Peptide-Based Material Via Metal-Ion Induced Registry Shift. *J. Am. Chem. Soc.* **2013,** *135* (28), 10278-10281.

42. Gunasekar, S. K.; Anjia, L.; Matsui, H.; Montclare, J. K. Effects of Divalent Metals on Nanoscopic Fiber Formation and Small Molecule Recognition of Helical Proteins. *Adv. Funct. Mater.* **2012,** *22* (10), 2154-2159.

43. More, H. T.; Zhang, K. S.; Srivastava, N.; Frezzo, J. A.; Montclare, J. K. Influence of Fluorination on Protein-Engineered Coiled-Coil Fibers. *Biomacromolecules* **2015,** *16* (4), 1210-1217.

44. Hume, J.; Sun, J.; Jacquet, R.; Renfrew, P. D.; Martin, J. A.; Bonneau, R.; Gilchrist, M. L.; Montclare, J. K. Engineered Coiled-Coil Protein Microfibers. *Biomacromolecules* **2014,** *15* (10), 3503-3510.

45. Tsurkan, M. V.; Ogawa, M. Y. Formation of Peptide Nanospheres and Nanofibrils by Metal Coordination. *Biomacromolecules* **2007,** *8*, 3908-3913.

46. Zhou, M.; Bentley, D.; Ghosh, I. Helical Supramolecules and Fibers Utilizing Leucine Zipper-Displaying Dendrimers. *J. Am. Chem. Soc.* **2004,** *126* (3), 734-735.

47. Egelman, E. H.; Xu, C.; DiMaio, F.; Magnotti, E.; Modlin, C.; Yu, X.; Wright, E.; Baker, D.; Conticello, V. P. Structural Plasticity of Helical Nanotubes Based on Coiled-Coil Assemblies. *Structure* **2015,** *23* (2), 280-289.

48. Wu, Y.; Norberg, P. K.; Reap, E. A.; Congdon, K. L.; Fries, C. N.; Kelly, S. H.; Sampson, J. H.; Conticello, V. P.; Collier, J. H. A Supramolecular Vaccine Platform Based on A-Helical Peptide Nanofibers. *ACS Biomater. Sci. & Eng.* **2017,** *3* (12), 3128-3132.

49. Xu, C.; Liu, R.; Mehta, A. K.; Guerrero-Ferreira, R. C.; Wright, E. R.; Dunin-Horkawicz, S.; Morris, K.; Serpell, L. C.; Zuo, X.; Wall, J. S.; Conticello, V. P. Rational Design of Helical Nanotubes from Self-Assembly of Coiled-Coil Lock Washers. *J. Am. Chem. Soc.* **2013,** *135* (41), 15565-15578.

50. Xu, C.; Liu, R.; Mehta, A. K.; Guerrero-Ferreira, R. C.; Wright, E. R.; Dunin-Horkawicz, S.; Morris, K.; Serpell, L. C.; Zuo, X.; Wall, J. S.; Conticello, V. P. Rational Design of Helical Nanotubes from Self-Assembly of Coiled-Coil Lock Washers. *J. Am. Chem. Soc.* **2013,** *135* (41), 15565-15578.

51. Thomas, F.; Burgess, N. C.; Thomson, A. R.; Woolfson, D. N. Controlling the Assembly of Coiled-Coil Peptide Nanotubes. *Angew. Chem. Int. Ed.* **2016,** *55*, 987-991.

52. Burgess, N. C.; Sharp, T. H.; Thomas, F.; Wood, C. W.; Thomson, A. R.; Zaccai, N. R.; Brady, R. L.; Serpell, L. C.; Woolfson, D. N. Modular Design of Self-Assembling Peptide-Based Nanotubes. *J. Am. Chem. Soc.* **2015,** *137* (33), 10554-10562.

53. Tian, Y.; Polzer, F. B.; Zhang, H. V.; Kiick, K. L.; Saven, J. G.; Pochan, D. J. Nanotubes, Plates, and Needles: Pathway-Dependent Self-Assembly of Computationally Designed Peptides. *Biomacromolecules* **2018,** *19* (11), 4286-4298.

54. Petka, W.; Harden, J.; McGrath, K.; Wirtz, D.; Tirrell, D. Reversible Hydrogels from Self-Assembling Artificial Proteins. *Science* **1998,** *281* (5375), 389-392.

55. Xu, C.; Kopeček, J. Genetically Engineered Block Copolymers: Influence of the Length and Structure of the Coiled-Coil Blocks on Hydrogel Self-Assembly. *AAPS J.* **2008,** *25* (3), 674-682.

56. Wei, S.; Kechun, Z.; Julia, A. K.; David, A. T. Tuning the Erosion Rate of Artificial Protein Hydrogels through Control of Network Topology. *Nat. Mater.* **2006,** *5* (2), 153-158.

57. Wang, C.; Stewart, R. J.; Kopecek, J. Hybrid Hydrogels Assembled from Synthetic Polymers and Coiled-Coil Protein Domains. *Nature* **1999**, 417-420.

58. Yao, M.-H.; Yang, J.; Du, M.-S.; Song, J.-T.; Yu, Y.; Chen, W.; Zhao, Y.-D.; Liu, B. Polypeptide-Engineered Physical Hydrogels Designed from the Coiled-Coil Region of Cartilage Oligomeric Matrix Protein for Three-Dimensional Cell Culture. *J. Mater. Chem. B* **2014,** *2* (20), 3123-3132.

59. Kopeček, J. Hydrogel Biomaterials: A Smart Future? *Biomaterials* **2007,** *28* (34), 5185-5192.

60. Banwell, E. F.; Abelardo, E. S.; Adams, D. J.; Birchall, M. A.; Corrigan, A.; Donald, A. M.; Kirkland, M.; Serpell, L. C.; Butler, M. F.; Woolfson, D. N. Rational Design and Application of Responsive Alpha-Helical Peptide Hydrogels. *Nat. Mater.* **2009,** *8*, 596-600.

61. Huang, C.-C.; Ravindran, S.; Yin, Z.; George, A. 3-D Self-Assembling Leucine Zipper Hydrogel with Tunable Properties for Tissue Engineering. *Biomaterials* **2014,** *35* (20), 5316-5326.

62. Mehrban, N.; Zhu, B.; Tamagnini, F.; Young, F. I.; Wasmuth, A.; Hudson, K. L.; Thomson, A. R.; Birchall, M. A.; Randall, A. D.; Song, B.; Woolfson, D. N. Functionalized A-Helical Peptide Hydrogels for Neural Tissue Engineering. *ACS Biomater. Sci. & Eng.* **2015,** *1* (6), 431-439.

63. Fletcher, J. M.; Harniman, R. L.; Barnes, F. R. H.; Boyle, A. L.; Collins, A.; Mantell, J.; Sharp, T. H.; Antognozzi, M.; Booth, P. J.; Linden, N.; Miles, M. J.; Sessions, R. B.; Verkade, P.; Woolfson, D. N. Self-Assembling Cages from Coiled-Coil Peptide Modules. *Science* **2013,** *340*, 595-599.

64. Lomander, A.; Hwang, W.; Zhang, S. Hierarchical Self-Assembly of a Coiled-Coil Peptide into Fractal Structure. *Nano Lett.* **2005,** *5*, 1255-1260.

65. Ryadnov, M. G. A Self-Assembling Peptide Polynanoreactor. *Angew. Chem., Int. Ed.* **2007,** *46* (6), 969-972.

66. Helena, G.; Sabina, B.; Tibor, D.; Damjan, V.; Iva, H.-B.; Alenka, M.; Ben, W.; Andrej, Š.; Sandi, K.; Roman, J. Design of a Single-Chain Polypeptide Tetrahedron Assembled from Coiled-Coil Segments. *Nat. Chem. Biol.* **2013,** *9* (6), 362-366.

67. Nepal, M.; Sheedlo, M. J.; Das, C.; Chmielewski, J. Accessing Three-Dimensional Crystals with Incorporated Guests through Metal-Directed Coiled-Coil Peptide Assembly. *J. Am. Chem. Soc.* **2016,** *138* (34), 11051-11057.

68. Nambiar, M.; Wang, L.-S.; Rotello, V.; Chmielewski, J. Reversible Hierarchical Assembly of Trimeric Coiled-Coil Peptides into Banded Nano- and Micro- Structures. *J. Am. Chem. Soc.* **2018,** *140* (40), 13028-13033.

CHAPTER 2. pH-REVERSIBLE HIGHER-ORDER ASSEMBLY OF COILED-COIL TRIMERS INTO BANDED MICROSTRUCTURES FOR DRUG-DELIVERY APPLICATIONS

2.1 Introduction

A primary requisite of synthetic biomaterials lies in their ability to mimic and adapt to naturally occurring biological molecules and systems. Whereas the sequential building blocks of most self-assembling peptide systems are different, their hierarchical molecular assemblies are generally held together by weak intermolecular forces. These interactions can be triggered by an external stimulus[1-4] and are, in some instances, reversible with pH,[5-8] temperature[9-18] and enzyme action.[19, 20] Among these environmental stimuli, pH-responsive properties are often incorporated into potential biomaterial designs for drug-delivery systems.[21]

Different organs, tissues and sub-cellular compartments can be characterized by their pH gradients. Many cancer tissues display an acidic extracellular pH within the tumor microenvironment, primarily due to lactate secretion from anaerobic glycolysis.[22, 23] pH variation is also observed during normal cell endocytosis when foreign material is engulfed by the cell into endosomal compartments, which undergo acidification to below physiological pH. These types of pH changes across different biological environments can be leveraged to design treatment strategies that are site-specific. Such modes of targeted therapy, especially with anti-cancer drugs, would be more effective and exhibit less adverse effects in comparison to conventional, systemic delivery methods. Commonly reported materials involve the use of synthetic polymers that are quite effective in protecting their fragile cargo.[24-26] However, these materials are limited by their inability to evade the immune system and lack of biodegradability. This can however, be overcome by substituting the core building-blocks with self-assembling peptides, while simultaneously

endowing them with pH-programmable molecular cues. This type of dynamic molecular control justifies the appeal of such systems for the creation of stimuli-responsive peptide materials.

A limited number of pH-switchable coiled-coil systems have been previously described, where in fibers[5] and hydrogels[7] have exhibited reversible assembly on cue. Coiled-coil peptides also offer benefits that include well-established design principles, facile synthesis as well as accessibility to multiple oligomeric states. Herein, we describe bipyridine-modified coiled-coil peptides that demonstrate self-assembly that can be reversibly controlled as a function of pH.

2.2 Results and Discussion

2.2.1 Peptide Design

Our choice of peptide sequence is based on the well-studied GCN4 leucine zipper motif.[27, 28] It has been established that the substitution of leucine residues with isoleucine in the *a* and *d* positions of the GCN4 sequence (Figure 2.1 A, helical wheel diagram), affords a trimeric coiled coil, with all three helices in a parallel orientation relative to each other.[27] We strategically placed hydrophobic groups on the polar face of the coiled-coil, in the solvent exposed *f* position, to permit inter-trimer interactions across coiled-coils. Specifically, we employed bipyridine moieties to mediate these interactions to promote higher-order assembly. The use of bipyridines enables a potential dual use of this moiety for aromatic interactions as well as enabling pH-sensitive control of assembly.

The design used in these studies features three peptide sequences, each with a varying number of bipyridines along the peptide backbone - **TriByp1** with one bipyridine at position 13, **TriByp2** with bipyridines at positions 13 and 20, and **TriByp3** with bipyridines at positions 6, 13 and 20 (Figure 2.1 B). Each of these monomers would fold into trimers with 3, 6 and 9 bipyridines, respectively. We hypothesized that with an increase in the number of bipyridines along the length

of the coiled-coil, there would be a corresponding increase in the degree of radially-directed inter-coil interactions.

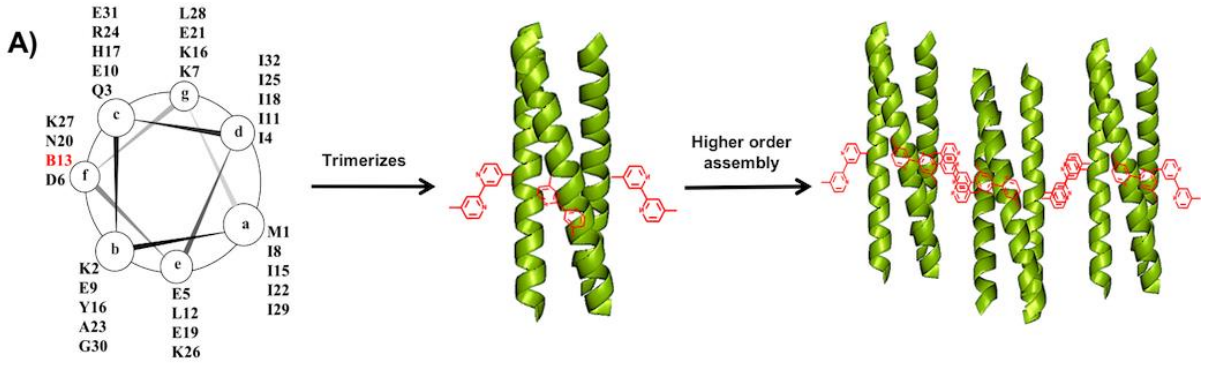

B)

Monomer	*abcdefg*	*abcdefg*	*abcdefg*	*abcdefg*	*abc*
TriByp1	Ac-MKQIEDK	IEEIL**B**K	IYHIENE	IARIKKL	IGE-NH_2
TriByp2	Ac-MKQIEDK	IEEIL**B**K	IYHIE**B**E	IARIKKL	IGE-NH_2
TriByp3	Ac-MKQIE**B**K	IEEIL**B**K	IYHIE**B**E	IARIKKL	IGE-NH_2

B = Lysine functionalized with bipyridine

Figure 2.1 The design of coiled-coil peptide assembly depicting A) helical wheel arrangement of an individual alpha helix leading to coiled-coil folding with subsequent higher-order assembly and, B) sequential representation of amino acids for each monomer sequence.

2.2.2 Synthesis of bipyridine moiety (Byp) - 4’-methyl-2,2’-bipyridine-4-carboxylic acid

4’-methyl-2,2’-bipyridine-4-carboxylic acid was synthesized using an established protocol.[29] The synthesis proceeds via two steps – i) conversion of starting material **(1)** to the monoaldehyde **(2)** via oxidation in the presence of selenium dioxide and, ii) subsequent conversion in the presence of silver nitrate and sodium hydroxide to the desired carboxylic acid derivative **(3)** (Scheme 2.1).

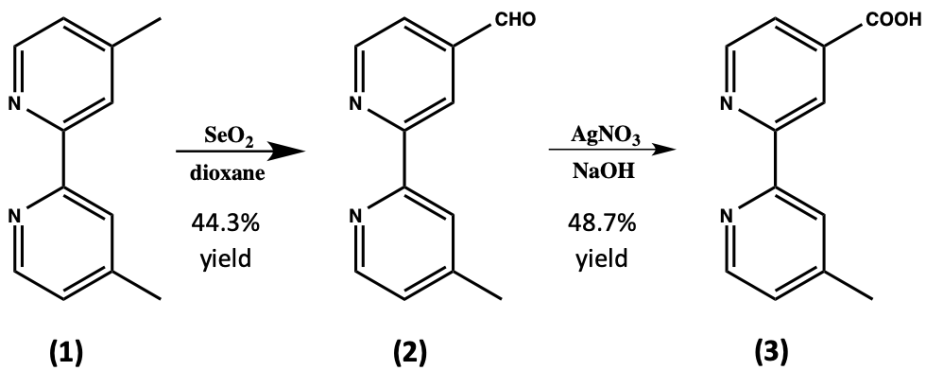

Scheme 2.1 Reaction scheme outlining the synthesis of 4'-methyl-2,2'-bipyridine-4-carboxylic acid.

2.2.3 Synthesis of Bipyridine-Modified Coiled-Coil Peptides

The peptides - **TriByp1**, **TriByp2** and **TriByp3** were synthesized using solid phase peptide synthesis (SPPS) with a low-loading ChemMatrix® rink amide resin as the solid support. Fmoc amino acids were coupled with the aid of the HBTU coupling agent and DIEA. Fmoc-Lys-Mtt residues were substituted at the specified *f* positions in the coiled-coil heptad, as per the design, in order to facilitate selective functionalization with the aromatic group, 4'-methyl-2,2'-bipyridine-4-carboxylic acid-**(3)**. Following the synthesis of the primary sequence, the sidechain protected Mtt groups were removed on resin under mild acidic conditions (30% HFIP in DCM), followed by the treatment with (**3**), HBTU and DIEA. The peptides were cleaved from resin with a trifluoroacetic acid cocktail, purified to homogeneity and characterized with matrix-assisted laser desorption ionization time of flight (MALDI-TOF) mass spectrometry.

2.2.4 Structural Characterization of Bipyridine-Modified Coiled-Coils

The decoration of the coiled-coil peptides with the bulky bipyridine groups could potentially disrupt their ability to fold into a helical coiled-coil trimer. To determine the secondary structure of the peptides, circular dichroism spectra were obtained, with an emphasis in the far-UV (190-250 nm) region. The CD measurement was performed at low pH (10 mM citrate buffer - pH

3.0) to avoid the possibility of assembly at higher pH values. All four peptides displayed a helical structure, indicated by the two negative absorption bands at 222 nm and 208 nm and a positive absorption band at 194 nm (Figure 2.2). It is worth noting that the magnitude of absorption at 222 nm is higher than that at 208 nm ($\theta_{222}/\theta_{208} \geq 1$), which has been shown to be indicative of the presence of a coiled-coil.[30] The level of helicity, as determined by the mean residue ellipticity value at 222 nm, was approximately 50-60% for all peptides.[31, 32] The native GCN4 trimer has been shown to be about 90% helical,[33, 34] suggesting that the incorporation of bipyridines decreases helical content, but does not preclude the formation of the alpha helix.

The oligomerization state of the trimers was further corroborated using sedimentation velocity analytical ultracentrifugation. Sedimentation coefficient distribution analysis indicates that the predominant oligomer (>80%) in all three peptide samples is a trimer (Figure 2.3). These results indicate that, despite the bipyridine functionalization of the peptides, the modified coiled-coil trimers maintained their structural integrity.

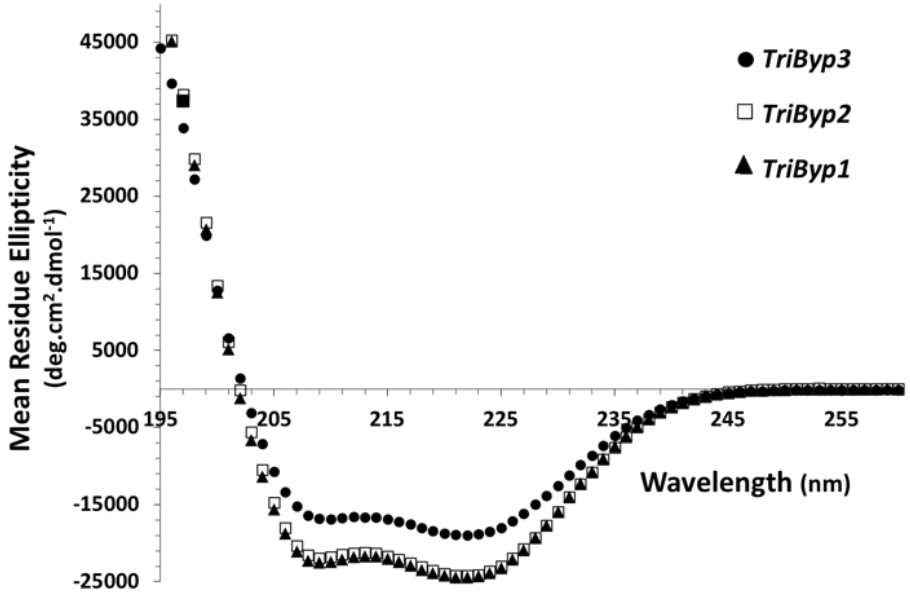

Figure 2.2 CD spectra of the coiled-coil peptides (100 µM) measured at pH 3.0 (10 mM citrate buffer).

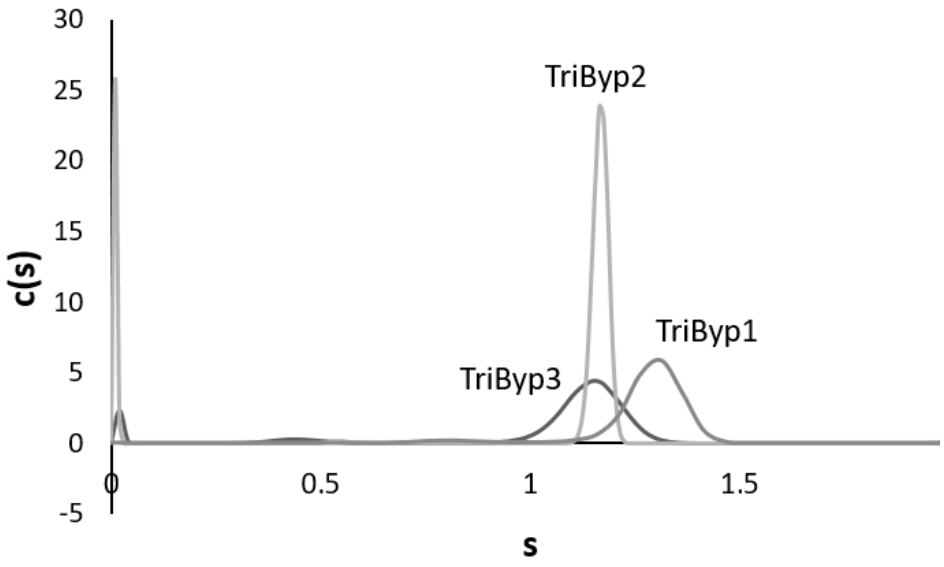

Figure 2.3 Analytical ultracentrifugation (AUC) analysis of the three coiled-coil peptides to verify their trimeric aggregation

2.2.5 Formation and Visualization of Coiled-Coil Trimer Assemblies

To achieve higher-order assembly, the peptides **TriByp1**, **TriByp2** and **TriByp3** (250 μM) were suspended in 10 mM MOPS buffer (pH 7.0) and incubated for 48 hours at room temperature. A colorless precipitate was formed in each case, which was collected by centrifugation, washed and suspended in water. The assemblies were visualized using scanning electron microscopy (SEM) and transmission electron microscopy (TEM). The trimers were observed to collectively adopt the appearance of striated rectangular blocks (Figure 2.4). The striation manifests itself in a repetitive banding pattern, noticeable from the TEM data (Figure 1.4 D-F). The banding distance, measured by performing fast Fourier transform (FFT) analysis, was 4.4 nm (Figure 2.5). This value was consistent across all trimer assemblies.

Varying dimensions were observed for the three different peptide assemblies with a noticeable difference in the aspect ratio of these structures across the trimers. For instance, **TriByp1** assemblies containing 3 bipyridines per trimer (Figure 2.4 A & D), were in the range of

30-150 nm wide (parallel to the direction of banding) and 200 nm-4 μm in length (the direction perpendicular to the banding), with an aspect ratio (length:width) of 16:1. **TriByp2**, consisting of 6 bipyridines within the coiled-coil, assumed a similar morphology as **TriByp1** (Figure 2.4 B & E), but the nano-assemblies were significantly shorter in the direction perpendicular to the banding, with the length in the range of 90-400 nm and an aspect ratio of 4:1. Correspondingly, with an increase in the number of bipyridines to 9 per trimer, the **TriByp3** nano-assemblies (Figure 2.4 C & F) displayed a slight overall decrease in length compared to **TriByp2**, but with a more significant increase in block width. Structures as wide as 300 nm were observed with the overall shape being more square-like. Thus, it is evident that with the sequential increase in the number of bipyridines from 3 through to 9 for each coiled-coil, the dimensions of the assembly change from rectangular micro-blocks to square shaped nano-blocks (Table 2.1). This change in aspect ratio supports our initial design that a higher number of radially positioned hydrophobic groups would have a higher propensity for individual coiled-coils to associate alongside each other (lateral assembly). For instance, enhanced lateral assembly of the trimeric coiled-coils with increased number of bipyridines was observed.

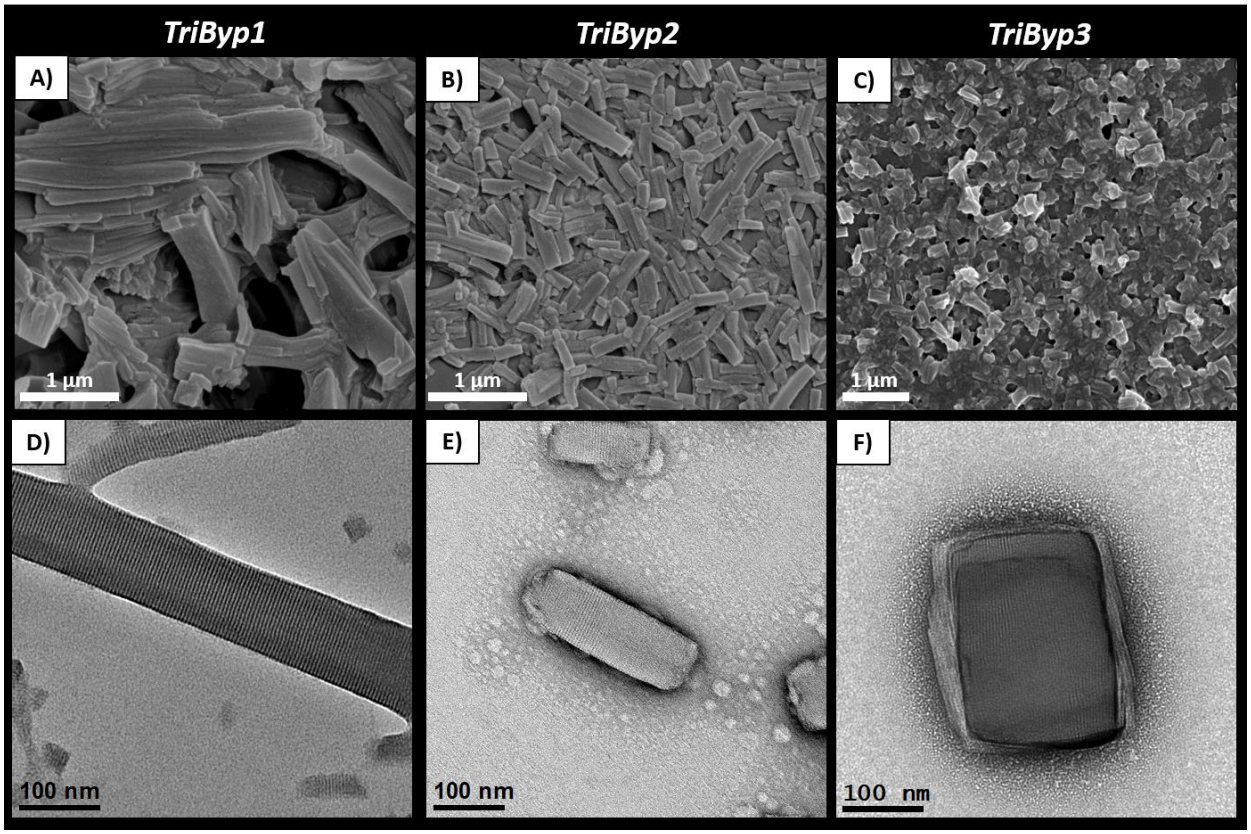

Figure 2.4 SEM images (A-C) and TEM micrographs (D-F) of the coiled-coil assemblies formed from **TriByp1**, **TriByp2** and **TriByp3** (250 µM), formed in 10 mM MOPS buffer (pH 7.0) at room temperature.

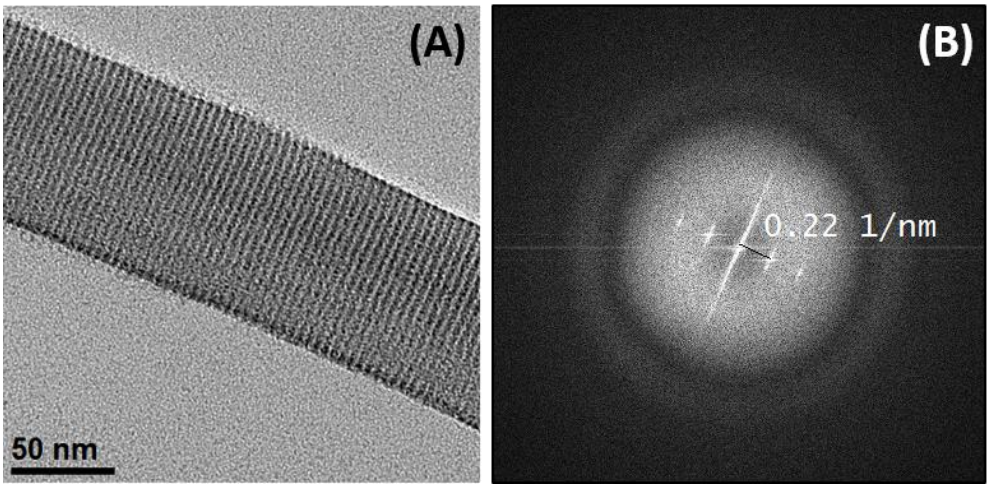

Figure 2.5 TEM image of **TriByp1** (A) and its corresponding fast fourier transform (FFT) (B) which shows the banding distance (4.5 nm) in reciprocal space (0.22 1/nm).

Table 2.1 Dimensional aspect ratios and height measurements of the assemblies

	Length (l)-nm	Width (w)-nm	Aspect ratio (l:w)	Height (h)-nm
TriByp1	200-4000 (*n* = 15)	30-150 (*n* = 15)	16:1	72 ± 47 (*n* = 5)
TriByp2	90-400 (*n* = 15)	45-70 (*n* = 15)	4:1	30 ± 20 (*n* = 5)
TriByp3	90-200 (*n* = 15)	50-300 (*n* = 15)	0.9:1	75 ± 35 (*n* = 5)

n = no. of structures for which measurements were taken

Tapping-mode AFM also suggests a similar morphology for the assemblies, as obtained with TEM and SEM (Figure 2.6). Cross-sectional analysis of the AFM images was conducted to measure the height or thickness of these structures (Table 2.1). The broad distribution and similar range of measured thickness across the three types of assemblies, suggests a limited variation in thickness, except for a somewhat smaller height observed for the **TriByp2** nanostructures. There is definite stacking morphology that is observed in the **TriByp3** structures (Figure 2.4 F), perhaps due to the additional bipyridine groups on the coiled-coil trimer, that is not observed with **TriByp2**.

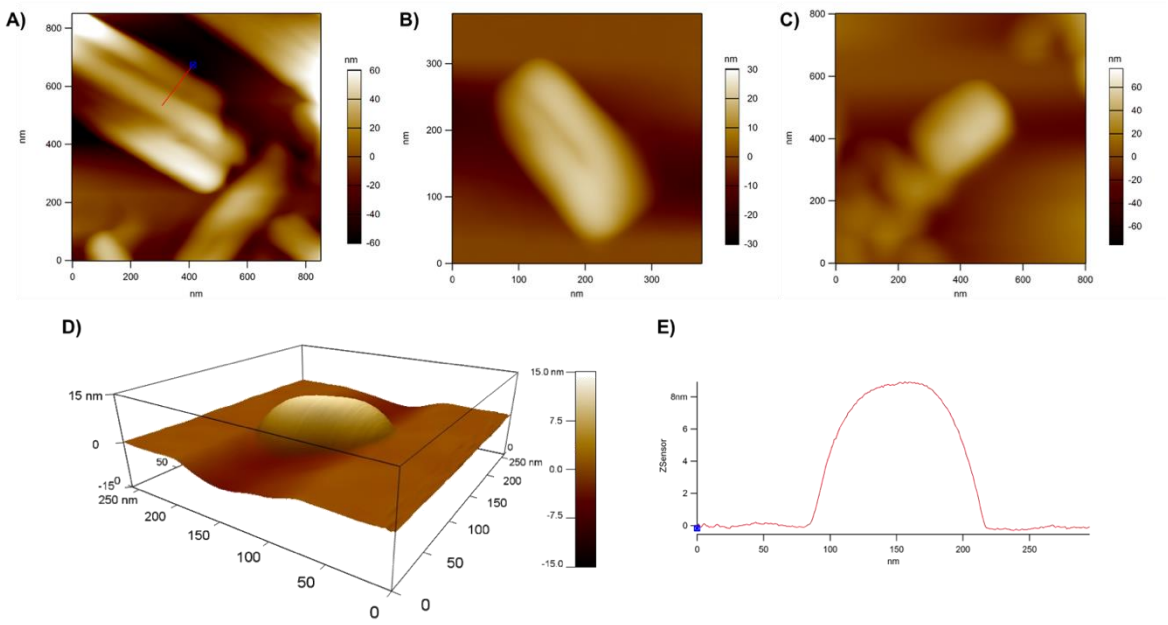

Figure 2.6 Tapping mode-AFM height images of **TriByp1** (A), **TriByp2** (B) and **TriByp3** (C), obtained at concentrations of 250uM in 10mM MOPS buffer. 3D projection of **TriByp2** (D) and, (E) cross-sectional analysis to show height of assembly measured to be 9 nm.

Bipyridines are well known to chelate a variety of metal ions. Hence, arguably metal-ion coordination could potentially instigate the higher-order assembly observed. To confirm that the formation of these hierarchical structures take place in the absence of metal, the three assemblies were treated with EDTA, a metal-chelating ligand. After treatment, the assemblies remained intact with no change in morphology. Additionally, EDX analysis of the nanostructures obtained with **TriByp2**, for instance, further substantiated the lack of metal ions in the assembly, with only baseline levels of metals such as iron and cobalt observed (Figure 2.7). The bipyridine-modified coiled-coil assemblies were also observed to be stable in the presence of metal ions and phosphate buffer, without undergoing any appreciable change, thus, substantiating their potential for biological applications.

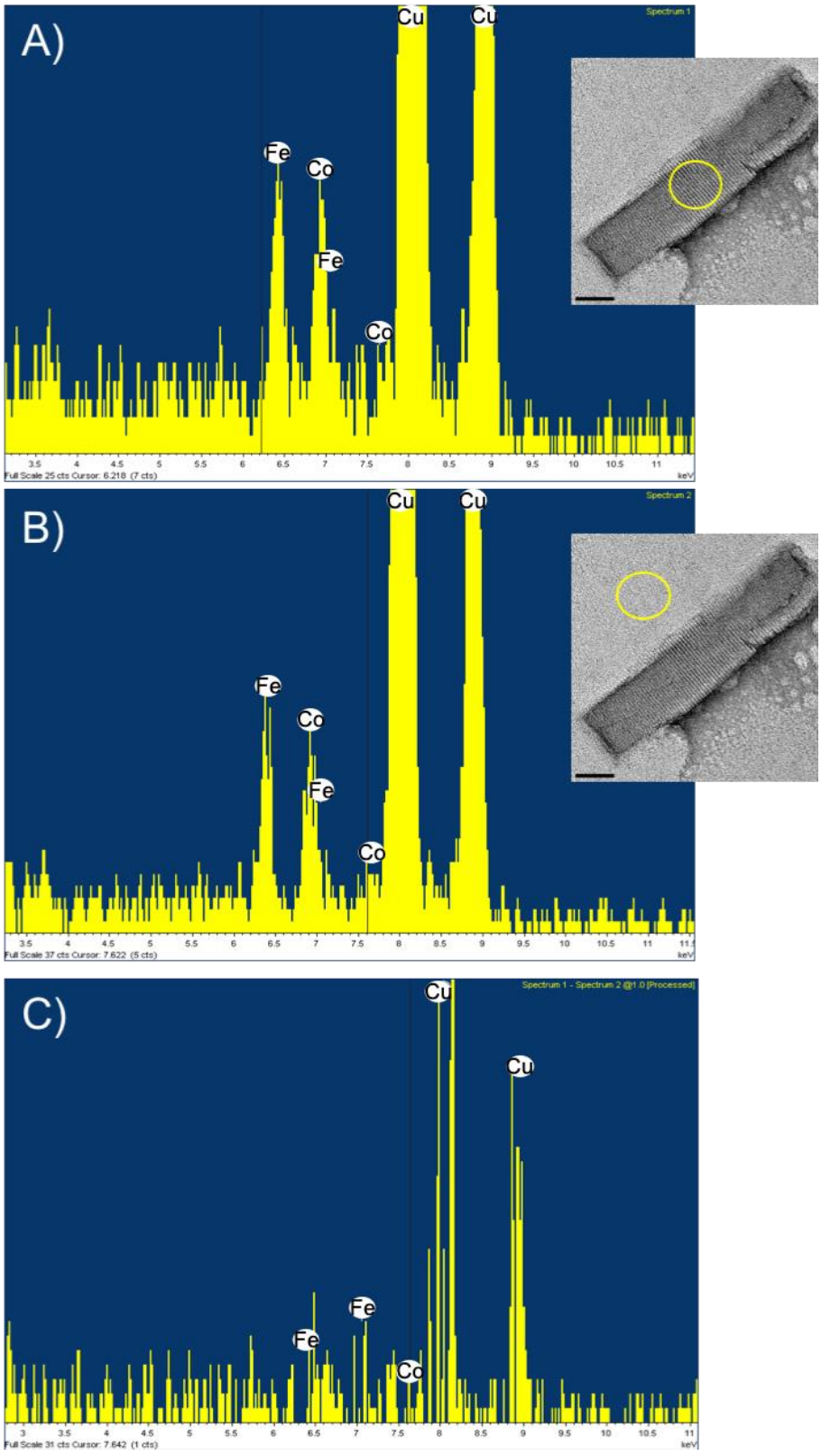

Figure 2.7 TEM-EDX analysis of **TriByp2**: A) nanostructure, B) background and, C) background (B) subtracted from microstructure (A) (scale bar = 100 nm)

2.2.6 Structural Elucidation of Assemblies

For all three peptide assemblies, the coiled-coils are the building block for hierarchical growth. Therefore, to determine the coiled-coil packing within these assemblies, medium and wide-angle X-ray scattering profiles (MAXS and WAXS, respectively) were obtained. In the MAXS data (Figure 2.8 A), a peak with a q-value of 0.14 $Å^{-1}$ was observed that corresponds to a d-spacing of 4.4 nm. This spacing corresponds to the length of the coiled-coil trimer as shown in Figure 2.8 B. This spacing also corresponds to the banding distance of 4.4 nm obtained from the FFT analysis of the TEM data (Figure 2.5). The q values of 0.25 corresponds to the second-order spot also observed in the TEM analysis (Figure 2.5). The q values 0.33 $Å^{-1}$ and 0.58 $Å^{-1}$ and 0.67 $Å^{-1}$ obtained from both the MAXS and WAXS data (Figure 2.8A and 2.8B), correspond to *d*-spacings of 1.85 nm, 1.07 nm and 0.93 nm respectively. Each of these represent the (100), (110) and (200) lattice planes, with a lattice parameter of 2.19 nm. These values suggest two possible packing arrangements, (i) a hexagonal close-packed (hcp) model (Figure 2.8 D) or (ii) a hexagonal honey-comb model. Although the latter model accommodates the three-fold symmetry predicted for coiled-coil trimers as well as the antiparallel orientation of adjacent helices, as observed in our earlier work,[35] the small lattice parameter of 2.19 nm suggests the probability of a more compact hcp arrangement, similar to that observed for fibers formed from coiled-coil dimers.[36]

Sub-nanometer *d*-spacings of 0.5 nm and 0.45 nm were also obtained from the WAXS data (Figure 2.8 B). These values could correspond to electrostatic and cation-π interactions between adjacent coiled-coils, within the assemblies. Additionally, electrostatic and hydrogen bonding interactions, encompassing the *b* and *c* positions between coiled-coils, may also serve to stabilize the resulting assemblies.[35]

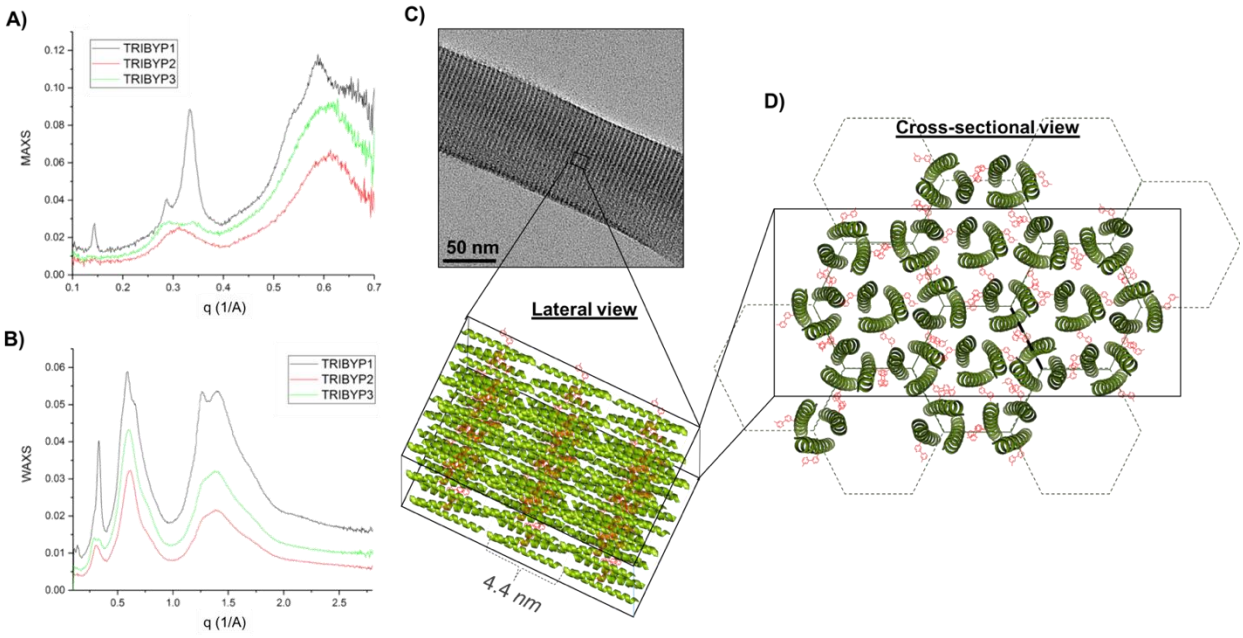

Figure 2.8 MAXS and WAXS analysis of the coiled-coil trimers to determine helical packing within the assemblies: A) MAXS profile of coiled-coil trimer assemblies, B) WAXS profile of coiled-coil trimer assemblies, C) TEM image of **TriByp1** with inset depicting the coiled-coil trimer packing within the microstructure and, D) cross-sectional view depicting hexagonal close-packing of coiled-coils with inset depicting inter-trimer aromatic interactions.

2.2.7 Dynamic Light Scattering Analysis

The proposed aromatic interactions between the bipyridine groups within the peptide assemblies have the potential to be disrupted by protonation of the bipyridines at acidic pH. To probe if the assembly could be controlled by pH, DLS measurements of the assemblies under both acidic and neutral conditions were performed (Figure 2.9). At pH 7.0, the peptides suspended in 10 mM MOPS buffer, exhibited higher order assembly with hydrodynamic radii ranging from several hundred nanometers to about a micron. At pH 3.0 (10 mM glycine-HCl buffer), the hydrodynamic radius of each coiled-coil trimer was about 2-3 nm, a value that is consistent with the trimeric peptides in its unassembled state.[27] This result may be due to protonation of the bipyridines in the more acidic environment, disfavoring trimer-trimer interactions and thereby, perturbing higher-order assembly.

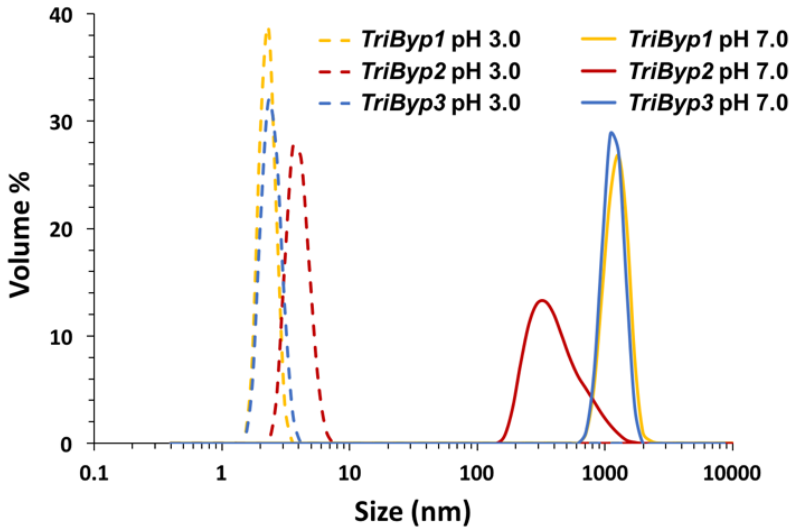

Figure 2.9 Dependence of modified coiled-coil peptide assembly (250 µM) on pH (10 mM MOPS, pH 7.0 and 10 mM glycine-HCl, pH 3.0).

It is worth noting that these DLS measurements were acquired within minutes of initiating the assembly with buffer, which indicates that at pH 7.0, these microstructures grow rapidly. This rapid formation was further verified with TEM, which showed clear formation of well-ordered rectangular microstructures taken 2 hours after initiating assembly (Figure 2.10). The size distribution for the **TriByp2** assemblies at pH 7.0 is relatively smaller in comparison to that of **TriByp1** and **TriByp3**. This size difference is also corroborated by the electron microscopy and AFM data for **TriByp2** assemblies, which exhibited smaller overall dimensions.

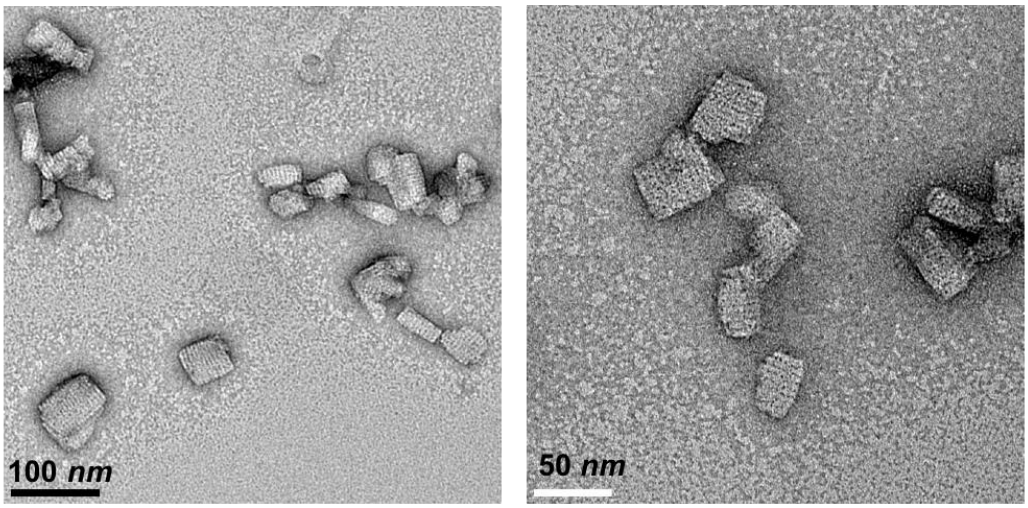

Figure 2.10 Formation of rectangular nanostructures after 2 hours of assembly. Representative example of **TriByp3** (250 μM) in 10 mM MOPS buffer

We further investigated pH as a reversible control element in coiled-coil hierarchical assembly. We wished to probe if the assembly was reversible with pH over several cycles. As such we monitored the change in size of the **TriByp1**, **TriByp2** & **TriByp3** assemblies by DLS, by shuttling the pH from neutral to acidic pH and back, over the course of two minutes (Figure 2.11). Interestingly, pre-formed assemblies quickly reverted to monomeric coiled-coils when subjected to acidic pH. Cycling back to neutral pH allowed the assemblies to reform, with greater than 99% sample recovery at the end of each cycle. These data demonstrate successful regeneration of the nanostructures with repeated disassembly and reformation over three pH cycles.

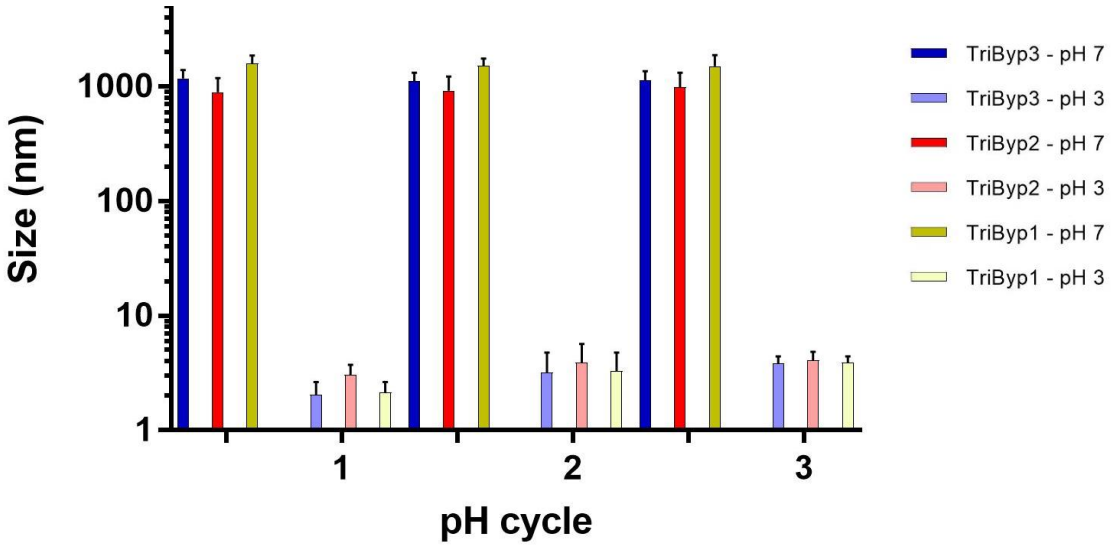

Figure 2.11 Reversible assembly of **TriByp1**, **TriByp2** and **TriByp3** demonstrated by repeated shuttling of pH from 7.0 to 3.0 over three cycles.

2.2.8 Non-Covalent Binding of Small Molecules

The **TriByp** peptide assemblies contain many charged and aromatic residues that can be harnessed for the non-covalent binding of organic molecules, thus providing scope for the docking of a wide-variety of small molecule drugs. Doxorubicin (DOX), an anthracycline antibiotic, has been used in the treatment of various cancers. It is also a highly conducive tool for research due to its inherent fluorescence.[37] Its planar aromatic and cationic moieties as well as its low molecular weight make it a suitable choice of cargo for binding to the **TriByp** assemblies. **TriByp1, TriByp2** and **TriByp3** peptides (500 μM) were assembled in MOPS buffer (10 mM, pH 7.0)) in the presence of DOX (1 mM, 24 hours). All three peptide assemblies displayed binding affinities to doxorubicin, to form **TriByp1**-DOX, **TriByp2**-DOX and **TriByp3**-DOX fluorescent assemblies. (Figure 2.12).

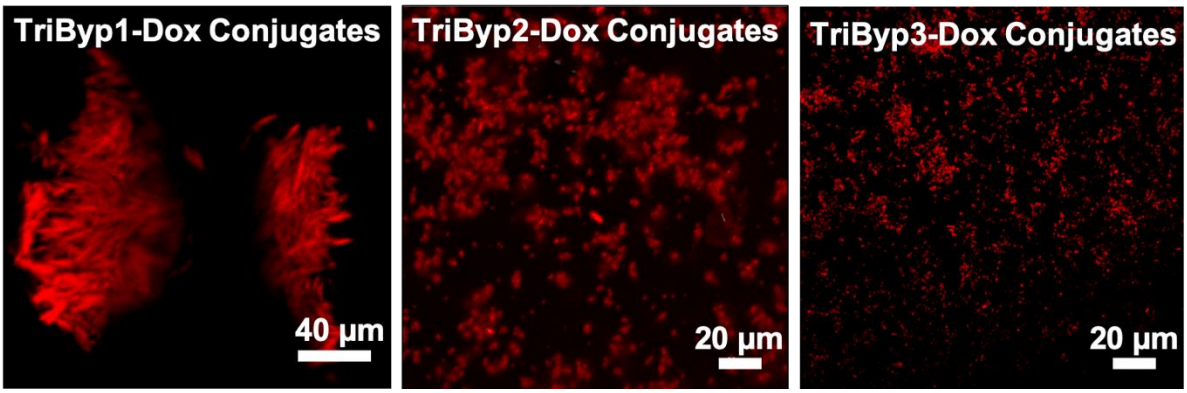

Figure 2.12 Confocal light microscopy images of **TriByp1**-DOX, **TriByp2**-DOX and **TriByp3**-DOX structures assembled in 10 mM MOPS buffer at pH 7.0.

To determine the binding efficiencies, the fluorescent assemblies were acidified and the amount of bound DOX was quantified using UPLC-MS. For the above mentioned concentrations of peptide and DOX, **TriByp2** displayed the highest binding efficiency (Table 2.2). It is also worth noting that the **TriByp2** assemblies possess nanoscale dimensions. Thus, **TriByp2** assemblies not only possess a higher docking efficiency, but also a more optimal size for cell uptake. For this reason, only the **TriByp2**-DOX assemblies were utilized for further biological testing. The **TriByp2**-DOX composite nanostructures were measured to be stable in cell growth media (RPMI), containing 10% fetal bovine serum. DLS measurements revealed a consistent assembly size over a period of 18 hours (Figure 2.13). The level of DOX released from the composites in media after 20 hours, quantified using UPLC-MS, was measured to be 10 ± 2.5 % of the total bound drug.

Table 2.2 DOX binding efficiency of **TriByp1**, **TriByp2** and **TriByp3** assemblies (500 μM peptide) assembled in the presence of 1 mM DOX in 10 mM MOPS buffer for 24 hours.

	Docking Efficiency
TriByp1	10%
TriByp2	15%
TriByp3	4%

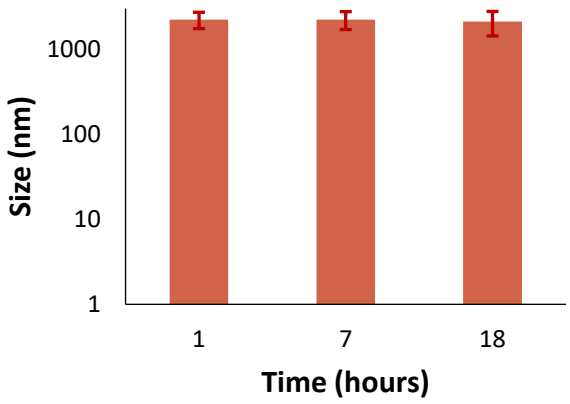

Figure 2.13 Size of **TriByp2**-DOX assemblies monitored over time in RPMI media containing 10% FBS.

2.2.9 pH-triggered Drug Release

Due to the fact that the coiled-coil assemblies are pH reversible, the release of DOX cargo could be triggered via a pH stimulus. The controlled release of DOX can allow for potential site-specific therapy, making the **TriByp2** assemblies possible viable tumor drug carriers. In addition, these carriers also have the potential to penetrate cells via endocytosis, allowing for late-endosomal release of the drug following their transition into more acidic cellular compartments.

With these factors in mind, the rate of release of DOX from the **TriByp2**-DOX assemblies was monitored over time at different pH values – 7.4, 6.5, 5.25, 4.5 and 4.0 (10 mM PBS), and the amount of DOX released was quantified using UPLC-MS (Figure 2.14). 100% of drug-release was achieved by acidification of the assemblies in glycine-HCl buffer (pH 3.0). As expected, the release rate of drug from the nanostructures is visibly faster at more acidic pH values. Almost 50% of the drug was released at pH 4.0 within the first 30 minutes, whereas less than 10% of the drug was released at pH 7.4 within the same time period. The half-life for release of doxorubicin decreased with the sequential lowering of pH to acidic values (Table 2.3). At low pH values of 4.0 and 4.5, the rate of release was observed to be extremely rapid with nearly 100% release within 24

hours. In contrast, at pH values of 6.5 and 7.4, less than 25% of the drug released after 72 hours. Though minimal levels of release were observed at early time points for the higher pH values, this can be attributed to loosely bound DOX molecules that are mostly located on the peripheral surface of the nanostructures. Collectively, these results suggest that it is possible to control the rate of release in response to environmental pH.

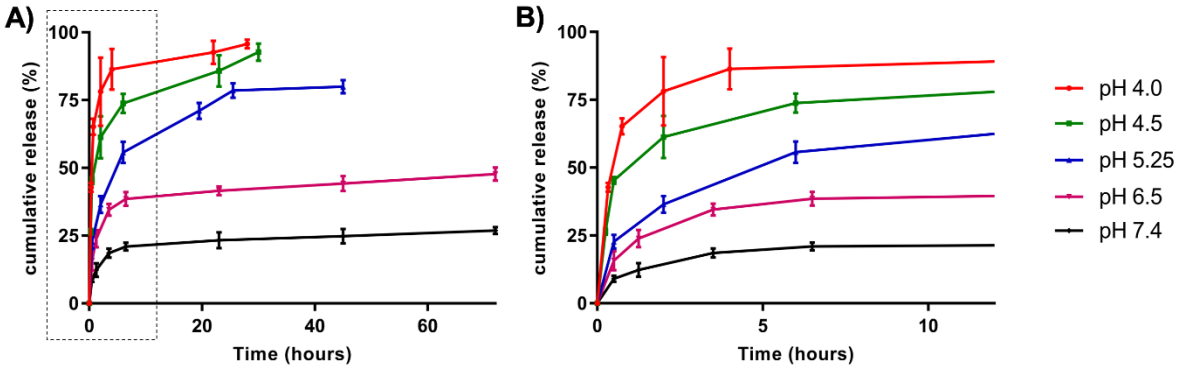

Figure 2.14 A) pH-dependent drug release profile of **TriByp2**-DOX nanostructures in PBS buffer (10 mM) at pH values of 4.0, 4.5, 5.25, 6.5 and 7.4, as a function of time. B) Zoom-in of selected area in A.

Table 2.3 Half-life release of DOX from **TriByp2**-DOX in PBS buffer (10mM) monitored at different pH values.

pH	4.0	4.5	5.25	6.5	7.4
Half-life release of Dox	30 min	1 hr	5 hrs	> 3 days	> 3 days

2.2.10 Cytotoxicity

In order for these nanostructures to be used as drug-delivery agents, acceptable mammalian cell viability is desired. Hence, we evaluated the viability of MCF-7 breast cancer cells with the **TriByp2** nanostructures, assembled at different concentrations of peptide, for 24 hours. The viable cells were quantified using an MTT assay.[38]

The materials show little to no toxicity even with nanostructure treatments containing peptide concentrations as high as 500 μM (Figure 2.15 A). We also investigated the cell viability of DOX, both in the free form as well as when docked to the nanostructures at 24 hours. As expected, there is decrease in viability with increasing DOX concentration in both cases (Figure 2.15 B-C). With the administration of free DOX, even at very low amounts (0.8 nmol), the cell viability dropped to below 75%. From these data, we obtained an IC_{50} value of 38.8 μg/ml for cells seeded at 15,000 cells/well, differing from the value reported in the literature (0.7 μg/ml).[39] However, taking into consideration the assay conditions from the latter, which applied a seeding density of 2000 cells/well and an assay time of 48 hours, the results obtained are reasonable. A similar trend was observed for the **TriByp2**-DOX materials, containing comparable levels of doxorubicin (Figure 2.15 C). However, the average cell viability for a given concentration of DOX was marginally higher in comparison to the free DOX data. This difference in viability may be attributed to a delayed release of drug from the nanostructures, thus, lowering the cytotoxicity within the given time period.

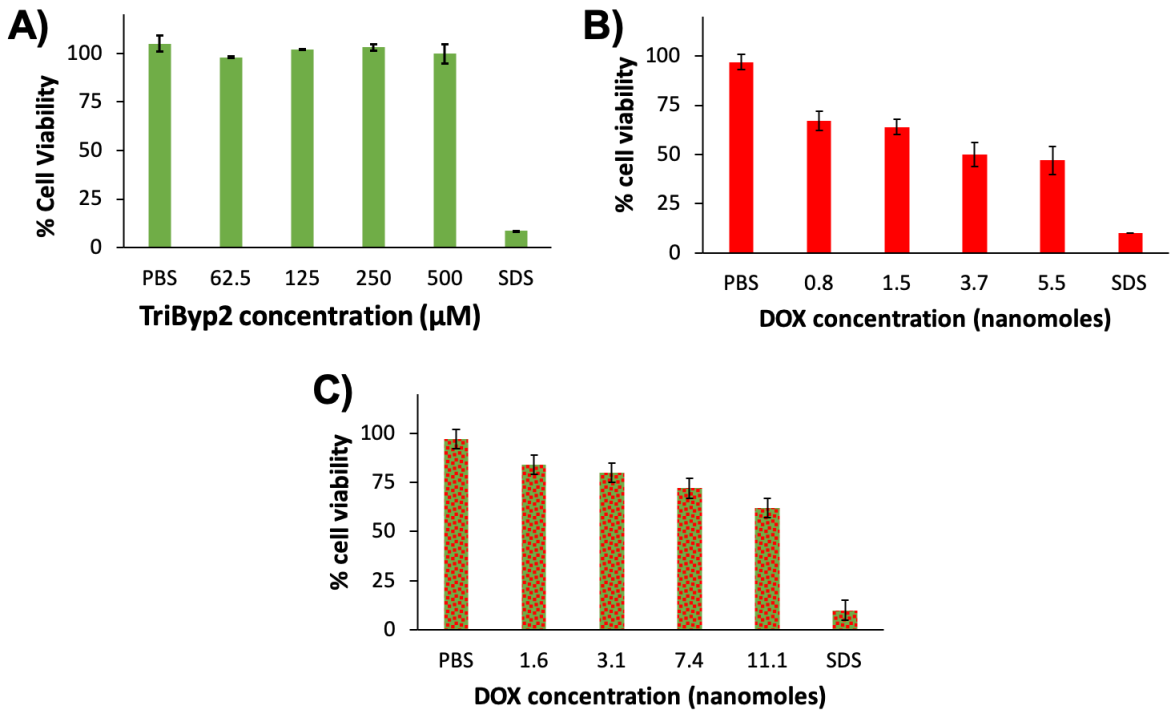

Figure 2.15 Cell viability of the MCF-7 cells, assessed via the MTT assay, with A) **TriByp2** nanostructures and, B) DOX, administered in its free form and C) DOX bound to the **TriByp2** nanostructures

2.2.11 Cell Uptake

The ability of these particles to penetrate cells and deliver doxorubicin was investigated using flow cytometry. After 1 hour incubation, the amount of drug internalized was quantified by measuring intracellular fluorescence. The cell uptake of doxorubicin was monitored in both its free and bound forms. As expected, with an increase in concentration of the treatment, there was a corresponding increase in accumulation of doxorubicin within the cells after 1 hour (Figure 2.16). A similar trend was observed for the **TriByp2**-DOX nanostructures, containing comparable amounts of drug. However, the measure of intracellular fluorescence was marginally higher for the latter. This potentially suggests that the uptake of doxorubicin is further enhanced when bound to the nanoparticles. However, it is critical to account for possible quenching of DOX upon intercalation with the DNA in the nucleus.[40, 41] Due to the stability of the **TriByp2**-DOX

composites in cell culture media, this potentially leads to the slower release rate of DOX from the nanostructures. Thus, a higher fluorescence signal is observed for the **TriByp2**-DOX particles, in contrast to the lower signal obtained as a result of a faster diffusion rate of the free DOX from the cytosol to the nucleus.

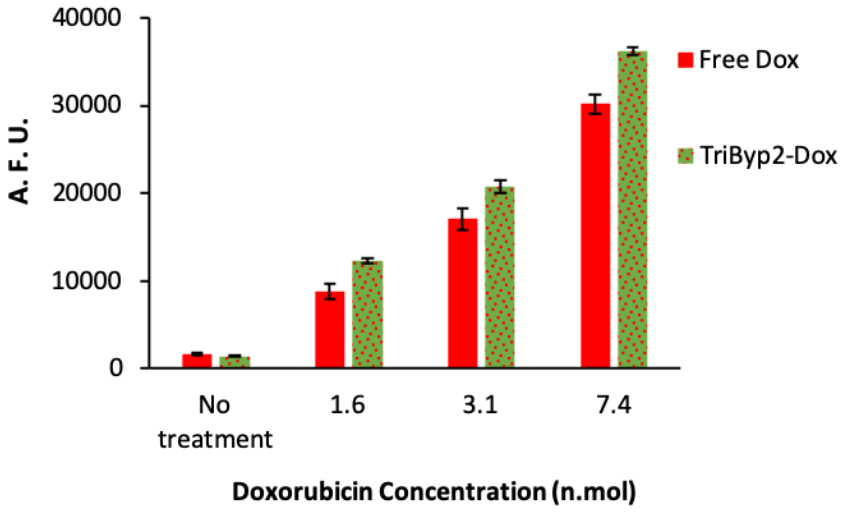

Figure 2.16 Accumulation of doxorubicin from **TriByp2** versus free DOX within MCF-7 cells as a function of doxorubicin concentration (t = 1 hour).

2.2.12 Interaction of the **TriByp2**-DOX particles with MCF-7 breast cancer cells

To gain further insight into localization of the nanostructures within the cells, we used confocal microscopy post-incubation with **TriByp2**-DOX materials, to study and elucidate their mode of delivery. Lysotracker (green) and Hoescht 33342 (blue) were used to label the endosomes and nuclei, respectively. Upon treatment of MCF-7 cells with free DOX (7.5 nmol) for 1 hour, the Hoechst dye showed colocalization with the doxorubicin fluorescence (blue + red = purple), thus confirming nuclear localization of the drug (Figure 2.17). The cells were also treated with the **TriByp2**-DOX particles (7.5 nmol) for 1 hour (Figure 2.18). The nanoparticles can be seen in and

around the periphery of the cells and there is doxorubicin diffusion into the nucleus, evidenced by co-localization.

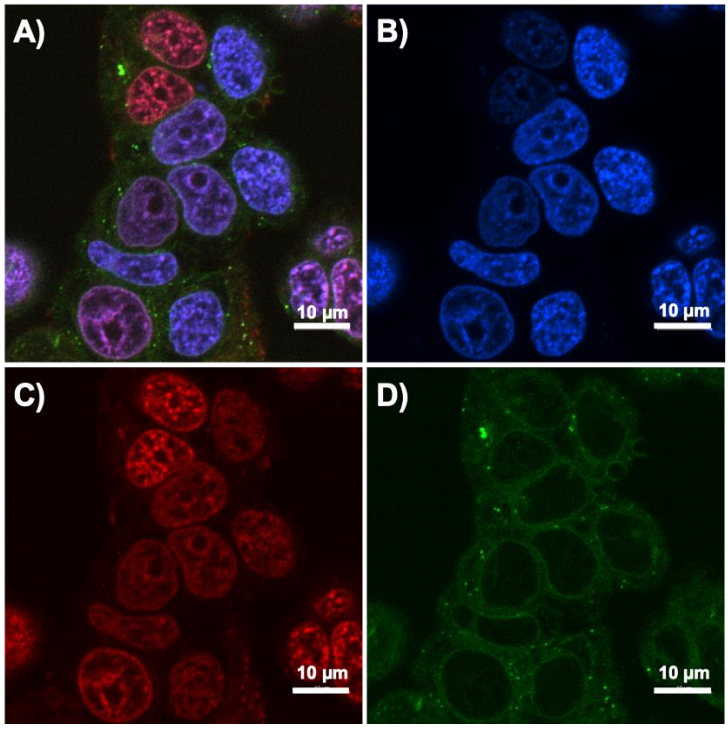

Figure 2.17 Confocal light microscopy images of MCF-7 cells treated with 7.5 nmol of DOX for 1 hour, depicting A) merged channels, B) blue channel, C) red channel and, D) green channel.

In order to determine the mechanism of delivery of these particles within the cells and elucidate whether endocytosis plays a role, their cell uptake was further investigated over time (Figure 2.18). Based on the fluorescence image (red channel, Figure 2.18), at the 4 hrs timepoint, there is a slight increase in DOX delivery to the nucleus. But after 8 hrs, there is a considerably greater amount of DOX delivery to the nucleus. There is, however, no evidence of co-localization between the DOX (Red) and Lysotracker (Green) for these data. Following this, we probed the effects of both longer times periods of incubation (8 hrs) as well as higher concentrations of bound DOX. At a higher concentration (13.1 nmoles DOX, Figure 2.19), there is some visible co-

localization with the endosomes (yellow = red + green) from the merged channel image. This potentially suggests that the **TriByp2**-DOX nanostructures can enter through a form of endocytosis.

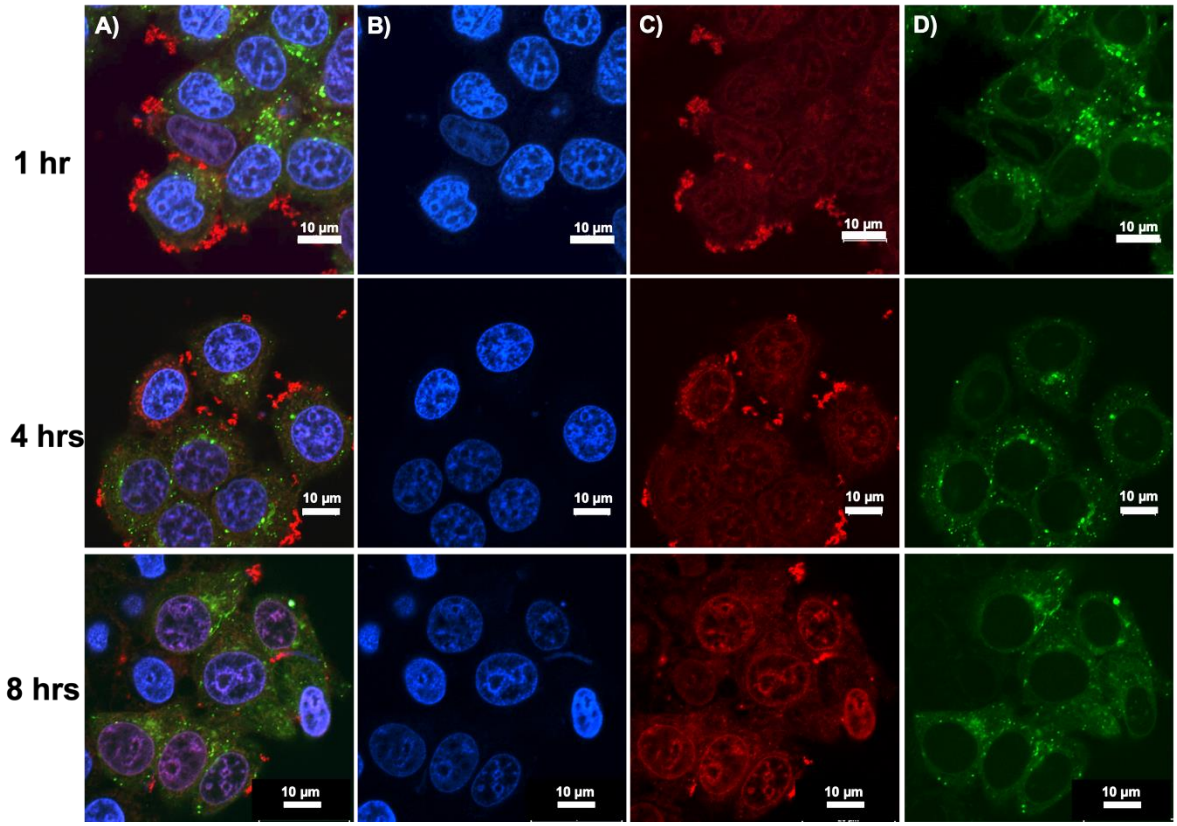

Figure 2.18 Confocal light microscopy images of MCF-7 cells, depicting their time-dependent interaction with **TriByp2**-DOX (7.5 n.moles of DOX).

The rate of endocytosis is highly dependent upon a variety of factors, including but not limited to temperature, shape, size and charge of cargo. The size of the **TriByp2** carriers (Table 2.1) has already been determined to be optimal for cellular entry. In addition, their bullet- or rod-like shape is a positive contributing factor towards their cell uptake.[42] In addition, surface charge plays a vital role in dictating cellular fate and to determine this we obtained zeta potential measurements. The surface charge of the **TriByp2** particles is positive (Table 2.4), however, after

DOX binding, the surface charge became essentially neutral (-10 to + 10 mV). It has been suggested that positively charged nanoparticles favour adhesion onto the slightly negative cell membrane, enabling cell uptake.[43, 44] This potentially explains the absence of their localization within the endosomes at low concentrations and short incubation times.

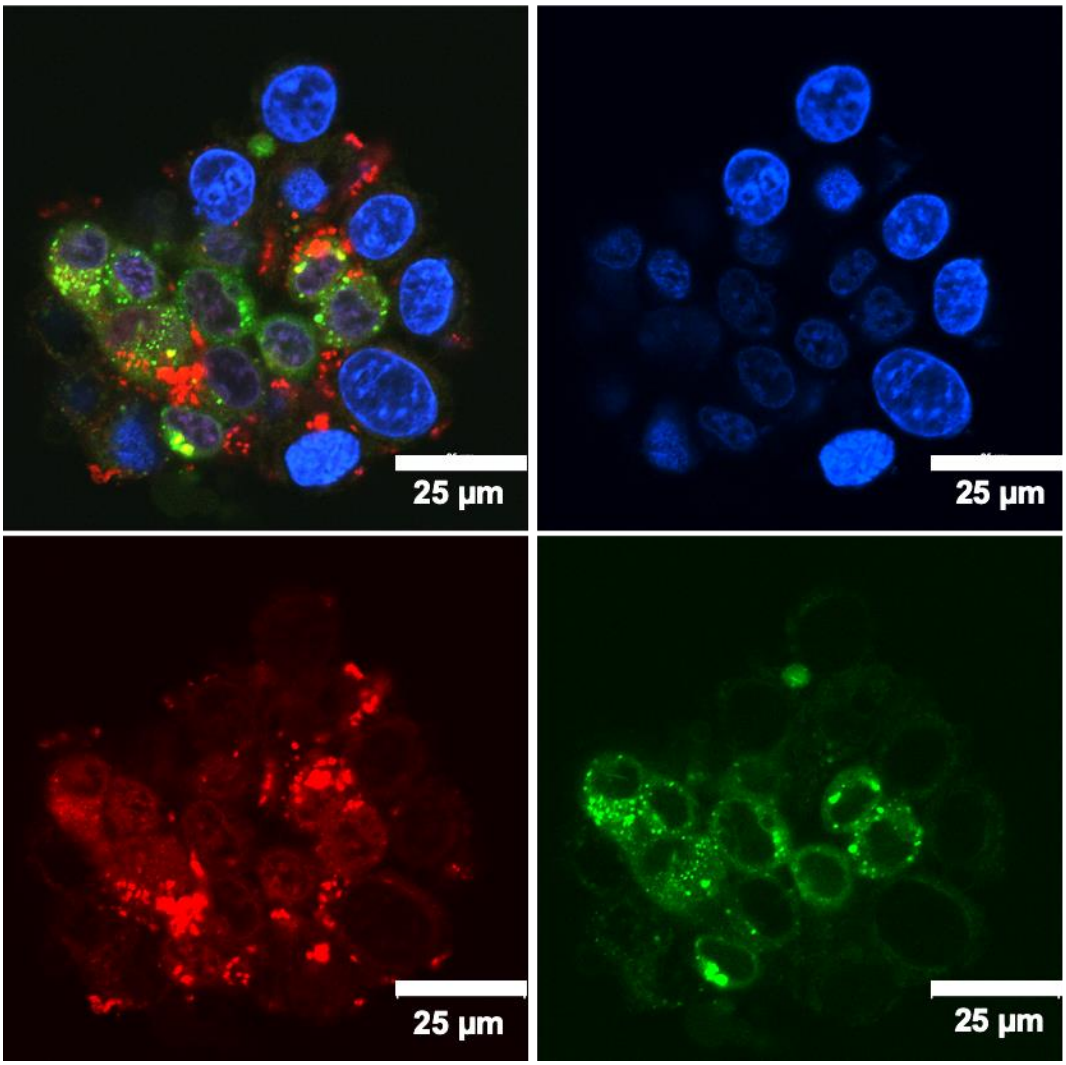

Figure 2.19 Confocal light microscopy images of MCF-7 cells incubated with **TriByp2**-DOX (13.1 nanomoles) for 8 hours, depicting A) merged channels, B) blue channel, C) red channel and, D) green channel.

Table 2.4 Zeta potential measurements of **TriByp2** with and without bound DOX.

	Zeta Potential (mV)
TriByp2	39.0
TriByp2-DOX	-3.2

2.3 Conclusion

In summary, coiled-coil trimers radially modified with bipyridine moieties successfully self-assembled into striated micro- and nanostructures in buffer at pH 7.0. Facile modification of the coiled-coil peptides with varied number of bipyridines at the three positions provided morphological control, as demonstrated by variation in shape from rectangular to square. This is evident from the higher propensity for lateral growth observed with an increase in the number of aromatic groups, leading to wider assemblies. Additionally, nanoscale banding was also observed that corresponds to the length of the coiled-coil trimers within each assembly. Interestingly, the formation of nano- to micro-structures was controlled both rapidly and reversibly as a function of pH over a number of cycles. In an attempt to demonstrate pH-controlled release of therapeutics at target cellular sites, we harnessed the electrostatic and aromatic interactions of the peptide material to non-covalently bind DOX to the **TriByp2** nanostructures. The nanostructures were found to be compatible with MCF-7 breast cancer cells, with close to 100% cell viability. The **TriByp2** nanostructures were also effective drug carriers. **TriByp2**-DOX composites displayed high stability in growth medium containing serum. successfully delivering the DOX into MCF-7 cells. Future studies will include experiments to elucidate the mechanism of nanostructure-cell interaction as well as to validate the specificity of pH-triggered release at tumor sites over healthy tissue.

2.4 Materials and Methods

2.4.1 Materials

Fmoc-protected amino acids Fmoc-Met, Fmoc-Lys(Boc), Fmoc-Lys(Mtt), Fmoc-Gln(Trt), Fmoc-Ile, Fmoc-Leu, Fmoc-Arf(Pbf), Fmoc-His, Fmoc-Glu(tBu), Fmoc-Tyr(tBu), Fmoc-Ala, Fmoc-Gly, Fmoc-Asp(tBu), and activation agent HBTU (O-benzotriazole-N,N,N',N'-tetramethyl-uronium-hexafluoro-phosphate) were purchased from ChemPep Inc (Wellington, Florda, USA). Diisopropylethylamine (DIEA) was purchased from ChemImpex, Inc (Wood Dale, IL, USA). ChemMatrix rink amide resin was purchased from PCAS Biomatrix Inc (Saint-Jean-sur-Richelieu, Quebec, Canada). Doxorubicin (DOX), Dichloromethane (DCM), N,N-dimethylformamide (DMF), methanol (MeOH), trifluoroacetic acid (TFA), triisopropylsilane (TIPS), diethyl ether, selenium(IV) oxide, silver(I) nitrate and 4, 4'-dimethylbipyridine were purchased from Sigma-Aldrich (St. Louis, MO). Acetic anhydride was purchased from Macron Fine Chemicals.

2.4.2 General Peptide Synthesis

All peptides were synthesized using standard Fmoc (9-fluoromethylmethoxycarbonyl) protected amino acids on Chemmatrix® Rink Amide resin (500 mg, 0.24 mmol/g). The desired amino acid was coupled to the free amine using HBTU (6 eq, 0.72 mmol) and DIEA (12 eq, 1.44 mmol) as coupling reagents dissolved in DMF. The mixture was added to the reaction flask containing the solid support (resin) and this was allowed to agitate for 3 hours at room temperature. After couplings, the solution was drained and the resin was washed with DMF (2 X 10 mL), DCM (2 X 10 mL), MeOH (2 X10 mL), DCM (2 X 10 mL), and DMF (2 X 10 mL). To remove the Fmoc protecting group, the resin-bound peptide was treated with piperidine (25% in DMF, 15 mL) and reacted for 30 minutes. The piperidine solution was drained and the resin was subsequently washed with DMF, DCM, MeOH, DCM, and DMF (3 x 10 mL each). The coupling and Fmoc

deprotection was monitored with the Kaiser (detection of 1° amines) test. This process was repeated until the full-length peptide was synthesized. After the final Fmoc deprotection, the N-terminal amino acid was acetylated using 5% acetic anhydride and 8.5% DIEA in DMF (v/v) for 30 minutes.

The Mtt protecting group was removed by treating the resin-bound resin peptide with 1.8% TFA in DCM (10 x 10 mL) with deprotection times of 3 minutes and DCM washes (10 mL) in between each treatment. This was followed by the coupling of 4'–methyl-2,2'bipyridine-4-carboxylic acid, synthesized using a reported procedure,[45,46] to the deprotected lysines using HBTU (6 eq, 0.57 mmol) and DIEA (12 eq, 1.14 mmol), dissolved in DMF. The resin was finally washed with DMF, DCM, MeOH, DCM, and DMF (2 X 10 mL each).

The resin bound peptides were then dried under reduced pressure. All peptides were cleaved from resin by treatment with TFA/TIPS/H_2O (95:2.5:2.5) (15 mL) (v/v) for 2 hours. The TFA cocktail was drained into a falcon tube. The resin was washed twice with TFA (30 mL) and twice with DCM (30 mL). These filtrates were combined and the solvents were removed under reduced pressure. The peptide was precipitated with cold diethyl ether (50 mL). The precipitate was collected via centrifugation. The supernatant was decanted, and to this was added fresh diethyl ether (50 mL). This was centrifuged once more and again the supernatant was decanted. The pellet was initially dried under flow of nitrogen, followed by drying under pressure. After determination of the mass, peptides were suspended in water (10 mg/mL).

The peptides were then purified by reverse phase (RP) HPLC on a Luna C18 (250 x 21.20 mm, 100 Å pore size, 10 micron, Phenomenex) column. Eluent conditions consisted of solvent A (CH_3CN/0.1% TFA) and solvent B (H_2O/0.1% TFA) with a 60-minute gradient (Table 2.5), and a

flow rate of 12 mL/min monitored at wavelengths of 214 nm and 254 nm (Appendix: A-1, A-2 and A-3). These peptides were subsequently characterized using MALDI-TOF (Table 2.6).

Table 2.5 HPLC purification conditions for coiled-coil peptides

	HPLC Conditions	**Retention Times**
TriByp3	20-90%	28.8 min
TriByp2	20-80%	32 min
TriByp1	20-90%	28.6

Table 2.6 MALDI-TOF characterized masses of coiled-coil peptides

	MW, calculated	**MALDI-MS, observed**
TriByp3	4423.35	4421.41
TriByp2	4214	4211
TriByp1	4003	4000.38

2.4.3 Circular Dichroism

CD analyses was performed using a JASCO J-810 CD spectropolarimeter (Jasco inc., Easton, MD), equipped with a PFD-425S Peltier temperature control unit. Samples were either suspended in 10 mM citrate buffer. The spectra were obtained at 4 ^{o}C, obtaining an average of 3 scans for each sample between 190-260 nm at 0.1 nm data pitch with a 1 nm bandwidth. The scan rate was 100 nm/min with a 1 second response time.

2.4.4 Analytical Ultracentrifugation (AUC)

The sedimentation velocity (SV) experiments were carried out in an Optima ProteomeLab XL-A analytical ultracentrifuge (Beckman Coulter). The peptide (400 µL, 100 µM) in Glycine-HCl buffer (pH 3.0) and the same volume of Glycine-HCl buffer (pH 3.0) as a blank reference

were loaded into a double sector AUC sample cell, assembled with a 12-mm epon-charcoal centerpiece and sapphire windows. The sample cells were placed in an An-60 Ti rotor. After equilibrating at 20 °C in the rotor chamber for 2 hours, the sample cells were centrifuged at 60,000 rpm at 20 °C and monitored by UV absorbance at 254 nm. The sedimentation velocity boundaries were analyzed by the c(s) model in SEDFIT version 15.01b and c(s) plots were created with GUSSI version 1.1.0.

2.4.5 Assembly of Banded Micro- and Nanostructures

A solution of the peptide (250 μM) in MOPS buffer (10 mM, pH 7.0) was incubated at room temperature for 48 hours, during which a colorless precipitate formed. This precipitate was washed by centrifuging the sample at 10 g for 3 minutes, followed by the removal of the supernatant and addition of water. This process was repeated two more times for each sample, with the final suspension being in water.

2.4.6 Transmission Electron Microscopy & Energy Dispersive X-ray Spectroscopy

Samples were imaged using a Tecnai T20 TEM (FEI Company, Hillsboro, OR, USA) operated at 100 KV, with a spot size of 3, 200μm condenser aperture and 70 μm objective aperture. Images were captured using an SIA L3C 4- megapixel CCD camera (Scientific Instruments and Application, Duluth, GA). Samples were fixed on a 400-mesh copper grid coated in formvar with a carbon film (Ted Pella, Redding, CA, USA) which were previously glow discharged. An aliquot of the assembly in water (3.5 μL) was placed directly onto the surface of the grid. This was left to stand for 2 minutes; the water was then wicked away. The grid was rinsed through stain droplets and blotted dry. Staining was done with 2% uranyl acetate. For EDX measurements, the sample was analyzed using an EDS detector for analyzing backscattered electrons.

2.4.7 Atomic Force Microscopy

A 5 µL aliquot of the rinsed sample post assembly, was placed on freshly cleaved Mica surface (Ted Pella, INC). This was left to air dry. Samples were imaged in air in tapping mode on the Asylum Cypher ES Microscope using silicon probes having a resonance frequency of 265-400 kHz (Ted Pella, INC – Tap300-G-10). All AFM images were obtained at 25 °C (room temperature).

2.4.8 Scanning Electron Microscopy

Samples were prepared by placing a 5 µL aliquot of the assembly in water, on the surface of a glass cover slip adhered to the specimen stub with double sided copper tape. The samples were left to air dry prior to being coated with platinum for 60 seconds using a sputter coater. Samples were imaged using a FEI NOVA NANO SEM field emission scanning electron microscope using the Everhart-Thornley (ETD) or the high-resolution through the lens (TLD) detectors. Samples were imaged at an accelerating voltage of 5 kV with optimal working distances between 3-5 mm and a 30 µm aperture.

2.4.9 Dynamic Light Scattering

DLS measurements were performed on a Zetasizer Nano ZS (Malvern Instruments Ltd, Worcestershire, UK). The peptides (250 µM) were suspended in 10 mM MOPS buffer (pH 7.0) and 10mM glycine-HCl buffer (pH 3.0). The solutions were measured in plastic cuvettes and were placed in a sample holder at 22 °C. The volume size distributions were obtained from analysis of correlation functions using the multiple spherical modes algorithm.

2.4.10 X-ray Scattering (WAXS & MAXS)

For X-ray scattering, samples were prepared by drop-casting an aliquot of the assembly in water on a Kapton film and the measurements were performed using a Ganesha SAXS-LAB

(Northampton, Massachusetts) system operated at near-vacuum conditions with a Cu Kα line (1.54 Å). Patterns were acquired with an acquisition time of 45 mins by means of a Pilatus detector with 487 × 619 pixels of 172 μm × 172 μm, placed at approximately 480 mm (MAXS) and 180 mm (WAXS), from the sample surface.

2.4.11 Assembly of DOX-infused Fluorescent Assemblies

A solution of the peptide (250 μM) in MOPS buffer (10 mM, pH 7.0) was incubated at room temperature in the presence of DOX (500 μM), during which a reddish-pink precipitate formed (total sample volume of 100 μL). This precipitate was washed by centrifuging the sample at 10 g for 3 minutes, followed by the removal of the supernatant (85 μL) and addition of PBS (85 μL). This process was repeated two more times for each sample, with the final suspension being in PBS (maintaining the total volume of 100 μL).

2.4.12 pH-triggered Release of DOX

Five sample solutions of the **TriByp2**-DOX composites suspended in PBS (100 μL, described above) were centrifuged, the supernatant (85 μL) was removed and the precipitate was resuspended in the appropriate pH buffers (85 μL of PBS – 7.4, 6.5, 5.25, 4.5, 4.0). For each of the five pH conditions, the release of DOX was monitored by analyzing the supernatant of the re-suspended assembly over time. At each time point, 85 μL of the supernatant was removed from each sample and replenished with its corresponding PBS buffer. The removed supernatant (85 μL) was mixed with glycine-HCl buffer (10 mM, 15 μL) and the concentration of DOX present was quantified using UPLC.

2.4.13 Media Stability

A solution of the **TriByp2**-DOX composites suspended in PBS (100 μL) were centrifuged, supernatant (85 μL) removed and resuspended in 100 μL of cell culture media (RPMI with 10% FBS). At different time points (1 hr, 7 hrs & 18 hrs), the sample size was monitored using DLS. After 20 hrs, the sample was centrifuged, following which 85 μL of the supernatant was diluted with 85 μL of cold acetonitrile. This mixture was again centrifuged to precipitate proteins from the media and the concentration of DOX in this final supernatant was analyzed using UPLC.

2.4.14 Cell Culture

MCF-7 breast cancer cells were grown in RPMI (Rosewell Park Memorial Institute) medium, supplemented with 10% fetal bovine serum (FBS), 1% L-glutamine and 1% penicillin-streptomycin and maintained at 37ºC under a controlled humidified atmosphere containing 5% CO_2. RPMI supplemented with 10% fetal bovine serum (FBS), 1% L-glutamine and 1% penicillin-streptomycin was also used for all cell assays.

2.4.15 Cell Toxicity

The viability of the MCF-7 cells with the **TriByp2** nanostructures (assembled from different concentrations of peptide – 62.5 μM, 125 μM, 250 μM and 500 μM) were analyzed via a colorimetric 3-(4,5- dimethyl-2-thiazolyl)-2,5-diphenyl-2H-tetrazolium bromide (MTT) (Sigma M2128) assay. The assemblies were prepared in 10 mM MOPS buffer (100 μL), washed using the centrifugation method (replenishing the removed supernatant with PBS buffer, pH 7.0) and resuspended in 50 μL of cell culture media. MCF-7 cells (15,000) cultured at 37 ºC and under 5% CO_2 were seeded to a 96-well plate and allowed to grow for 18 h. The spent media was aspirated and the macrophages were then treated with the assembled nanostructures (in 50 μL media) for 24 h at 37 ºC. 5% SDS and PBS were used as the positive and negative controls, respectively. After

incubation, the treatment was removed and 100 µL of fresh RPMI media was added to each well. Further, 10 µL of 12 mM 3-(4,5- dimethylthiazol-2-yl)-2,5-diphenyltetrazolium bromide (MTT) was added to each well and allowed to incubate for 2 h at 37 °C under 5% CO_2. Finally, the MTT solution was discarded and 100 µL of dimethyl sulfoxide (DMSO) was added to each well. The plate was allowed to shake for 15 min at room temperature and the absorbance of each well was measured at 590 nm using a microplate reader (TECAN SpectraFluor Plus). The results were expressed as the percentage of viable cells as compared to control with no treatment. Data were obtained in duplicates from at least two independent experiments.

The MTT assay was also used to compare the viability of the MCF-7 cells with DOX, in its free form and as bound to **TriByp2** nanostructures. For the **TriByp2**-DOX composites, the amount of DOX administered was controlled by incubating 250 µM of DOX with different peptide concentrations (in 10 mM MOPS buffer), 50 µM, 100 µM, 250 µM and 500 µM each, to achieve a loading of 1.6 nmol, 3.1 nmol, 7.4 nmol and 13.1 nmol of DOX, respectively. The **TriByp2**-DOX composites were washed and administered using the same assay conditions as outlined above. For the MTT assay with the free DOX, comparable concentrations (nmol) of DOX were administered.

2.4.16 Cell Uptake

MCF-7 cells were cultured as described above and seeded at 125,000 cells collected in round bottom tubes (BD Falcon). Next 1000 µL of FBS supplemented RPMI containing the **TriByp2**-Dox and free DOX at the desired concentrations were added to the tubes and incubated for 1 h at 37 °C. Cells treated with media only, served as a control for the experiment. After incubation, the cells were centrifuged at 1500 rpm, the media was aspirated, and the cells were re-suspended in

400 µL PBS. Samples were analyzed using the BD Accuri™ C6 Flow cytometer (FL2-A channel). Data was obtained in duplicates from at least two independent experiments.

2.4.17 Confocal Cell Experiments

MCF-7 cells were seeded at a density of 200,000 cells/well in a 4-well LabtTek chambered slides (Thermo Fisher Scientific 155383) and allowed to grow for 18 h at 37 °C under 5% CO_2. The media was aspirated, and the cells were washed 1X with 400 µL PBS. Next the **TriByp2**-Dox nanostructures at chosen concentrations was added to each well in 400 µL of DMEM media supplemented with FBS. The cells were allowed to incubate with peptide for 1, 4 and 8hrs at 37 °C under 5% CO_2. Excess media was aspirated, and the cells were washed 1X with 400 µL PBS. The cells were further treated with either Lysotracker (600 nM, green) (Invitrogen L7528) and Hoescht 3342 (1 nM, blue) for 30 min at 37 °C. The excess dye was aspirated, the cells were washed with PBS (400 µL) and fresh RPMI media (400 µL) was added to each well. Imaging was performed using a Nikon A1R multiphoton inverted confocal microscope under 60X oil objective.

2.5 References

1. Haines, L. A.; Rajagopal, K.; Ozbas, B.; Salick, D. A.; Pochan, D. J.; Schneider, J. P. Light-Activated Hydrogel Formation Via the Triggered Folding and Self-Assembly of a Designed Peptide. *J. Am. Chem. Soc.* **2005,** *127* (48), 17025-17029.

2. Li, X.; Gao, Y.; Kuang, Y.; Xu, B. Enzymatic Formation of a Photoresponsive Supramolecular Hydrogel. *Chem. Comm.* **2010,** *46* (29), 5364-5366.

3. Yao, M.-H.; Yang, J.; Du, M.-S.; Song, J.-T.; Yu, Y.; Chen, W.; Zhao, Y.-D.; Liu, B. Polypeptide-Engineered Physical Hydrogels Designed from the Coiled-Coil Region of Cartilage Oligomeric Matrix Protein for Three-Dimensional Cell Culture. *J. Mater. Chem. B* **2014,** *2* (20), 3123-3132.

4. Ulijn, R. V.; Smith, A. M. Designing Peptide Based Nanomaterials. *Chem. Soc. Rev.* **2008,** *37*, 664-675.

5. Zimenkov, Y.; Dublin, S. N.; Ni, R.; Tu, R. S.; Breedveld, V.; Apkarian, R. P.; Conticello, V. P. Rational Design of a Reversible pH-Responsive Switch for Peptide Self-Assembly. *J. Am. Chem. Soc.* **2006,** *128*, 6770-6771.

6. Aggeli, A.; Bell, M.; Carrick, L. M.; Fishwick, C. W. G.; Harding, R.; Mawer, P. J.; Radford, S. E.; Strong, A. E.; Boden, N. Ph as a Trigger of Peptide Beta-Sheet Self-Assembly and Reversible Switching between Nematic and Isotropic Phases. *J. Am. Chem. Soc.* **2003,** *125*, 9619-9628.

7. Fletcher, N. L.; Lockett, C. V.; Dexter, A. F. A pH-Responsive Coiled-Coil Peptide Hydrogel. *Soft Matter* **2011,** *7* (21), 10210-10218.

8. Schneider, J. P.; Pochan, D. J.; Ozbas, B.; Rajagopal, K.; Pakstis, L.; Kretsinger, J. Responsive Hydrogels from the Intramolecular Folding and Self-Assembly of a Designed Peptide. *J. Am. Chem. Soc.* **2002,** *124* (50), 15030-15037.

9. De Leon-Rodriguez, L. M.; Hemar, Y.; Mo, G.; Mitra, A. K.; Cornish, J.; Brimble, M. A. Multifunctional Thermoresponsive Designer Peptide Hydrogels. *Acta Biomater*. **2017,** *47*, 40-49.

10. Huang, R.; Wang, Y.; Qi, W.; Su, R.; He, Z. Temperature-Induced Reversible Self-Assembly of Diphenylalanine Peptide and the Structural Transition from Organogel to Crystalline Nanowires. *Nanoscale Res. Lett.* **2014,** *9* (1), 1-9.

11. Luo, T.; He, L.; Theato, P.; Kiick, K. L. Thermoresponsive Self-Assembly of Nanostructures from a Collagen-Like Peptide-Containing Diblock Copolymer. *Macromol. Biosci.* **2015,** *15* (1), 111-123.

12. Luo, T.; Kiick, K. L. Noncovalent Modulation of the Inverse Temperature Transition and Self-Assembly of Elastin-B-Collagen-Like Peptide Bioconjugates. *J. Am. Chem. Soc.* **2015,** *137* (49), 15362-15265.

13. Lv, S.; Cao, Y.; Li, H. Tandem Modular Protein-Based Hydrogels Constructed Using a Novel Two-Component Approach. *Langmuir* **2012,** *28* (4), 2269-2274.

14. Ozbas, B.; Rajagopal, K.; Haines-Butterick, L.; Schneider, J. P.; Pochan, D. J. Reversible Stiffening Transition in β-Hairpin Hydrogels Induced by Ion Complexation. *J. Phys. Chem. B* **2007,** *111* (50), 13901-13908.

15. Petka, W.; Harden, J.; McGrath, K.; Wirtz, D.; Tirrell, D. Reversible Hydrogels from Self-Assembling Artificial Proteins. *Science* **1998,** *281* (5375), 389-392.

16. Pochan, D. J.; Schneider, J. P.; Kretsinger, J.; Ozbas, B.; Rajagopal, K.; Haines, L. Thermally Reversible Hydrogels Via Intramolecular Folding and Consequent Self-Assembly of a De Novo Designed Peptide. *J. Am. Chem. Soc.* **2003,** *125* (39), 11802-11803.

17. Wright, E. R.; Conticello, V. P. Self-Assembly of Block Copolymers Derived from Elastin-Mimetic Polypeptide Sequences. *Adv. Drug Deliv. Rev.* **2002,** *54* (8), 1057-1073.

18. Gleaton, J.; Chmielewski, J. Thermally Controlled Collagen Peptide Cages for Biopolymer Delivery. *ACS Biomater. Sci. & Eng.* **2015,** *1* (10), 1002-1008.

19. Toledano, S.; Williams, R. J.; Jayawarna, V.; Ulijn, R. V. Enzyme-Triggered Self-Assembly of Peptide Hydrogels Via Reserved Hydrolysis. *J. Am. Chem. Soc.* **2006,** *128* (4), 1070-1071.

20. Yang, Z. M.; Liang, G. L.; Wang, L.; Xu, B. Using a Kinase/Phosphatase Switch to Regulate a Supramolecular Hydrogel and Forming the Supramoleclar Hydrogel in Vivo. *J. Am. Chem. Soc.* **2006,** *128* (9), 3038-3043.

21. Gao, W.; Chan, J.; Farokhzad, O. C. pH-Responsive Nanoparticles for Drug Delivery. *Mol. Pharm.* **2010,** *7* (6), 1913-1920.

22. Kato, Y.; Ozawa, S.; Miyamoto, C.; Maehata, Y.; Suzuki, A.; Maeda, T.; Baba, Y. Acidic Extracellular Microenvironment and Cancer. *Cancer Cell Int.* **2013,** *13*(89), 1-8.

23. Swietach, P.; Vaughan-Jones, R. D.; Harris, A. L.; Hulikova, A. The Chemistry, Physiology and Pathology of pH in Cancer. *Philos. Trans. R. Soc. B-Biol. Sci.* **2014,** *369* (1638), 20130099-20130108.

24. Longer, M. A.; Ch' Ng, H. S.; Robinson, J. R. Bioadhesive Polymers as Platforms for Oral Controlled Drug Delivery Iii: Oral Delivery of Chlorothiazide Using a Bioadhesive Polymer. *J. Pharm. Sci.* **1985,** *74* (4), 406-411.

25. Grumezescu, A. M. Nanobiomaterials in Drug Delivery. In *Applications of Nanobiomaterials*; William Andrew: Amsterdam, Netherlands, 2016; Vol. 9.

26. Raj, R.; Saniya, A.; Ildiko, B. Polymeric Nanoparticles in Gene Therapy: New Avenues of Design and Optimization for Delivery Applications. *Polymers* **2019,** *11* (4), 745-780.

27. Harbury, P. B.; Kim, P. S.; Alber, T. Crystal Structure of an Isoleucine-Zipper Trimer. *Nature* **1994,** *371*, 80-83.

28. Harbury, P. B.; Zhang, T.; Kim, P. S.; Alber, T. A Switch between Two-, Three-, and Four-Stranded Coiled Coils in GCN4 Leucine Zipper Mutants. *Science* **1993,** *262* (5138), 1401-1407.

29. Aldridge, W. S.; Hornstein, B. J.; Serron, S.; Dattelbaum, D. M.; Schoonover, J. R.; Meyer, T. J. Synthesis and Characterization of Oligoproline Based Molecular Assemblies for Light Harvesting. *J. Org. Chem.* **2006,** *71* (14), 5186-5190.

30. Lau, S. Y. M.; Taneja, A. K.; Hodges, R. S. Synthesis of a Model Protein of Defined Secondary and Quaternary Structure. *J. Biol. Chem.* **1984,** *259*, 13253-13261.

31. Greenfield, N. Using Circular Dichroism Spectra to Estimate Protein Secondary Structure. *Nat. Protoc.* **2006,** *1* (6), 2876-2890.

32. Holzwarth, G.; Doty, P. The Ultraviolet Circular Dichroism of Polypeptides. *J. Am. Chem. Soc.* **1965,** *87* (2), 218-228.

33. O'Shea, E. K.; Rutkowski, R.; Kim, P. S. Evidence That the Leucine Zipper Is a Coiled Coil. *Science* **1989,** *243*, 538-542.

34. Ciani, B.; Bjelić, S.; Honnappa, S.; Jawhari, H.; Jaussi, R.; Payapilly, A.; Jowitt, T.; Steinmetz, M. O.; Kammerer, R. A. Molecular Basis of Coiled-Coil Oligomerization-State Specificity. *Proc. Nat. Acad. Sci. U. S. A.* **2010,** *107* (46), 19850-19855.

35. Nepal, M.; Sheedlo, M. J.; Das, C.; Chmielewski, J. Accessing Three-Dimensional Crystals with Incorporated Guests through Metal-Directed Coiled-Coil Peptide Assembly. *J. Am. Chem. Soc.* **2016,** *138* (34), 11051-11057.

36. Papapostolou, D.; Smith, A. M.; Atkins, E. D. T.; Oliver, S. J.; Ryadnov, M. G.; Serpell, L. C.; Woolfson, D. N. Engineering Nanoscale Order into a Designed Protein Fiber. *Proc. Nat. Acad. Sci. U. S. A.* **2007,** *104* (26), 10853-10858.

37. Mohan, P.; Rapoport, N. Doxorubicin as a Molecular Nanotheranostic Agent: Effect of Doxorubicin Encapsulation in Micelles or Nanoemulsions on the Ultrasound-Mediated Intracellular Delivery and Nuclear Trafficking. *Mol. Pharm.* **2010,** *7* (6), 1959-1973.

38. Riss, T. L.; Moravec, R. A.; Niles, A. L.; Benink, H. A.; Worzella, T. J., Cell Viability Assays. In *Assay Guidance Manual*, Sittampalam, G. S., Ed. Bethesda, MD Eli Lilly & Company and the National Center for Advancing Translational Sciences: Bethesda, MD, 2016; pp 1-31.

39. Fang, X. J.; Jiang, H.; Zhu, Y. Q.; Zhang, L. Y.; Fan, Q. H.; Tian, Y. Doxorubicin Induces Drug Resistance and Expression of the Novel Cd44st via Nf-κB in Human Breast Cancer MCF-7 Cells. *Oncol. Rep.* **2014,** *31* (6), 2735-2742.

40. Hajian, R.; Shams, N.; Mohagheghian, M. Study on the Interaction between Doxorubicin and Deoxyribonucleic Acid with the Use of Methylene Blue as a Probe. *J. Braz. Chem. Soc.* **2009,** *20* (8), 1399-1405.

41. Airoldi, M.; Barone, G.; Gennaro, G.; Giuliani, A. M.; Giustini, M. Interaction of Doxorubicin with Polynucleotides. A Spectroscopic Study. *Biochemistry* **2014,** *53*, 2197-2207.

42. Albanese, A.; Tang, P. S.; Chan, W. C. W. The Effect of Nanoparticle Size, Shape, and Surface Chemistry on Biological Systems. *Annu. Rev. Biomed. Eng.* **2012,** *14*, 1-16.

43. Thorek, D. L. J.; Tsourkas, A. Size, Charge and Concentration Dependent Uptake of Iron Oxide Particles by Non-Phagocytic Cells. *Biomaterials* **2008,** *29* (26), 3583-3590.

44. Slowing, I.; Trewyn, B.; Lin, V.-Y. Effect of Surface Functionalization of MCM-41-Type Mesoporous Silica Nanoparticles on the Endocytosis by Human Cancer Cells. *J. Am. Chem. Soc.* **2006,** *128* (46), 14792-14793.

45. Peek, B. M.; Ross, G. T.; Edwards, S. W.; Meyer, G. J.; Meyer, T. J. Synthesis of Redox Derivatives of Lysine and Related Peptides Containing Phenothiazine or Tris(2,2'-bipyridine)ruthenium(II). *Int. J. Peptide Protein Res.* **1991,** *38* (2), 114-123.

46. Aldridge, W. S. III; Hornstein, B. J.; Serron, S.; Dattelbaum, D. M.; Schoonover, J. R.; Meyer, T. J. Synthesis and Characterization of Oligoproline Based Molecular Assemblies for Light Harvesting. *J. Org.Chem.*. **2006,** *71* (14), 5186-5190.

CHAPTER 3. MULTI-TIERED SELF-ASSEMBLY OF COILED-COIL PEPTIDES INTO NANOTUBES & MICROBARRELS

3.1 Introduction

Molecular self-assembly of biologically-relevant motifs is a powerful tool to fabricate nano- and micro-assemblies for applications in nanotechnology and medicine.[1] Nature is a grandmaster in creating structurally complementary and chemically compatible constituents that arrange into self-organized functional systems. This phenomenon of self-assembly can be observed in aspects of protein folding, the cell-membrane and highly-evolved virus architectures, to name a few.[2] In order to mimic this bottom-up fabrication approach to obtain functional structures, it is crucial to identify tunable, pre-exisiting building-blocks. Peptides have gained considerable interest in this regard, and their structures have been widely used to achieve modular assembly of novel supramolecular architectures.[3-6] Supramolecular assembly consists of a synergistic ensemble of interactions, such as hydrogen bonding, van der Waals forces, electrostatic and π-π interactions, and metal chelation.[2] The hierarchical, and at times reversible nature of the growth of these individual building-blocks into three dimensional structures provides scope to investigate the mechanistic aspects of their assembly. As a result, multiple orders of assembly can be induced, with increasing levels of structural intricacy at each tier and across scales. Such knowledge of assembly delivers the potential to create complex structures programmed with sophisticated mechanical and biological functions. Herein we explore the mechanistic formation of two distinct architectures, namely nanotubes and microbarrels, as a result of altering the oligomerization of a coiled-coil motif.

3.2 Coiled-Coil Trimer: Nanotubes

Tubular structures with hollow cavities, as opposed to fibers or rod-like structures that have no inner space, have garnered considerable attention, particularly as drug carriers as they possess advantages over other drug-delivery systems.[7, 8] More specifically, hollow tubes which have different inner and outer surfaces, can be differentially functionalized to allow for site-specific cargo loading, thus enabling multifunctionality.[9] Carbon nanotubes have been the traditional choice of organic nanotubes based on their thermal and electric properties, as well as the ability to structurally fabricate them with a range of different diameters.[10-14] However, without further chemical modifcations, their biological applications are limited by their low solubility in biological conditions.[15, 16] Peptide building-blocks, on the other hand, can offer extensive chemical functionality in addition to enhancing biocompatibility and potential molecular recognition properties. Cyclic peptides have been used to form hollow cylinders, comprising ring-like peptide stacks assembled via hydrogen bonding.[17-21] In addition, the assembly of short peptide building-blocks into tubular structures has also been investigated. The most prominent examples utilize diphenylalanine(FF)-based moieties to create hollow tubular structures, self-assembled via π-π stacking and β-sheet structure formation.[22] These have been employed for use as scaffolds with antibacterial properties,[23] light-harvesting applications,[24] piezoelectric energy harvesters[25] and biosensing.[26] Their potential for drug-delivery applications as well as their ability to conjugate to drug molecules has also been explored.[27] Analogous to the FF motif, dileucine (LL) nanotubes have also been developed to exhibit piezoelectric properties.[28, 29]

Hollow tube assemblies from linear peptides with more elaborate secondary structures are lesser known. Coiled-coils have the tendency to form fibrillar structures[30-35] and their higher-order assembly into hollow tubes has remained a challenge. However, the flexibility of the coiled-coil

sequence and knowledge of their folding has allowed for rational engineering of assemblies.[36-40] Limited demonstrations thus far include the elegant design of six-[41] and seven-helix coiled-coil bundles[35] into multichannel nanotubes with inner pore diameters of 5-7 Å. More recently, the assembly of a designed coiled-coil homotetramer into hollow nanotubes with inner diameters of 13 nm has been described.[42] However, in these reports, the tubular cavities have not been harnessed as potential carriers of cargo. In the present study, we demonstrate the higher-order assembly of coiled-coil trimer peptides into hollow tubes and reveal their ability to selectively encapsulate cargo within their interior cavities.

3.2.1 Peptide Design and Synthesis

Our peptide sequence is modelled on the GCN4 leucine zipper with modifications, reported by Kim and co-workers.[43, 44] The dimerization domain of the GCN4 can be transformed to trimeric and tetrameric forms via mutations of the hydrophobic residues within the coiled-coil interior. More specifically, the substitution of isoleucine groups at the *a* and *d* positions within the hydrophobic core allows for an acute packing geometry of the beta-branched side-chains within the helical peptide, ultimately resulting in an oligomerization shift from the dimer to the trimer. The isoleucine zipper sequence, in particular, has been previously modified with metal binding ligands at the terminii and aromatic moieties along the backbone to generate hexagonal crystals[45] and banded rectangular microstructures,[46] respectively. We hypothesized that the unmodified coiled-coil trimer, **TriNL,** with its native polar residues highlighted in blue at the *b*, *c* and *f* positions of the helical wheel, would be capable of participating in inter-trimer electrostatic and hydrogen-bonding interactions to form higher-order structures **(**Figure 3.1**)**.

TriNL was synthesized using standard Fmoc-based solid-phase peptide synthesis on Chemmatrix H-rink amide resin, utilizing the O-(benzotriazol-1-yl)-N,N,N’,N’ -

tetramethyluronium hexafluorophosphate (HBTU) coupling agent. The peptide was cleaved from resin with a trifluoroacetic acid cocktail, purified to homogeneity using reverse phase-HPLC and characteried by MALDI-TOF mass spectrometry.

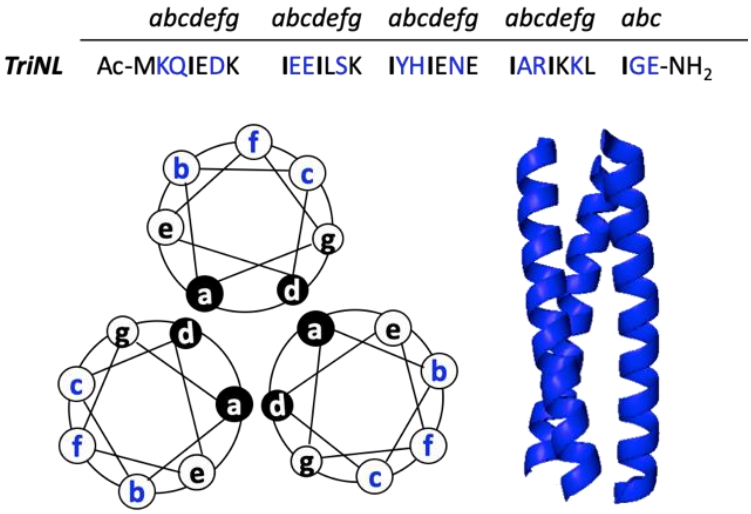

Figure 3.1 Peptide sequence of **TriNL** with a depiction of its helical wheel and trimeric coiled-coil.

3.2.2 Nanotube Assembly

To initiate assembly, the peptide (1 mM) was added to a buffered solution (10 mM MOPS, pH=7.4). After 30 minutes at room temperature, the peptide formed a dense precipitate which was visualized using SEM. **TriNL** was observed to form hollow tubes with lengths in the range of 5-12 μm and widths in the range of 0.75-1.50 μm, (Figure 3.2 & 3.3). The tube openings (100-950 nm) reveal a non-uniform thickness to the interiors with jagged edges (Figure 3.2 B-C). In addition, the outer surface of the tubes displays a pattern of longitudinal ridges along the axis of the tube (Figure 3.2 C-D). From these data, we observed the lateral association of thinner strips of material with one another to form a hollow tube. Tapping-mode atomic force microscopy (AFM) images of **TriNL** assembled in MOPS buffer revealed a height range of 350-900 nm, which is reasonably

well within the experimental range determined from the scanning electron microscopy (SEM) micrographs. In addition, the 3D height view also depicts the expected curved topology associated with tubular structures (Figure 3.3).

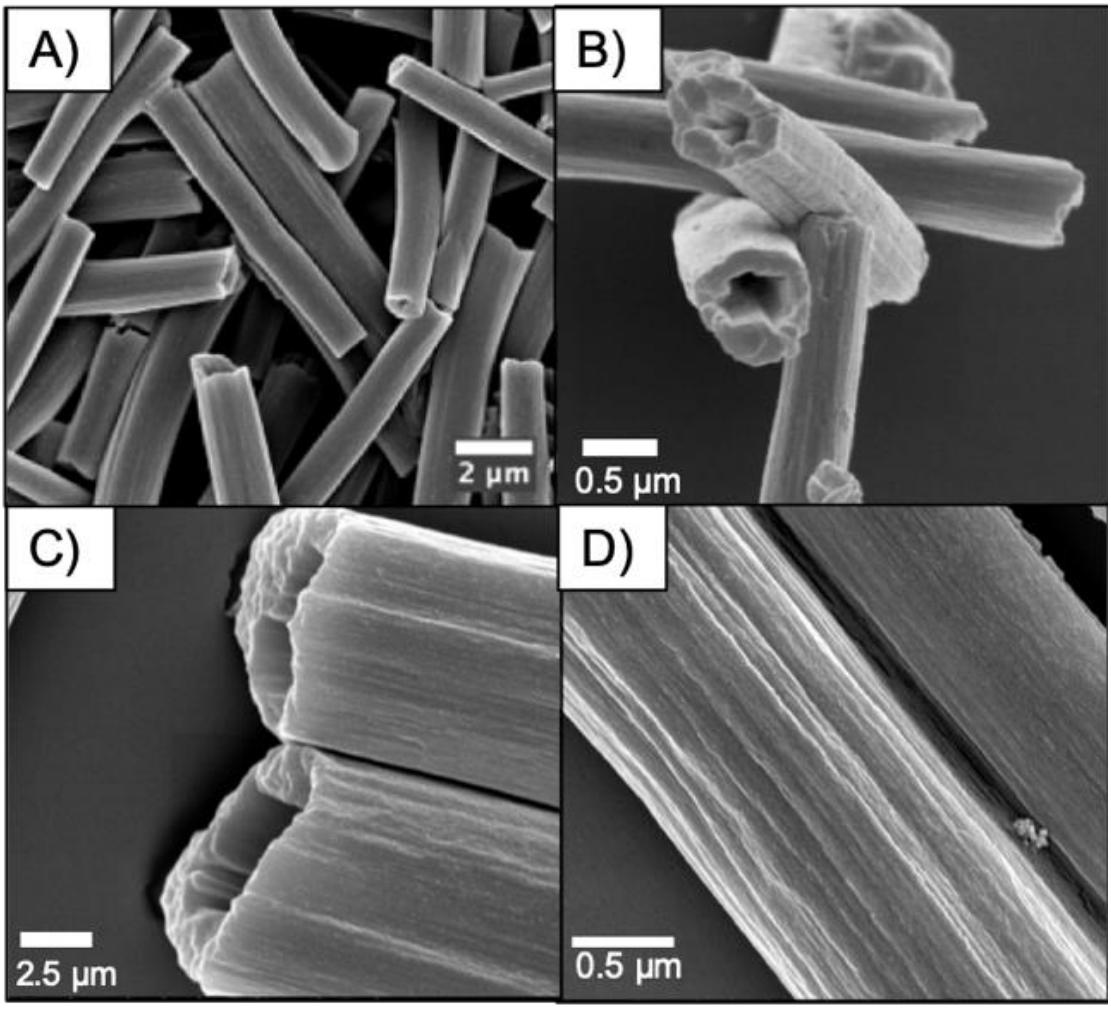

Figure 3.2 SEM micrographs (A-D) of hollow tubes formed from 1 mM **TriNL** in 10 mM MOPS buffer, pH 7.0 (30 min).

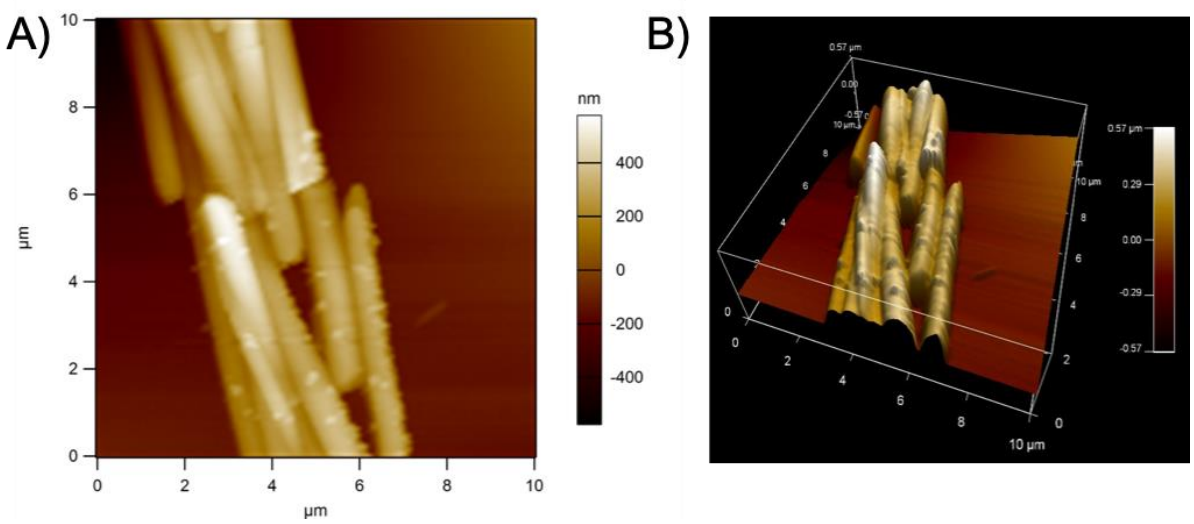

Figure 3.3 Tapping-mode AFM images (Height-A) and (3D view of Height-B) of 1 mM **TriNL** tubes in 10 mM MOPS buffer.

It is also worth noting that when incubated for longer time periods (> 12 hours), the peptide assembly results in the formation of solid tubes. SEM micrographs suggest that the hollow tubes are filled-in with additional trimer material, transforming from a hollow tube to a solid rod (Figure 3.4). This sustained inward-growth of the tube possibly indicates that the hollow tube serves as a structural precursor towards its morphological transformation into a rod.

The native GCN4 coiled-coil dimer (DiNL) was also investigated for higher-order assembly under similar assembly conditions. The assembly mixture in this case did not yield a visible precipitate even after extended incubation times up to 24 hours. Centrifugation of the sample followed by visualization via transmission electron microscopy (TEM) demonstrated amorphous aggregates of peptide material with no definite order (Figure 3.5). The increase in oligomerization from the dimeric to trimeric form evidently provides greater scope for interfacial interactions between the coiled-coil units, leading to more well-defined structures.

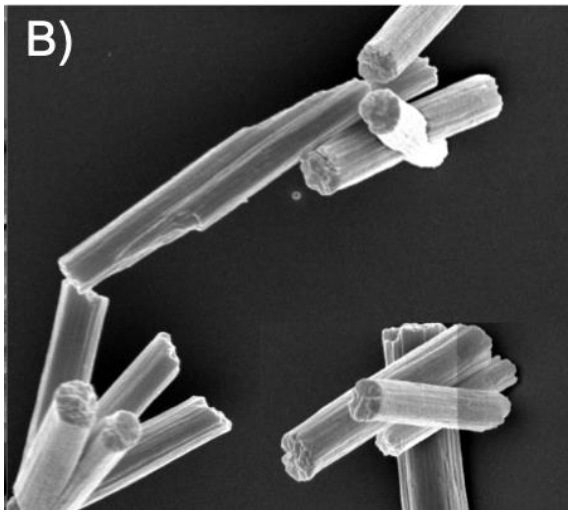

Figure 3.4 SEM micrograph of 1 mM **TriNL** assembled in 10 mM MOPS (pH 7.0) buffer at longer time periods (12 hours).

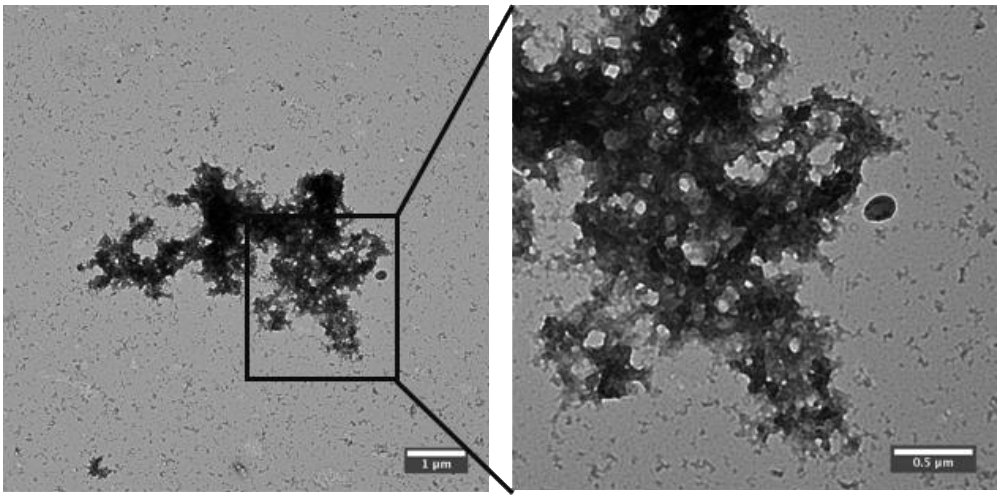

Figure 3.5 TEM micrographs of 1mM **DiNL** in 10 mM MOPS buffer (pH 7.0, 4 hours).

3.2.3 Structure Elucidation

TEM was used to further probe the coiled-coil trimer packing within the tubular assemblies of **TriNL**. TEM analysis revealed a banding pattern along the surface, perpendicular to the tube axis (Figure 3.6 A). Fourier transform of these TEM images (Figure 3.6 B) revealed that the banding pattern on the surface of the tube corresponds to a spacing of 4.4 nm, which corresponds to the length of the coiled-coil trimer of TriNL. A second order spacing was also visible, which is

also associated with the helical repeat along the axis. This suggests that within each assembly, the coiled-coils align themselves along the axis of the tube, perpendicular to the direction of banding.

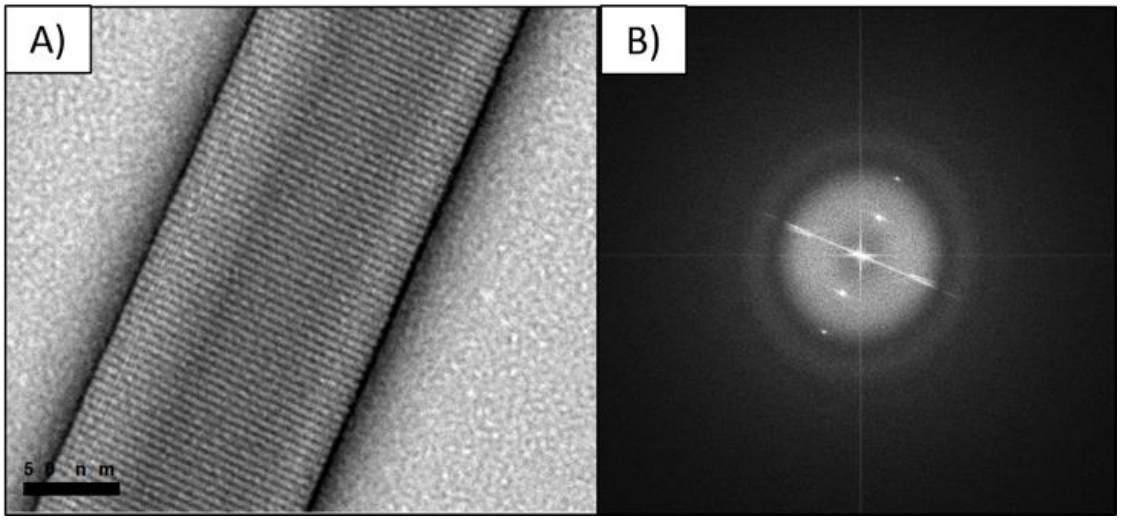

Figure 3.6 TEM image illustrating the banding pattern of hollow tubes of **TriNL** (A) with its corresponding fourier fast transform analysis (B).

Small and wide angle X-ray scattering (SWAXS) were used to determine additional information about the inter-helical organization within the tubular assemblies of TriNL. The q values obtained from the SWAXS spectrum (3.48 and 6.12 and 6.71 nm^{-1}, Figure 3.7 A), correspond to *d*-spacings of 1.81, 1.03 and 0.94 nm, respectively. Each of these values represent the (100), (110) and (200) lattice planes, with a lattice parameter (*a*) of 2.09 nm (Figure 3.7 B). Since the experimentally determined radius of the coiled-coil trimer is 0.67 nm (without side chains),[43, 44] these data suggest that the trimers pack in a hexagonal close-packed arrangement (Figure 3.7 B).[45] Additional q-values of 12.74 and 14.4 nm^{-1} correspond to inter-atomic distances of 0.49 and 0.44 nm, which may be attributed to shorter range inter-trimer hydrogen bonding and electrostatic interactions.

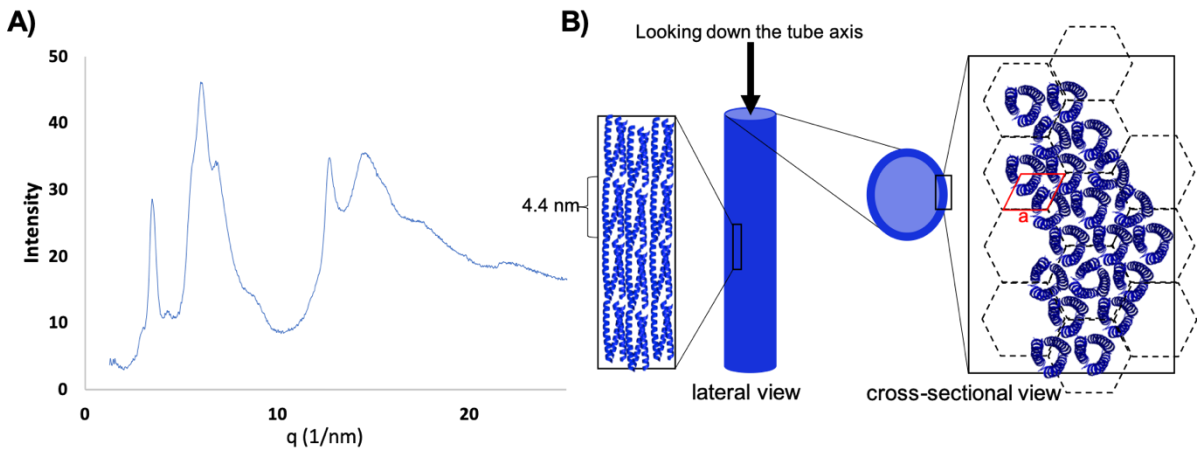

Figure 3.7 Small and wide angle x-ray scattering plot of the assembled tubes of **TriNL** (A) and proposed packing model of the trimers within the tubes (B).

Changing the buffer system from MOPS to phosphate (10 mM, pH 7.0) with the **TriNL** trimer also formed similar tubes, with slightly smaller dimensions (MOPS: length = 7.7 ± 5.7 μm, width = 0.9 ± 0.6 μm, n=20; phosphate buffer: length = 5.2 ± 2.5 μm, width = 0.7 ± 0.5 μm, n=20) (Figure 3.2 & Figure 3.8). Interestingly, the structures generated by the assembly of **TriNL** in phosphate buffer (10 mM) with added NaCl (150 mM) generated thinner fibrillar structures (width = 0.77 μm, n=20), that spanned lengths greater than 100 μm (Figure 3.9). The difference in structural morphology may be due to the effects of electrostatic screening of salt. It has been reported that salt can reduce electrostatic repulsion of peptides, causing a dramatic increase in fiber length.[47] These thinner needle-like structures may form from more limited lateral assembly of the coiled-coils, and may be related to the narrow fiber-like strips of material associating to form tubes in MOPS buffer.

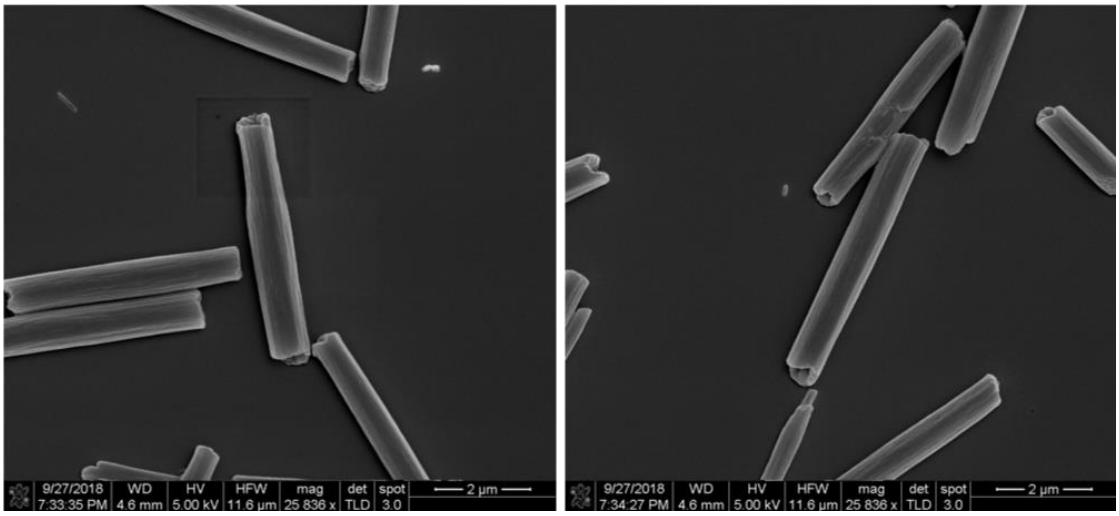

Figure 3.8 SEM images of 1 mM **TriNL** assembled in 10 mM PB buffer (pH 7.0, 30 min).

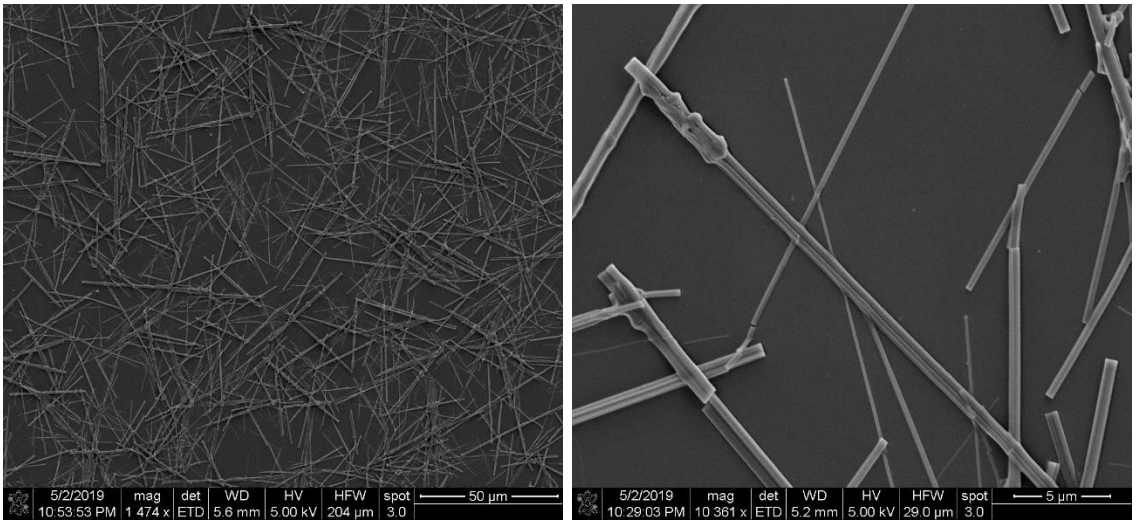

Figure 3.9 SEM micrographs of 1 mM **TriNL** assembled in 10 mM PBS buffer (pH 7.0, 30 min).

In consideration of these observations, as well as the TEM and X-ray diffraction analysis, we hypothesize that the trimers may assemble into thinner fibrillar structures, followed by their subsequent lateral association into tubes (Figure 3.10). The formation of these cylindrical tubes could be promoted by the ionic interaction between the fibers and/or through the non-covalent interactions displayed by polar sidechains present along the solvent-exposed faces of the coiled-coil. To further substantiate this hypothesis, nanotubes pre-formed in MOPS buffer were

resuspended in PBS buffer and their stability over time was investigated. After a period of 24 hours, the nanotubes were observed to erode into open tube-halves and shards, broken in segments along their long axis. In addition, shorter tubes were also observed, which are most likely formed from tube segmentation along its length (Figure 3.11). This further validates that both the lateral as well as head-to-tail trimer interactions play a vital role in nanotube formation.

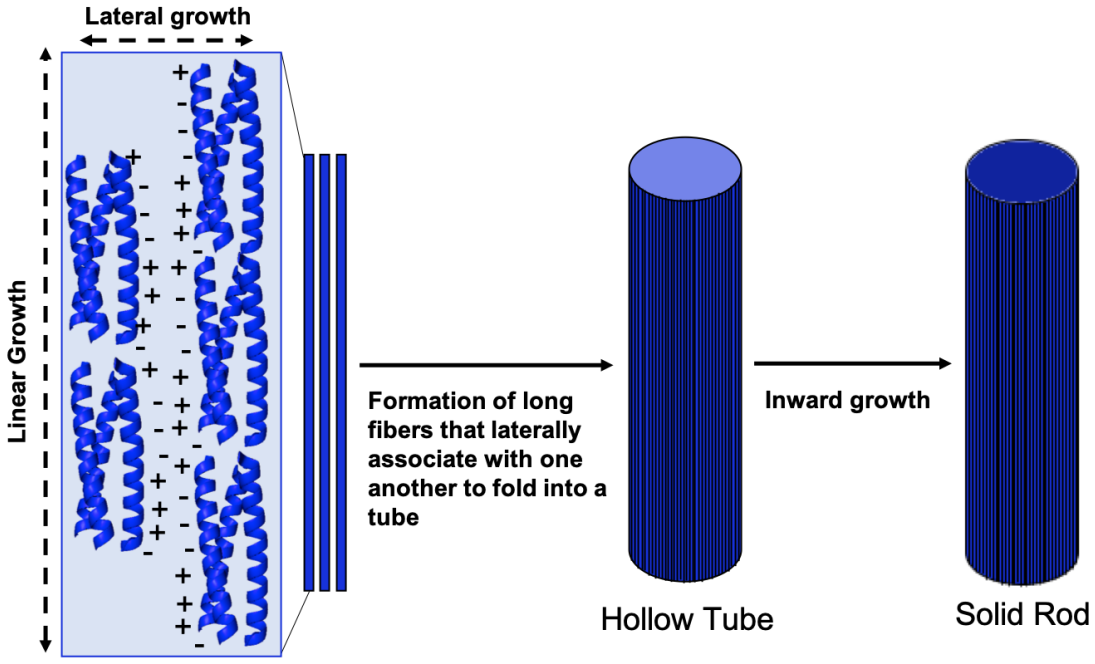

Figure 3.10 Schematic outlining the mechanistic hypothesis of **TriNL** assembly.

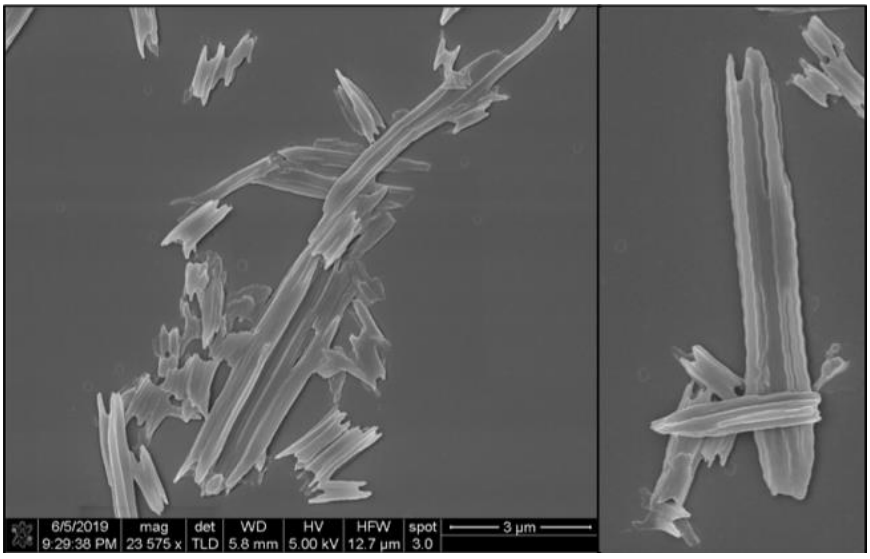

Figure 3.11 SEM micrographs of pre-formed **TriNL** tubes formed in 10 mM MOPS (pH 7.0, 30 min), resuspended in PBS buffer (24 hours).

3.2.4 Biomolecule Encapsulation

The hollow tubes, with their large aspect ratio, offer a substantial cavity for the non-covalent binding of biomolecules. Since the nanotubes displayed a positive zeta potential (Table 3.1), we investigated the addition of fluorescein-labelled anionic dextran (40,000 MW) to the assembly medium prior to initiating tube formation. The dextran was successfully encapsulated within the tubular cavities, as visualized by confocal light microscopy (Figure 3.12 A-C). 3D image regeneration of a z-stack acquisition shows the absence of fluorescent signal on the outsides of the tube, which would otherwise be visible at top and bottom focal planes (Figure 3.12 D-E). These data support the localization of the dextran within the tube cavities (Figure 3.13).

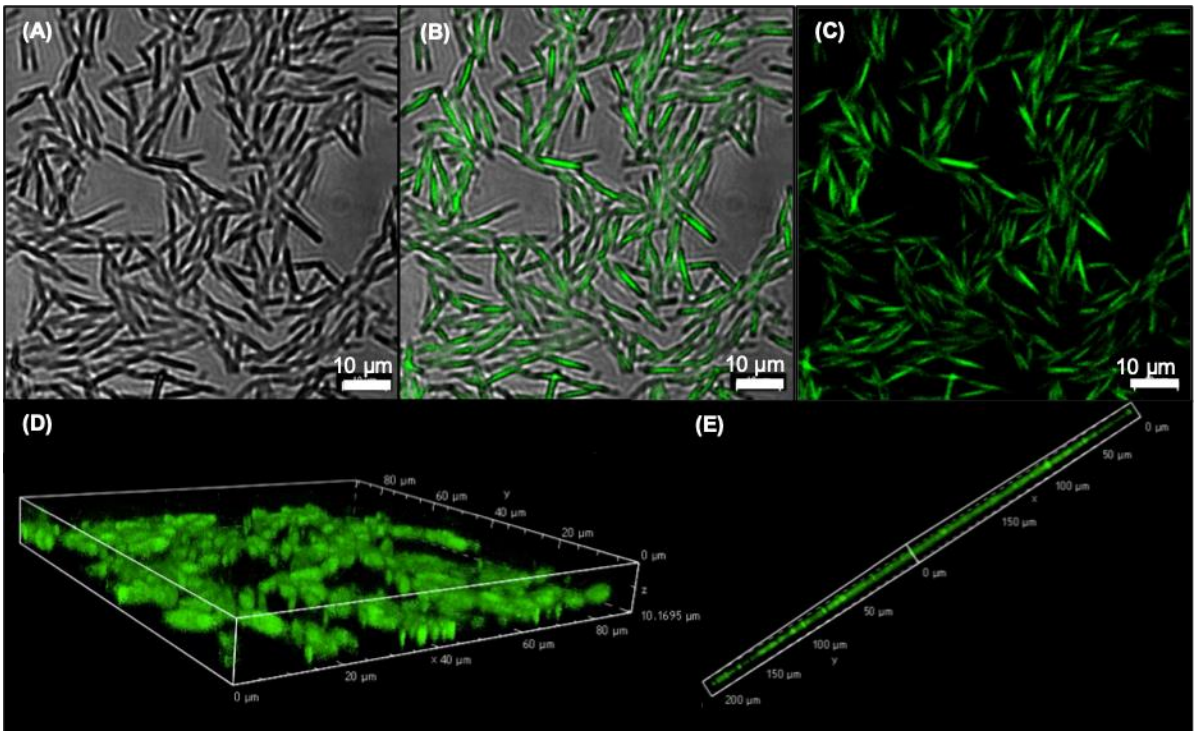

Figure 3.12 Confocal Images of **TriNL** tubes with fluorescein-labelled dextran anionic (40,000 MW) – (A) bright field channel, (B) combined channels and (C) green channel; (D & E) 3D regeneration of z-stack analysis.

To investigate the effects of dextran binding in the nanotubes, additional zeta-potential experiments were performed. The initial zeta-potential of the tubes was +16 mV in the absence of dextran (Table 3.1). Assembly of the tubes in the presence of anionic dextran gave a zeta potential of -1.3 mV. Also, adding Texas red-labelled neutral dextran (40,000 Da) during tube assembly led to no observed fluorescence of the nanotubes, nor does the zeta potential change (Figure 3.14, Table 3.1). These data strongly suggest that electrostatic interactions between the inner surface charge of the host tube and that of the guest molecules determine whether encapsulation occurs within the hollow cavities. It is also worth noting that the anionic dextran does not bind to any part of the tube when added post-tube formation (Figure 3.15). Furthermore, these data may point to an asymmetry in surface charge, with a positively charged inner tube surface and a neutral or negatively charged

outer tube surface. This would explain the ease of encapsulation of the biopolymer while forming the nanotube, as opposed to the less facile filling-in of the dextran into pre-formed tubes.

Table 3.1 Measured zeta potentials of the **TriNL** tubes

	Zeta Potential [mV]
TriNL Tubes	+15.9
TriNL Tubes w/Anionic 40k Fl-Dex (during assembly)	-1.3
TriNL Tubes w/Neutral 40k TR-Dex (during assembly)	+15.6

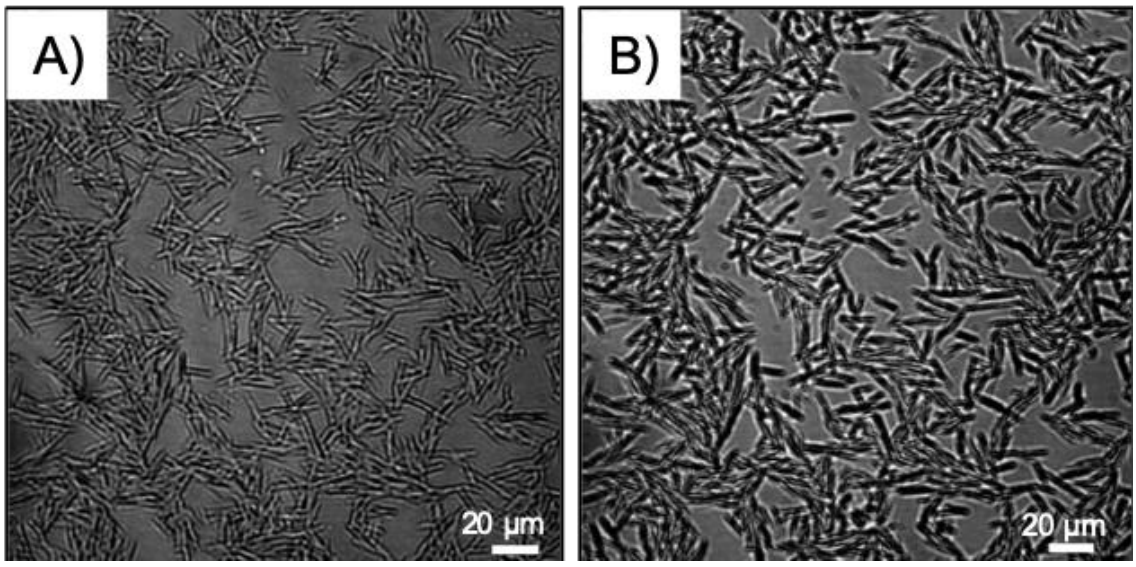

Figure 3.13 Confocal microscopy depicting merged channels of the 'top' and 'bottom' focal ends captured during z-stack analysis of 1 mM **TriNL** with fluorescein-labelled anionic dextran (40,000 Da) in 10 mM MOPS buffer.

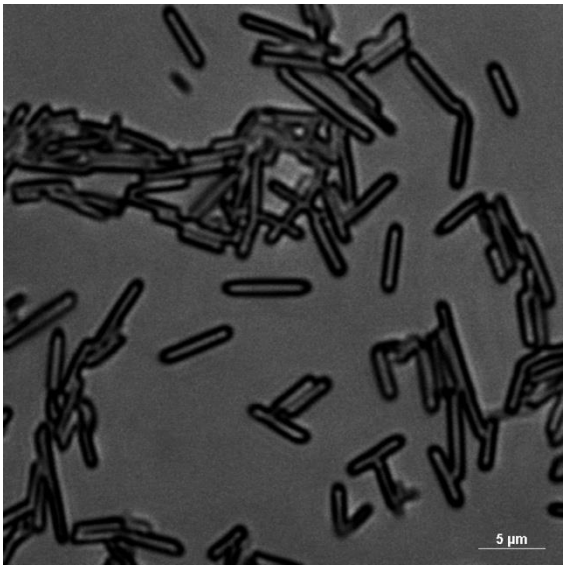

Figure 3.14 Confocal microscopy of merged channels of 1 mM **TriNL** tubes incubated with Texas Red Labelled Dextran (40,000 Da)-Neutral in 10 mM MOPS buffer; representative example of the z-stack analysis.

Figure 3.15 Confocal microscopy images (merged channels) of **TriNL** tubes (1 mM**)** incubated with Fluorescein Labelled Dextran-Anionic (40,000 Da) post-assembly in 10 mM MOPS buffer; representative example of the z-stack analysis.

3.3 Coiled-Coil Tetramer: Microbarrels

Bipyridine ligands along the monomeric backbone of collagen mimetic peptides have been used to allow for metal-assisted radial assembly. By varying the number of bipyridines, micrometer sized branched fibers,[48] disks,[49] hollow spheres[50] as well as a 3D mesh[51] were generated. The collagen triple helix is, however, limited by its tertiary conformation. Coiled-coils, on the other hand, give us access to a range of oligomers (two to seven), which can be harnessed to create an even wider range of structures. Herein we report the hierarchical assembly of a coiled-coil tetramer into barrel-like and spherical structures mediated by bipyridine-iron complexation.

3.3.1 Peptide Design

The higher order assembly of the trimers with bipyridine modifications (**TriByp1, TriByp2 and TriByp3**) into rectangular banded structures as well as the that of the unmodified trimer (**TriNL**) into tubes, has been discussed in the first part of this chapter and Chapter 2. In order to elucidate the effects of coiled-coil oligomerization on the resulting assembly, similar design principles were applied to the coiled-coil tetramer. Harbury *et al.* demonstrated the effect of changing the hydrophobic core on the resulting oligomerization state to produce two, three and four stranded coiled-coils.[43] More specifically, it was established that mutating the isoleucine residues to leucine at the *a* position of the trimer (**TriNL**), resulted in the formation of a tetramer (**TetNL**). In addition, we also proposed the mutation of the serine residue at the central *f* positon with a bipyridine group to form **TetByp1**, a coiled-coil building-block with four bipyridines (Figure 3.16). Thus, **TetNL** and **TetByp1** represent tetrameric analogs of the trimeric building-blocks, **TriNL** and **TriByp1,** respectively.

The peptide, **TetByp1** was synthesized using solid phase peptide synthesis (SPPS) with a low-loading ChemMatrix® rink amide resin as the solid support. Fmoc amino acids were coupled

with the aid of the HBTU coupling agent and DIEA. Fmoc-Lys-Mtt residues were substituted at the specified *f* positions in the coiled-coil heptad as per the design of **TetByp1**, in order to facilitate selective functionalization with the aromatic group, 4'-methyl-2,2'-bipyridine-4-carboxylic acid. Following the synthesis of the primary sequence, the sidechain protected Mtt groups were removed on resin under mild acidic conditions (30% HFIP in DCM), followed by the treatment with the bipyridine derivative, HBTU and DIEA. The peptides were cleaved from resin with a trifluoroacetic acid cocktail, purified to homogeneity and characterized with matrix-assisted laser desorption ionization time of flight (MALDI-TOF) mass spectrometry.

A)

B)

	abcdefg	abcdefg	abcdefg	abcdefg	abc
TriByp1	Ac - MKQIEDK	IEEILBK	IYHIENE	IARIKKL	IGE- NH_2
TetByp1	Ac - MKQIEDK	LEEILBK	LYHIENE	LARIKKL	LGE- NH_2

Figure 3.16 A) Change in oligomerization of the coiled-coil building block from trimer (**TriByp1**) to tetramer (**TetByp1**); B) Monomeric sequence of coiled-coils **TriByp1** and **TetByp1. B** residue represents a lysine modified bipyridine. In **TriNL** and **TetNL, B** is a serine (S) residue.

3.3.2 Higher-Order Non-Metal Assembly

The assembly of the unmodified tetrameric coiled-coil, **TetNL** has already been established.[52] At a concentration of 1 mM in MOPS buffer (10 mM), a cloudy precipitate was observed to form after 1 hour and imaged using TEM and SEM. We observed that the peptide

assembles into two-dimensional fibers, ~ 700 nm to a few microns in length (Figure 3.17 a). In addition, there were slightly larger, stiffer rod-like structures, indicated by the arrows (Figure 3.17 a). At longer time periods of 12 hours, we observed the formation of 3D rectangular blocks (Figure 3.17 b). From these data, we hypothesized that the fibers formed at shorter time periods further aggregate via non-covalent interactions into thicker rectangular blocks. It is evident that even without additional backbone modifications, the increase in oligomerization from trimer to tetramer leads to a dramatic shift in the resultant morphology. This is attributed to the increase in cumulative inter-coil interactions with an increase in number of helices from three (trimer) to four (tetramer).

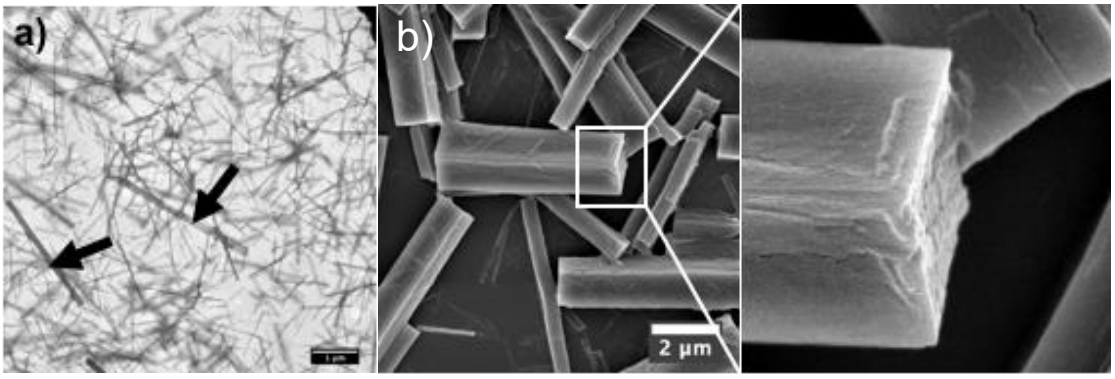

Figure 3.17 TEM micrographs depicting the assembly of 1 mM **TetNL** in MOPS buffer (pH 7.0, 20 mM) for a) 1 hour and, b) 12 hours.[52]

To initiate assembly of **TetByp1,** 250 μM of the peptide was incubated in buffer (10 mM MOPS, pH 7.0) for 24 hours. The resulting precipitate was collected by centrifugation and resuspended in water. These assemblies were visualized using electron microscopy. In the absence of metal ions, transmission electron microscopy images revealed the formation of rectangular-sheet like nanostructures (Figure 3.18). However, the **TetByp1** assemblies have somewhat smaller dimensions (l = 200-600 nm; b = 35-75 nm; n = 10) in contrast to the **TriByp1** assemblies. We have already established the effect of the number of bipyridine modifications on the trimer on the

resulting dimensions of their assemblies. The **TriByp1** (3 bipyridines), **TriByp2** (6 bipyridines) and **TriByp3** (9 bipyridines) coiled-coils generated nanostructures with aspect ratios (l:w) of 12:1, 4:1 and 0.9:1, respectively. With an increase in number of radially positioned bipyridines, there is an enhanced lateral assembly of the coiled-coils and thereby, a corresponding decrease in aspect ratio. Therefore, the aspect ratio of 9:1 obtained for the **TetByp1** (4 bipyridines) assemblies seems reasonable. These assemblies displayed a banding pattern with a spacing of 4.4 nm, measured from its FFT analysis, similar to that observed for the **TriByp** assemblies. This strongly suggests that like the trimeric coiled-coils, the tetrameric coiled-coils also align themselves perpendicular to the direction of banding within the assemblies. There is also no change in the length of each coiled-coil unit, which accounts for the same banding distance.

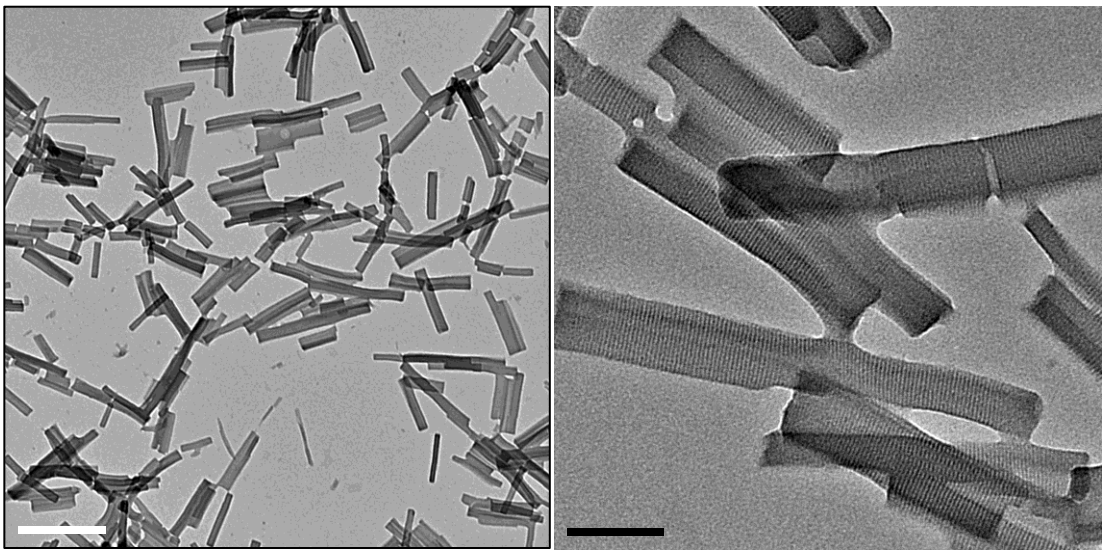

Figure 3.18 TEM micrographs depicting the assembly of **TetByp1** (250 μM) in MOPS buffer (pH 7.0, 10 mM) in the absence of metal ions after 24 hrs.

3.3.3 Metal-Mediated Assembly of **TetByp1**

In order to promote metal-mediated assembly, **TetByp1** (250 μM) was incubated with $FeCl_2$ (325 μM, 1.3 eq.) in MOPS buffer (10 mM, pH 7.0) for 24 hours. The pink-colored precipitate, as

result of Fe^{2+} complexation, was collected via centrifugation and resuspended in water. Transmission electron micrographs indicated the presence of high density cylindrical and circular morphologies as well as fiber-like structures (Figure 3.19 A-B). Further analysis of these structures using scanning electron microscopy revealed an assorted population consisting of barrel and sphere-like structures (Figure 3.19 C-D). The microbarrels, termed on account of their dimensions and shape (1-2 μm), appear to comprise several long rectangular shard-like structures. These rectangular shards are likely the non-metal assemblies of **TetByp1** and appear as the fiber-like structures in the TEM data (Figure 3.19 A-B). Upon addition of metal ions, the rectangular banded sheets appear to undergo a second-order of assembly. They self-organize in a concentric manner, with their individual lengths parallel to the axis of the microbarrel. Thus, the non-metal assemblies may serve as structural precursors for a more complex three dimensional architecture. The spheres also form with addition of metal, although the presence of any structural tiering is less apparent.

It is important to note that there is also a substantial presence of fiber-like structures observed (Figure 3.19) even after the addition of metal. This suggests that not all of the non-metal fiber-like structures were transformed into the three-dimensional architectures. Increasing the concentration of metal (Figure 3.20), did not succeed in the complete transformation of the fibers to the larger assemblies. At a peptide:metal ratio of 1:2 and 1:3 (Figure 3.20 A-D), we observed the formation of higher-order spheres with very few cylindrical barrel structures. At an even higher ratio of 1:5, the overall number of both spheres and barrels had significantly reduced (Figure 3.20 E-F). The disproportionate increase in metal-ion concentration, perhaps over-saturated the ligands, and may perturb the non-metal fibers from participating in a second order assembly. In order to utilize these structures for biological applications, mechanistic control of their assembly is

essential. Future experiments will include a comprehensive structural analysis, which will provide greater insight into their mode of self-assembly.

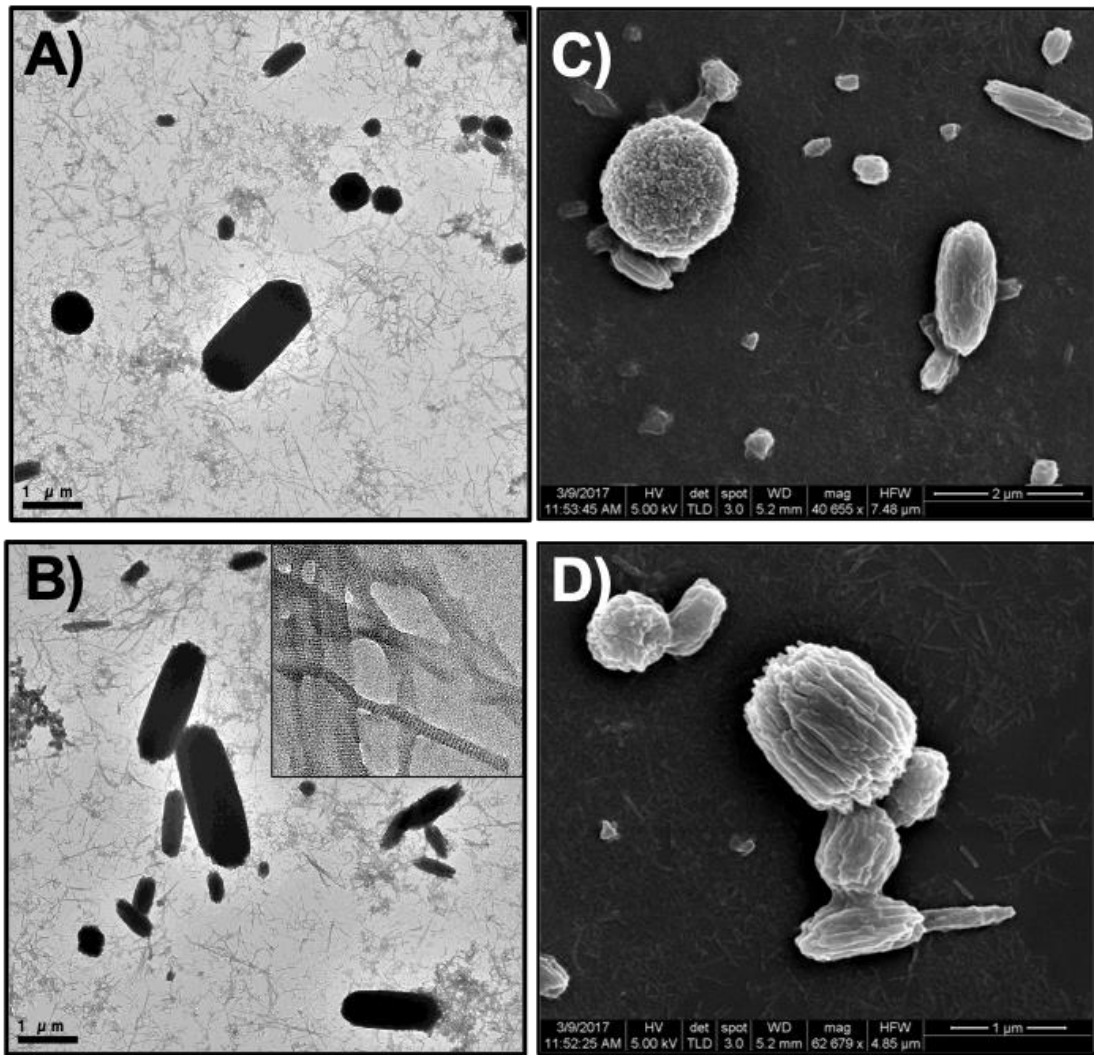

Figure 3.19 TEM (A, B) and SEM (C, D) micrographs depicting the assembly of **TetByp1** (250 μM) with $FeCl_2$ (325 μM) in MOPS buffer (10 mM) after 24 hrs. Inset in B shows the non-metal fiber-like assemblies formed in the background.

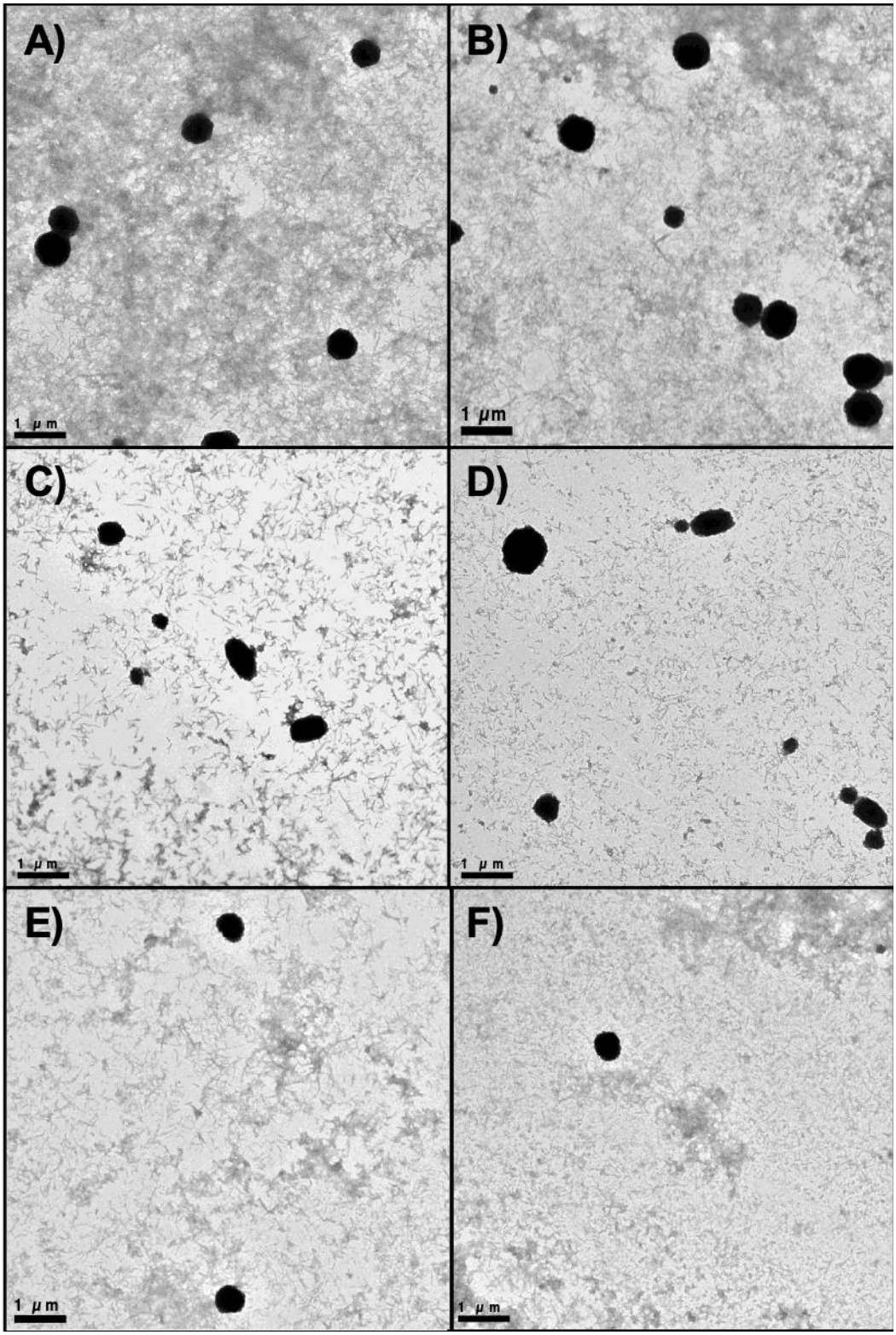

Figure 3.20 TEM micrographs depicting the effect of varying peptide metal ratio on the **TetByp1** assemblies: A-B) 1:2, C-D) 1:3 and, E-F) 1:5 peptide:metal ratio with 500 μM **TetByp1** in 10 mM MOPS buffer (pH 7.0) for 24 hours.

3.4 Conclusions

Self-organization of coiled-coil peptides into supramolecular tubular assemblies, induced by non-covalent interactions, holds immense potential for biomaterial development. The higher-order assembly of the isoleucine rich coiled-coil, **TriNL** was demonstrated to form nanotubes, with mechanistic evidence to suggest that the tube formation occurs in structural tiers. The first tier was marked by the initial organization of the coiled-coil building-blocks into long fiber-like strands. We hypothesized that this was followed by subsequent strand association into tubes to form the second tier, and a final transition into solid tubes or rods at longer time periods, marking the third tier. The hollow tubes selectively encapsulate fluorescently-labelled anionic dextran within their cavities through selective internal surface interactions. Furthermore, exploring the effects of molecular confinement within chemically tunable and biocompatible tubes can lead to smart responsive systems with a broad range of biomedical applications. Additionally, the tetrameric peptide building-blocks, **TetNL** and **TetByp1** also demonstrated multi-tier self-organization to form well-defined 3D architectures, namely rectangular blocks and microbarrels. Such construction was achieved through a very subtle change within the coiled-coil motif, i.e., a four amino acid change in the peptide sequence with a shift in oligomerization from trimer to tetramer, leading to dramatic transformations in the resulting morphologies. Consequentially these unique morphologies expands the possibilities for applications of the biomaterials in biological and material science.

3.5 Materials and Methods

3.5.1 Materials

Fmoc-protected amino acids Fmoc-Met, Fmoc-Lys(Boc), Fmoc-Lys(Mtt), Fmoc-Ser(tBu), Fmoc-Gln(Trt), Fmoc-Ile, Fmoc-Leu, Fmoc-Arf(Pbf), Fmoc-His, Fmoc-Glu(tBu), Fmoc-Tyr(tBu),

Fmoc-Ala, Fmoc-Gly, Fmoc-Asp(tBu), and activation agent HBTU (O-benzotriazole-N,N,N',N'-tetramethyl-uronium-hexafluoro-phosphate) were purchased from ChemPep Inc (Wellington, Florda, USA). Diisopropylethylamine (DIEA) was purchased from ChemImpex, Inc (Wood Dale, IL, USA). ChemMatrix rink amide resin was purchased from pcas Biomatrix Inc (Saint-Jean-sur-Richelieu, Quebec, Canada). Dichloromethane (DCM), N,N-dimethylformamide (DMF), methanol (MeOH), trifluoroacetic acid (TFA), triisopropylsilane (TIPS), diethyl ether, selenium(IV) oxide, silver(I) nitrate and 4, 4'-dimethylbipyridine were purchased from Sigma-Aldrich (St. Louis, MO). Acetic anhydride was purchased from Macron Fine Chemicals. Dextran, Fluorescein (40,000 MW, anionic) and dextran, TexasRed (40,000 MW, neutral) were purchased from ThermoFisher Scientific.

3.5.2 Solid Phase Peptide Synthesis

TriNL and **TetByp1** were synthesized using standard Fmoc protected amino acids on Chemmatrix ® Rink Amide resin (500 mg, 0.24 mmol/g). The desired amino acid was coupled to the free amine using HBTU (4 eq, 0.48 mmol) and DIEA (8 eq, 0.96 mmol) as coupling reagents dissolved in DMF. The mixture was added to the reaction flask containing the solid support (resin) and this was allowed to agitate for 3 hours at room temperature. After couplings, the solution was drained and the resin was washed with DMF (2 X 10 mL), DCM (2 X 10 mL), MeOH (2 X 10 mL), DCM (2 X 10 mL), and DMF (2 X 10 mL). To remove the Fmoc protecting group, the resin-bound peptide was treated with piperidine (25% in DMF, 15 mL) and reacted for 30 minutes. The piperidine solution was drained and the resin was subsequently washed with DMF, DCM, MeOH, DCM, and DMF (3 X 10 mL each). The coupling and Fmoc deprotection was monitored with the Kaiser (detection of 1° amines) test. This process was repeated until the full-length peptide was

synthesized. After the final Fmoc deprotection, the N-terminal amino acid was acetylated using 5% acetic anhydride and 8.5% DIEA in DMF (v/v) for 30 minutes.

The Mtt protecting group was removed by treating the resin-bound resin peptide with 1.8% TFA in DCM (10 x 10 mL) with deprotection times of 3 minutes and DCM washes (10 mL) in between each treatment. This was followed by the coupling of 4'–methyl-2,2'bipyridine-4-carboxylic acid to the deprotected lysines using HBTU (6 eq, 0.72 mmol) and DIEA (12 eq, 1.44 mmol), dissolved in DMF. The resin was finally washed with DMF, DCM, MeOH, DCM, and DMF (2 X 10 mL each).

The resin bound peptide was then dried under reduced pressure and cleaved from resin by treatment with TFA/TIPS/H_2O (95: 2.5: 2.5) (15 mL) (v/v) for 2 hours. The TFA cocktail was drained into a falcon tube. The resin was washed twice with TFA (15 mL) and twice with DCM (15 mL). These filtrates were combined and the solvents were removed under reduced pressure. The peptide was precipitated with cold diethyl ether (50 mL). The precipitate was collected via centrifugation. The supernatant was decanted, and to this was added fresh diethyl ether (50 mL). This was centrifuged once more and again the supernatant was decanted. The pellet was initially dried under flow of nitrogen, followed by drying under pressure. After determination of the mass, the peptide were suspended in water (10 mg/mL) and purified by reverse phase (RP) HPLC on a Luna C18 (250 x 21.20 mm, 100 Å pore size, 10 micron, Phenomenex) column. Eluent conditions consisted of solvent A (CH_3CN/0.1% TFA) and solvent B (H_2O/0.1% TFA) with a 60-minute gradient of 20-90% and a flow rate of 12 mL/min monitored at wavelengths of 214 nm and 254 nm (Appendix: A-4 and A-5). The peptide was subsequently characterized using MALDI-TOF.

3.5.3 Assembly of Tubes

A solution of the **TriNL** peptide (1 mM) in MOPS buffer (10 mM, pH 7.0) (total sample volume of 100 μL) was incubated at room temperature for 30 minutes, during which a precipitate formed. This precipitate was washed by centrifuging the sample at 10 g for 3 minutes, followed by the removal of the supernatant and addition of water. This process was repeated two more times for each sample, with the final suspension being in water.

3.5.4 Assembly with Dextrans

A solution of the **TriNL** peptide (1 mM) in MOPS buffer (10 mM) was incubated in the presence of fluorescently-labelled dextran (2 mg/ml) at room temperature for 1 hour (total sample volume of 100 μL). This was followed by a similar rinsing procedure outlined above.

3.5.5 Assembly of the Banded Rectangular Sheets

A solution of the **TetByp1** peptide (250 μM) in MOPS buffer (10 mM, pH 7.0) was incubated at room temperature for 24 hours, during which a colorless precipitate formed. This precipitate was washed by centrifuging the sample at 10 g for 3 minutes, followed by the removal of the supernatant and addition of water. This process was repeated two more times for each sample, with the final suspension being in water.

3.5.6 Assembly of Microbarrels

A solution of the **TriNL** peptide (250 μM) in MOPS buffer (10 mM, pH 7.0) along with 1.3 eq. of $FeCl_2$ (325 μM) (total sample volume of 100 μL) was incubated at room temperature for 24 hours, during which a pink colored precipitate formed. This precipitate was washed by centrifuging the sample at 10 g for 3 minutes, followed by the removal of the supernatant and addition of water.

This process was repeated two more times for each sample, with the final suspension being in water.

3.5.7 Transmission Electron Microscopy

An aliquot of the assembly in water (3.5 µL) was placed directly onto the surface of the grid. This was left to stand for 2 minutes; the water was then wicked away. The grid was rinsed through stain droplets and blotted dry. Staining was done with 2% uranyl acetate. Samples were imaged using a Tecnai T20 TEM (FEI Company, Hillsboro, OR, USA) operated at 100 KV, with a spot size of 3, 200 µm condenser aperture and 70 µm objective aperture. Images were captured using an SIA L3C 4- megapixel CCD camera (Scientific Instruments and Application, Duluth, GA). Samples were fixed on a 400-mesh copper grid coated in formvar with a carbon film (Ted Pella, Redding, CA, USA) which were previously glow discharged.

3.5.8 Atomic Force Microscopy

A 5 µL aliquot of the rinsed assembly was placed on freshly cleaved Mica surface (Ted Pella, INC). This was left to air dry. Samples were imaged in air in tapping mode on the Asylum Cypher ES Microscope using silicon probes having a resonance frequency of 265-400 kHz (Ted Pella, INC – Tap300-G-10). All AFM images were obtained at 25 °C.

3.5.9 Scanning Electron Microscopy

Samples were prepared by placing a 5 µL aliquot of the assembly in water, on the surface of a glass cover slip adhered to the specimen stub with double sided copper tape. The samples were left to air dry prior to being coated with platinum for 60 seconds using a sputter coater. Samples were imaged using an FEI NOVA NANO SEM field emission scanning electron microscope using the Everhart-Thornley (ETD) or the high-resolution through the lens (TLD) detectors. Samples

were imaged at an accelerating voltage of 5 kV with optimal working distances between 3-5 mm and a 30 μm aperture.

3.5.10 Confocal Light Microscopy

For the fluorescent samples, a 5 μL droplet of each sample (**TriNL** tubes with dextran) was placed on a coverslip and visualized under an inverted 60x and 100x oil objectives of a Nikon AIRSi confocal microscope. Fluorescein and Texas Red were excited using 488 nm and 555nm excitation lasers, respectively.

3.5.11 Small & Wide Angle X-ray Scattering (SWAXS)

For X-ray scattering, samples were prepared by drop-casting of an aliquot (4 μL) of the assembly in water on scotch tape and leaving it to air dry. The sample was confined within a circular area of 0.8 cm^2. Six different nanotube assemblies (1 mM **TriNL** in 10 mM MOPS) were parallelly prepared (as described in section 3.5.3) and drop-casted within the same concentrated area. The measurements were performed using an Anton-Paar SAXSPoint 2.0 system operated at near-vacuum conditions with a Primux 100 micro microfocus X-ray source (Cu). Diffraction patterns were acquired with an acquisition time of 15 mins (average of 3) by means of a 2D EIGER R series Hybrid Photon Counting (HPC) detectors and High-resolution WAXS module (EIGER2 R series). Measurements were obtained at sample-detector distances of 113 mm and 79 mm.

3.6 References

1. Zhang, S. Fabrication of Novel Biomaterials through Molecular Self-Assembly. *Nat. Biotechnol.* **2003,** *21* (10), 1171-1178.
2. Mendes, A. C.; Baran, E. T.; Reis, R. L.; Azevedo, H. S., Self-Assembly in Nature: Using the Principles of Nature to Create Complex Nanobiomaterials. *Wiley Interdiscip. Rev.: Nanomed. Nanobiotechnol.* **2013,** *5*(6), 582-612.

3. Boyle, A. L.; Woolfson, D. N. De Novo Designed Peptides for Biological Applications. *Chem. Soc. Rev.* **2011,** *40* (8), 4295-4306.

4. Ekiz, M. S.; Cinar, G.; Khalily, M. A.; Guler, M. O. Self-Assembled Peptide Nanostructures for Functional Materials. *Nanotechnol.* **2016,** *27*, 402002-402039.

5. Webber, M. J.; Berns, E. J.; Stupp, S. I. Supramolecular Nanofibers of Peptide Amphiphiles for Medicine. *Isr. J. Chem.* **2013,** *53*, 530-554.

6. de la Rica, R.; Matsui, H. Applications of Peptide and Protein-Based Materials in Bionanotechnoogy. *Chem. Soc. Rev.* **2010,** *39*, 3499-3509.

7. Gratton, S. E. A.; Ropp, P. A.; Phlhaus, P. D.; Luft, J. C.; Madden, V. J.; Napier, M. E.; DeSimone, J. M. The Effect of Particle Design on Cellular Internalization Pathways. *Proc. Natl. Acad. Sci. U. S. A.* **2008,** *105* (33), 11613-11618.

8. Geng, Y.; Dalhaimer, P.; Cai, S.; Tsai, R.; Tewari, M.; Minko, T.; Discher, D. E. Shape Effects of Filaments Versus Spherical Particles in Flow and Drug Delivery. *Nat. Nanotechnol.* **2007,** *2* (4), 249-255.

9. Hsieh, W.-H.; Liaw, J. Applications of Cyclic Peptide Nanotubes (Cpnts). *J. Food Drug Anal.* **2019,** *27* (1), 32-47.

10. Odom, T. W.; Huang, J.-L.; Kim, P.; Lieber, C. M. Structure and Electronic Properties of Carbon Nanotubes. *J. Phys. Chem. B* **2000,** *104*, 2794-2809.

11. Ciraci, S.; Dag, S.; Yildirim, T.; Gülseren, O.; Senger, R. T. Functionalized Carbon Nanotubes and Device Applications. *J. Phys.: Condens. Matter* **2004,** *16* (29), 901-960.

12. Singh, P. Carbon Nanotube and Their Biomedical Applications: A Review. **2010**, *7*, 389-396.

13. Singh, H.; Chauhan, A.; Jindal, P. Fabrication of Al2024/MWCNT Composite. *Res. J. Eng. Technol.* **2017,** *8* (3), 191-194.

14. Hrapovic, S.; Liu, Y.; Male, K. B.; Luong, J. H. T. Electrochemical Biosensing Platforms Using Platinum Nanoparticles and Carbon Nanotubes. *Anal. Chem.* **2004,** *76* (4), 1083-1088.

15. Adeniyi, A. A.; Lisa, T.; Robert, L. T.; Vincent, T. R. Preparation of Water Soluble Carbon Nanotubes and Assessment of Their Biological Activity in Embryonic Zebrafish. *Int. J. Biomed. Nanosci. Nanotechnol.* **2013,** *3* (1-2), 38-51.

16. Nakashima, N. Soluble Carbon Nanotubes and Their Applications. *J. Nanosci. Nanotechnol.* **2006,** *6* (11), 16-27.

17. Ghadiri, M. R.; Granja, J. R.; Milligan, R. A.; McRee, D. E.; Khazanovich, N. Self-Assembling Organic Nanotubes Based on a Cyclic Peptide Architecture. *Nature* **1993,** *366* (6453), 324-327.

18. Ghadiri, M. R.; Granja, J. R.; Buehler, L. K. Artificial Transmembrane Ion Channels from Self-Assembling Peptide Nanotubes. *Nature* **1994,** *369*, 301-304.

19. Hartgerink, J. D.; Granja, J. R.; Milligan, R. A.; Ghadiri, M. R. Self-Assembling Peptide Nanotubes. *J. Am. Chem. Soc.* **1996,** *118*, 43-50.

20. Shahabi, M.; Raissi, H. Assessment of Solvent Effects on the Inclusion Behaviour of Pyrazinamide Drug into Cyclic Peptide Based Nanotubes as Novel Drug Delivery Vehicles. *J. Mol. Liq.* **2018,** *268*, 326-334.

21. Rodriguez-Vasquez, N.; Garcia-Fandino, R.; Aldegunde, M. J.; Brea, J.; Loza, M. I.; Amorin, M.; Granja, J. R. Cis-Platinum Complex Encapsulated in Self-Assembling Cyclic Peptide Dimers. *Org. Lett.* **2017,** *19*, 2560-2563.

22. Santhanamoorthi, N.; Kolandaivel, P.; Adler-Abramovich, L.; Gazit, E.; Filipek, S.; Viswanathan, S.; Strzelczyk, A.; Renugopalakrishnan, V. Diphenylalanine Peptide Nanotube: Charge Transport, Band Gap and Its Relevance to Potential Biomedical Applications. *Adv. Mater. Lett.* **2011,** *2* (2), 100-105.

23. Porter, S. L.; Coulter, S. M.; Pentlavalli, S.; Thompson, T. P.; Laverty, G. Self-Assembling Diphenylalanine Peptide Nanotubes Selectively Eradicate Bacterial Biofilm Infection. *Acta Biomater.* **2018,** *77*, 96-105.

24. Kim, J. H.; Lee, M.; Lee, J. S.; Park, C. B. Self-Assembled Light-Harvesting Peptide Nanotubes for Mimicking Natural Photosynthesis. *Angew. Chem. Int., Ed.* **2011,** *51* (2), 517-520.

25. Lee, J.-H.; Hey, K.; Schulz-Schönhagen, K.; Lee, J. H.; Desai, M. S.; Jin, H.-E.; Lee, S.-W. Diphenylalanine Peptide Nanotube Energy Harvesters. *ACS Nano* **2018,** *12* (8), 8138-8144.

26. Yemini, M.; Reches, M.; Gazit, E.; Rishpon, J. Peptide Nanotube-Modified Electrodes for Enzyme-Biosensor Applications. *Anal. Chem.* **2005,** *77*, 5155-5159.

27. Silva, R. F.; Araújo, D. R.; Silva, E. R.; Ando, R. A.; Alves, W. A. L-Diphenylalanine Microtubes as a Potential Drug-Delivery System: Characterization, Release Kinetics, and Cytotoxicity. *Langmuir* **2013,** *29* (32), 10205-10212.

28. Handelman, A.; Shalev, G.; Rosenman, G. Symmetry of Bioinspired Short Peptide Nanostructures and Their Basic Physical Properties. *Isr. J. Chem.* **2015,** *55*, 637-644.

29. Handelman, A.; Natan, A.; Rosenman, G. Structural and Optical Properties of Short Peptides: Nanotubes-to-Nanofibers Phase Transformation. *J. Pept. Sci.* **2014,** *20* (7), 487-493.

30. Zimenkov, Y.; Dublin, S. N.; Ni, R.; Tu, R. S.; Breedveld, V.; Apkarian, R. P.; Conticello, V. P. Rational Design of a Reversible pH-Responsive Switch for Peptide self-Assembly. *J. Am. Chem. Soc.* **2006,** *128*, 6770-6771.

31. Tsurkan, M. V.; Ogawa, M. Y. Metal-Peptide Nanoassemblies. *Chem. Comm.* **2004,** (18), 2092-2093.

32. Dublin, S. N.; Conticello, V. P. Design of a Selective Metal Ion Switch for Self-Assembly of Peptide-Based fibrils. *J. Am. Chem. Soc.* **2007,** *130*, 49-51.

33. Gunasekar, S. K.; Anjia, L.; Matsui, H.; Montclare, J. K. Effects of Divalent Metals on Nanoscopic Fiber Formation and Small Molecule Recognition of Helical Proteins. *Adv. Funct. Mater.* **2012,** *22* (10), 2154-2159.

34. Anzini, P.; Xu, C.; Hughes, S.; Magnotti, E.; Jiang, T.; Hemmingsen, L.; Demeler, B.; Conticello, V. P. Controlling Self-Assembly of a Peptide-Based Material Via Metal-Ion Induced Registry Shift. *J. Am. Chem. Soc.* **2013,** *135* (28), 10278-10281.

35. Xu, C.; Liu, R.; Mehta, A. K.; Guerrero-Ferreira, R. C.; Wright, E. R.; Dunin-Horkawicz, S.; Morris, K.; Serpell, L. C.; Zuo, X.; Wall, J. S.; Conticello, V. P. Rational Design of Helical Nanotubes from Self-Assembly of Coiled-Coil Lock Washers. *J. Am. Chem. Soc.* **2013,** *135* (41), 15565-15578.

36. Woolfson, D. N. The Design of Coiled-Coil Structures and Assemblies. *Adv. Protein Chem.* **2005,** *70*, 79-112.

37. Apostolovic, B.; Danial, M.; Klok, H. A. Coiled Coils: Attractive Protein Folding Motifs for the Fabrication of Self-Assembled, Responsive and Bioactive Materials. *Chem. Soc. Rev.* **2010,** *39* (9), 3541-3575.

38. Woolfson, D. N.; Bartlett, G. J.; Bruning, M.; Thomson, A. R. New Currency for Old Rope: From Coiled-Coil Assemblies to Alpha-Helical Barrels. *Curr. Opin. Struct. Biol.* **2012,** *22* (4), 432-441.

39. Egelman, E. H.; Xu, C.; DiMaio, F.; Magnotti, E.; Modlin, C.; Yu, X.; Wright, E.; Baker, D.; Conticello, V. P. Structural Plasticity of Helical Nanotubes Based on Coiled-Coil Assemblies. *Structure* **2015,** *23* (2), 280-289.

40. Fletcher, J. M.; Harniman, R. L.; Barnes, F. R. H.; Boyle, A. L.; Collins, A.; Mantell, J.; Sharp, T. H.; Antognozzi, M.; Booth, P. J.; Linden, N.; Miles, M. J.; Sessions, R. B.; Verkade, P.; Woolfson, D. N. Self-Assembling Cages from Coiled-Coil Peptide Modules. *Science* **2013,** *340*, 595-599.

41. Thomas, F.; Burgess, N. C.; Thomson, A. R.; Woolfson, D. N. Controlling the Assembly of Coiled-Coil Peptide Nanotubes. *Angew. Chem., Int. Ed.* **2016,** *55*, 987-991.

42. Tian, Y.; Polzer, F. B.; Zhang, H. V.; Kiick, K. L.; Saven, J. G.; Pochan, D. J. Nanotubes, Plates, and Needles: Pathway-Dependent Self-Assembly of Computationally Designed Peptides. *Biomacromolecules* **2018,** *19* (11), 4286-4298.

43. Harbury, P. B.; Zhang, T.; Kim, P. S.; Alber, T. A Switch between Two-, Three-, and Four-Stranded Coiled Coils in GCN4 Leucine Zipper Mutants. *Science* **1993,** *262* (5138), 1401-1407.

44. Harbury, P. B.; Kim, P. S.; Alber, T. Crystal Structure of an Isoleucine-Zipper Trimer. *Nature* **1994,** *371*, 80-83.

45. Nambiar, M.; Wang, L.-S.; Rotello, V.; Chmielewski, J. Reversible Hierarchical Assembly of Trimeric Coiled-Coil Peptides into Banded Nano- and Micro- Structures. *J. Am. Chem. Soc.* **2018,** *140* (40), 13028-13033.

46. Nepal, M.; Sheedlo, M. J.; Das, C.; Chmielewski, J. Accessing Three-Dimensional Crystals with Incorporated Guests through Metal-Directed Coiled-Coil Peptide Assembly. *J. Am. Chem. Soc.* **2016,** *138* (34), 11051-11057.

47. Dong, H.; Paramonov, S.; Aulisa, L.; Bakota, E.; Hartgerink, J. Self-Assembly of Multidomain Peptides: Balancing Molecular Frustration Controls Conformation and Nanostructure. *J. Am. Chem. Soc.* **2007,** *129* (41), 12468-12472.

48. Przybyla, D. E.; Chmielewski, J. Metal-Triggered Radial Self-Assembly of Collagen Peptide Fibers. *J. Am. Chem. Soc.* **2008,** *130*, 12610-12611.

49. Przybyla, D. E.; Chmielewski, J. Metal-Triggered Collagen Peptide Disk Formation. *J. Am. Chem. Soc.* **2010,** *132*, 7866-7867.

50. Przybyla, D. E.; Rubert Perez, C. M.; Gleaton, J.; Nandwana, V.; Chmielewski, J. Hierarchical Assembly of Collagen Peptide Triple Helices into Curved Disks and Metal Ion-Promoted Hollow Spheres. *J. Am. Chem. Soc.* **2013,** *135* (9), 3418-3422.

51. Pires, M. M.; Przybyla, D. E.; Chmielewski, J. A Metal-Collagen Peptide Framework for Three-Dimensional Cell Culture. *Angew. Chem., Int. Ed.* **2009,** *48* (42), 7813-7817.

52. Nepal, M. Peptides as Tools to Develop Novel Therapeutics and Soft Materials. PhD. Dissertation, Purdue University, West Lafayatte, IN, 2017.

CHAPTER 4. METAL-PROMOTED ASSEMBLY OF HOMOCYSTEINE-STAPLED HELICAL BUNDLES INTO MICROSPHERES

4.1 Introduction

The design of supramolecular assemblies constructed from non-covalently assembled secondary and tertiary motifs such as coiled-coils, has been extensively explored. However, such assembly precursors may be limited by their lack of stability in different reaction conditions.[1] This is particularly apparent for short alpha-helical peptides which typically do not exhibit much of an alpha-helical conformation in solution.[2] This is because the entropic cost associated with the folding of the chain is not compensated by sufficient stabilizing interactions.[3] Covalent trapping of the tertiary conformation can potentially alleviate these limitations, and pave the way for chemically sturdier building-blocks for hierarchical assembly.

In nature, the four-helix bundle is a common structural motif in several protein structures that play a vital role in protein hormones and cytokines,[4, 5] redox and enzymatic functions,[6-8] scaffolds for metal and co-factor binding as well as strengthening protein-protein interactions that direct DNA binding,[9, 10] among others. As such, four-helix bundles have become key targets for de novo protein design and building-blocks for higher-order assemblies. These bundles comprise amphiphilic helices with hydrophobic residues buried within their consolidated cores. The Chmielewski lab has successfully established a novel method to covalently stabilize short 16 amino acid alpha helical peptide into four- and five-helix bundles.[11] The peptide, **L6HC**, based on the design principles outlined by DeGrado *et al.*,[12-18] contains a leucine rich hydrophobic face (six leucines) and a polar face comprising glutamic acids and lysines. These polar residues promote intramolecular salt bridges as well as interhelical electrostatic contacts. It was designed to form a

self-assembled helix bundle, enabling the burial of the hydrophobic groups from the solvent. Located at the interface of both of the polar and non-polar faces are acetamidomethyl (Acm) protected-homocysteine residues. These homocysteines were suitably positioned to enable inter-helical cross-linking via the formation of disulfide bridges. The incorporation of the homocysteines was to ensure a sufficient distance between two neighboring helices within the bundle to form a disulfide bond. Prior to cross-linking, the monomer was shown to adopt an aggregation state of four in aqueous solution. However, after the homocysteine-crosslinking reaction, the covalent stabilization of these helices resulted in the successful formation of both tetrameric (**4HB**) and pentameric (5**HB**) helical bundles.[11, 19]

These amphiphilic helices can thus, be efficiently transformed into stable 64 and 80 amino acid bundled proteins, that are approximately half the length of the GCN4 coiled-coils.[20-22 23] At this junction, it is important to highlight the distinction between these bundle and the coiled-coil structures described in the earlier part of this thesis. The difference primarily lies in the side-chain mediated helix-helix packing. Short peptides, less than 14 amino acids, tend to be free and often display irregular helical packing. Longer peptides typically associate in either a less specific ridges-into-grooves (RIG) or via the knob-into-hole (KIH) interactions. The KIH interactions, as discussed earlier, are characteristic of coiled-coil packing. The globular helical bundles tend to adopt an RIG packing pattern.[24-26] Based on this, we hypothesized that strategic chemical modifications of these four- and five-helix bundle proteins would lead to a novel library of building-blocks that can be further harnessed for higher-order assembly into peptide-based materials.

4.2 Results and Discussion

4.2.1 Peptide Design

In an effort to promote higher order assembly of helical bundles, we proposed the addition of ligands for metal ions at the *N* and *C* termini of the 16-amino acid amphiphilic helix, **L6HC** (Figure 4.1 A). Nitrilotriacetic acid (NTA) and di-histidine ligands were chosen for their high binding affinities for metal ions. We hypothesized that upon addition of metal, complementary metal-ligand coordination would promote a head-to-tail or linear assembly of the alpha-helices. The new ligand-modified monomer, **L6HCL** (Figure 4.1 A-C) would be further subjected to the homocysteine cross-linking reaction to yield covalently-stabilized bundles potentially comprising both the tetrameric (**4HBL**) and pentameric (**5HBL**) forms. Therefore, the higher-order assembly of these disulfide-linked helical bundle building-blocks would be two-fold (Figure 4.1 D): i) metal-assisted linear growth and, ii) inter-bundle electrostatics facilitated lateral growth.

A)

Monomer	Amino Acid Sequence
L6HC	Ac-E-L-L-E-K-L-**HCys**-K-**HCys**-L-E-E-L-L-K-K-NH_2
L6HCL	NTA-E-L-L-E-K-L-**HCys**-K-**HCys**-L-E-E-L-L-K-K-H-H-NH_2

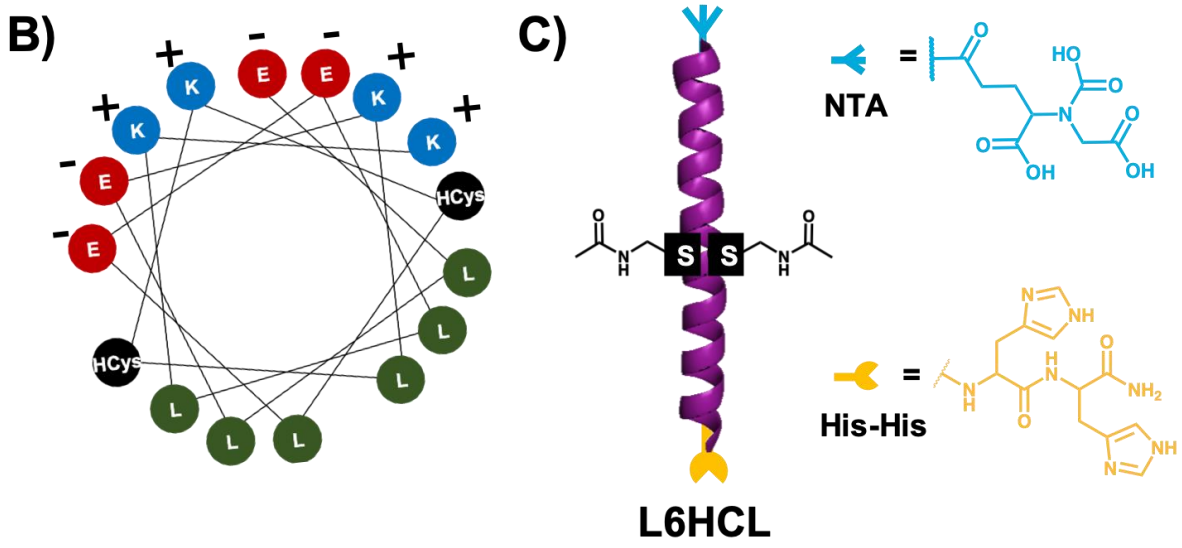

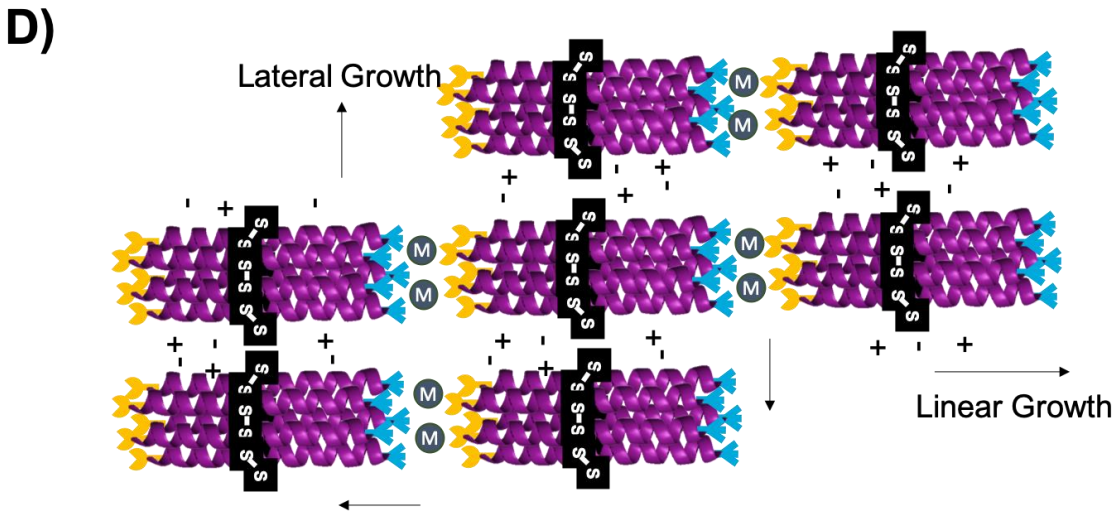

Figure 4.1 A) Amino acid sequence of monomers, **L6HC** and **L6HCL**, B) their corresponding helical wheel diagram, C) alpha-helical representation of **L6HCL** and, D) schematic representation of metal-mediated linear growth and electrostatic lateral growth between the bundles.

4.2.2 Synthesis of Nitrilotriacetic acid (NTA)

NTA was synthesized via a two-step process (Scheme 4.1).[12] First, the amino acid derivative H-Glu(OBzl)-OtBu (**1**) was reacted with t-butylbromoacetate in an overnight reaction to afford **2** with a 65% yield**.** Following this, the benzyl ether was deprotecting through a Pd-catalyed hydrogenation reaction, resulting in the formation of the NTA ligand, with 92% yield.

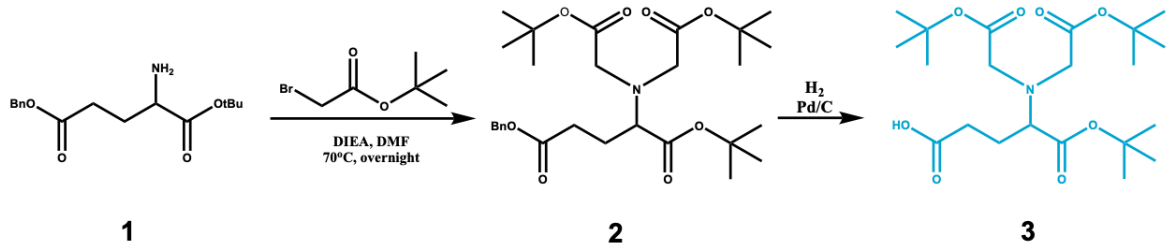

Scheme 4.1 Two-step synthesis of a protected NTA derivative

4.2.3 Synthesis of monomer **L6HCL**

The peptide **L6HCL** was synthesized using standard Fmoc-SPPS on ChemMatrix H-rink amide resin. HBTU was used as a coupling agent with two equivalents of DIEA for each amino acid. The peptide was cleaved using a TFA cocktail and was purified to homogeneity using RP-HPPLC. The peptide was characterized using MALDI-TOF mass spectrometry.

4.2.4 Helical bundle formation via cysteine-crosslinking

L6HCL was treated with excess cyanogen iodide (ICN) to deprotect the acetomidomethyl protecting groups on the homocysteine residues and simultaneously initiate the inter-helical disulfide formation (Figure 4.2).[13] After dialysis and lyophilization, the cross-linked helical bundles were separated using RP-HPLC. The cross-linking reaction resulted in six unique products, as characterized using MALDI-TOF spectrometry: three tetrameric bundles and three pentameric bundles (Figure 4.3). These compounds likely represent different isomers where the

helices are in parallel or mixed parallel-antiparallel orientations within the bundles. Based on molecular modelling of the unmodified monomer, **L6HC**, the most stable conformation would appear to be an all-parallel helical orientation due to the maximum number of salt-bridge connections.[7] The most dominant products, Tet2 and Pent2 (Figure 4.3) designated as **4HBL** and **5HBL**, respectively, were used to investigate higher-order assembly.

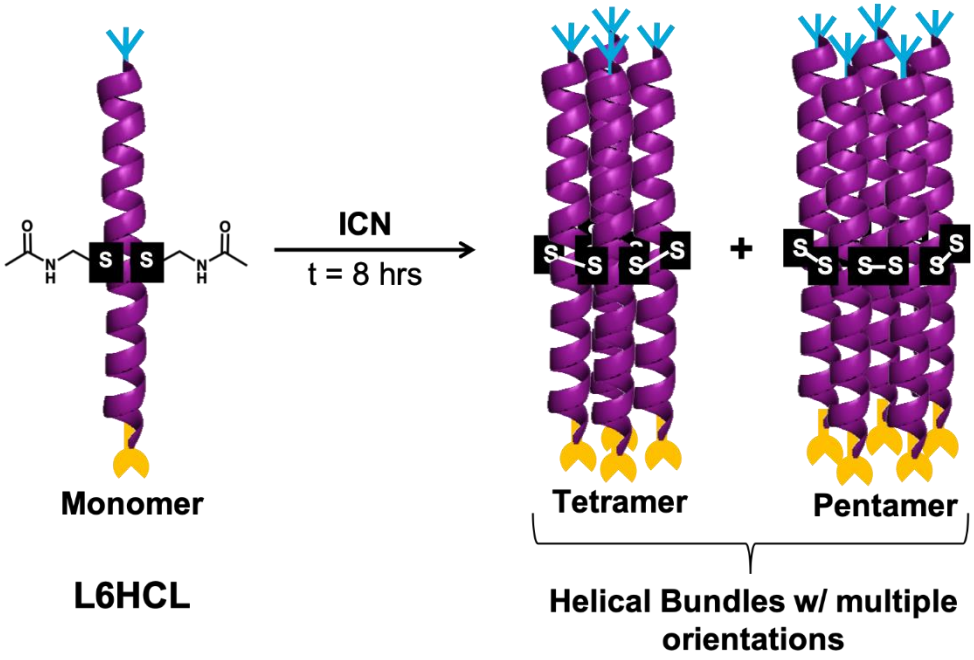

Figure 4.2 Synthesis of the cross-linked tetrameric and pentameric bundles of **L6HCL**.

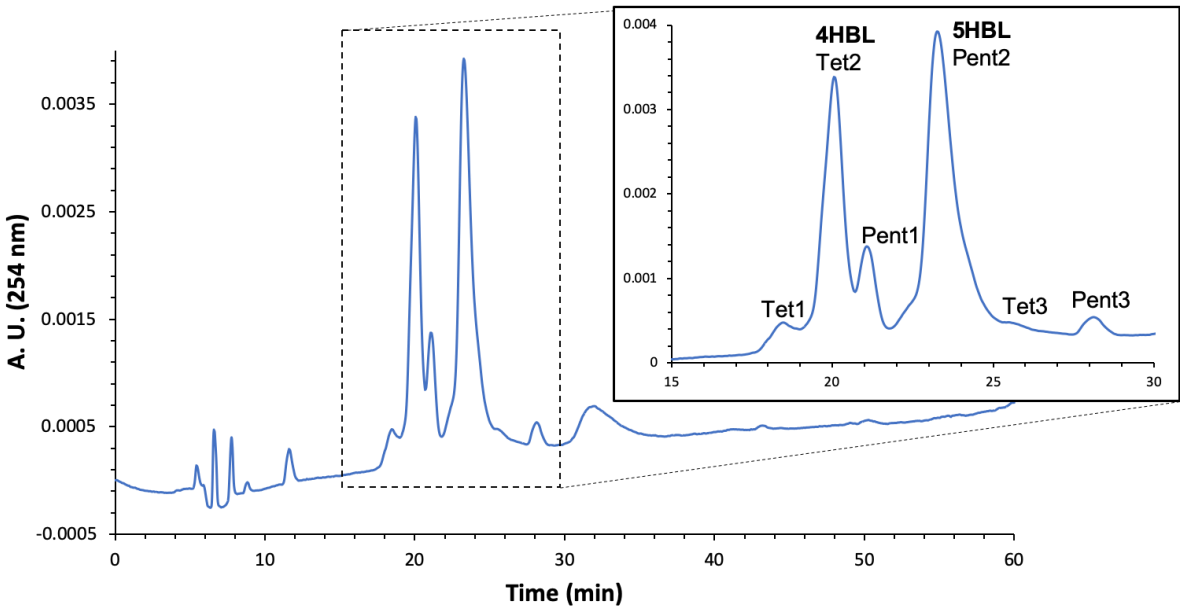

Figure 4.3 RP-HPLC separation of cross-linked tetramer and pentameric helical bundles of **L6HCL**.

4.2.5 Secondary Structure Analysis & Thermal Stability of **L6HCL**, **4HBL** and **5HBL**

The structure of **L6HCL** was investigated using circular dichroism prior to helical bundle formation. The CD spectrum displayed a helical pattern with two minima at 222 nm and 208 nm, and showed the monomer **L6HCL** (175 μM) to be 66% helical (Figure 4.4), compared to the 90% helical unmodified **L6HC**.[4] The decrease in helical content can be attributed to the addition of the NTA and di-histidine ligands at the monomer ends. The concentrations of the peptides were estimated by their weight which could further contribute to inconsistencies in observed ellipticity values, due to differing levels of sample hydration. The covalently stabilized tetramer, **4HBL** (90 μM) and pentamer, **5HBL** (75 μM) bundles also displayed alpha-helical characteristics with a helical content of 51% and 44%, respectively (Figure 4.4).

The stability of the proteins, **4HBL** and **5HBL** with respect to the temperature was investigated using circular dichroism and compared to that of the peptide monomer, **L6HCL**. There is a striking decrease in mean residue ellipticity (MRE) at 222 nm of the monomer, **L6HCL**,

with increase in temperature from 4° to 95° C, with a 53% decrease in helicity between the start and end temperatures (Figure 4.5). The MRE of **4HBL** and **5HBL** also declined with increasing temperature but were observed to be more thermally resistant with only 22% and 26% decreases in helicity, respectively (Figure 4.5). These trends in data complement the thermal stability trends obtained for the unmodified bundles of **L6HC**.[4, 7] This suggests that the homocysteine-crosslinking provides for more stable bundles in contrast to the non-crosslinked monomer. Since the peptides are covalently-attached they cannot dissociate into a fully unfolded monomer, and some residual helical content could remain even at high temperatures.

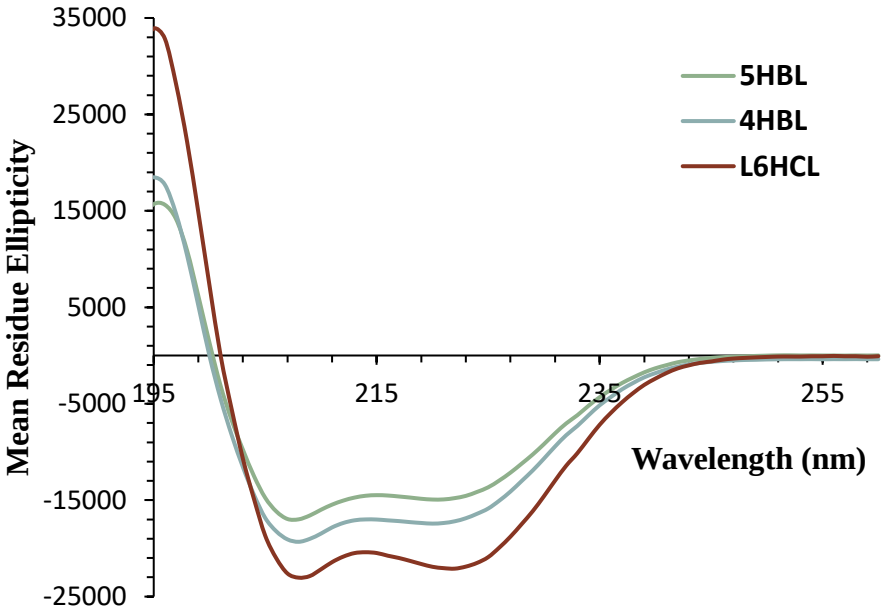

Figure 4.4 CD spectra of the helical bundles, formed by **L6HCL** (175 μM), **4HBL** (90 μM) and **5HBL** (75 μM) in 10 mM MOPS buffer (pH 7.0) at 22 °C.

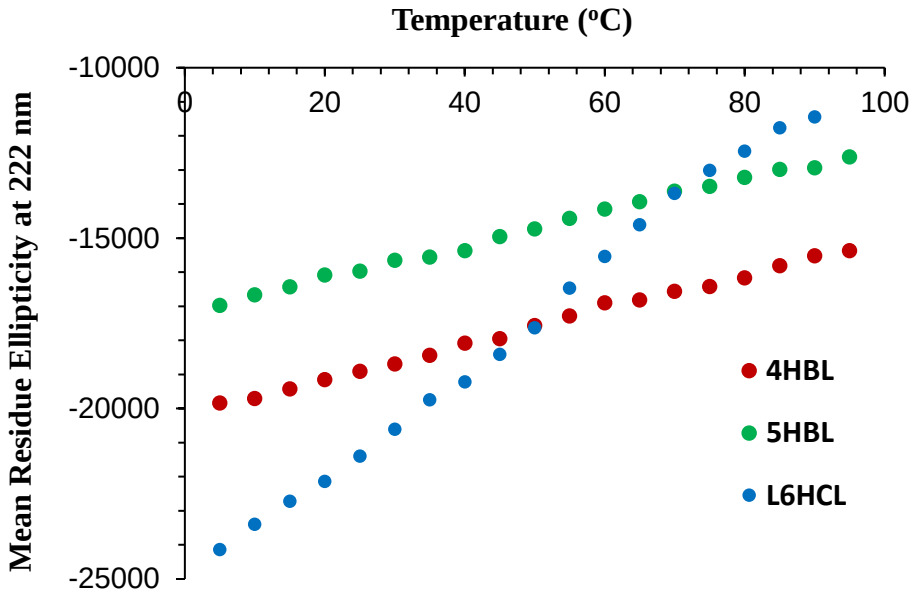

Figure 4.5 Temperature dependent helicity (MRE monitored at 222 nm) of **L6HCL** (175 μM), **4HBL** (90 μM) and **5HBL** (75 μM) in 10 mM MOPS buffer (pH 7.0).

4.2.6 Formation of helical bundle assemblies of **L6HCL**, **4HBL** and **5HBL**.

The helical bundles (1 mM in peptide unit concentration) were incubated in 25 mM MOPS buffer (pH 7.0), followed by the immediate addition of $ZnCl_2$ (2 mM) at room temperature. It is important to note that the helical bundles did not form higher-order assemblies in the absence of metal ions. With the addition of metal, the colorless precipitate that formed was collected via centrifugation and resuspended in water. These samples were visualized using scanning and transmission electron microscopies. The bundles were observed to form inter-connected globular aggregates (Figure 4.6) and there was no observable difference in the morphological nature of the assemblies formed by the four and five-helix proteins. These structures, spanning several microns, appeared to contain sphere-like entities within the material.

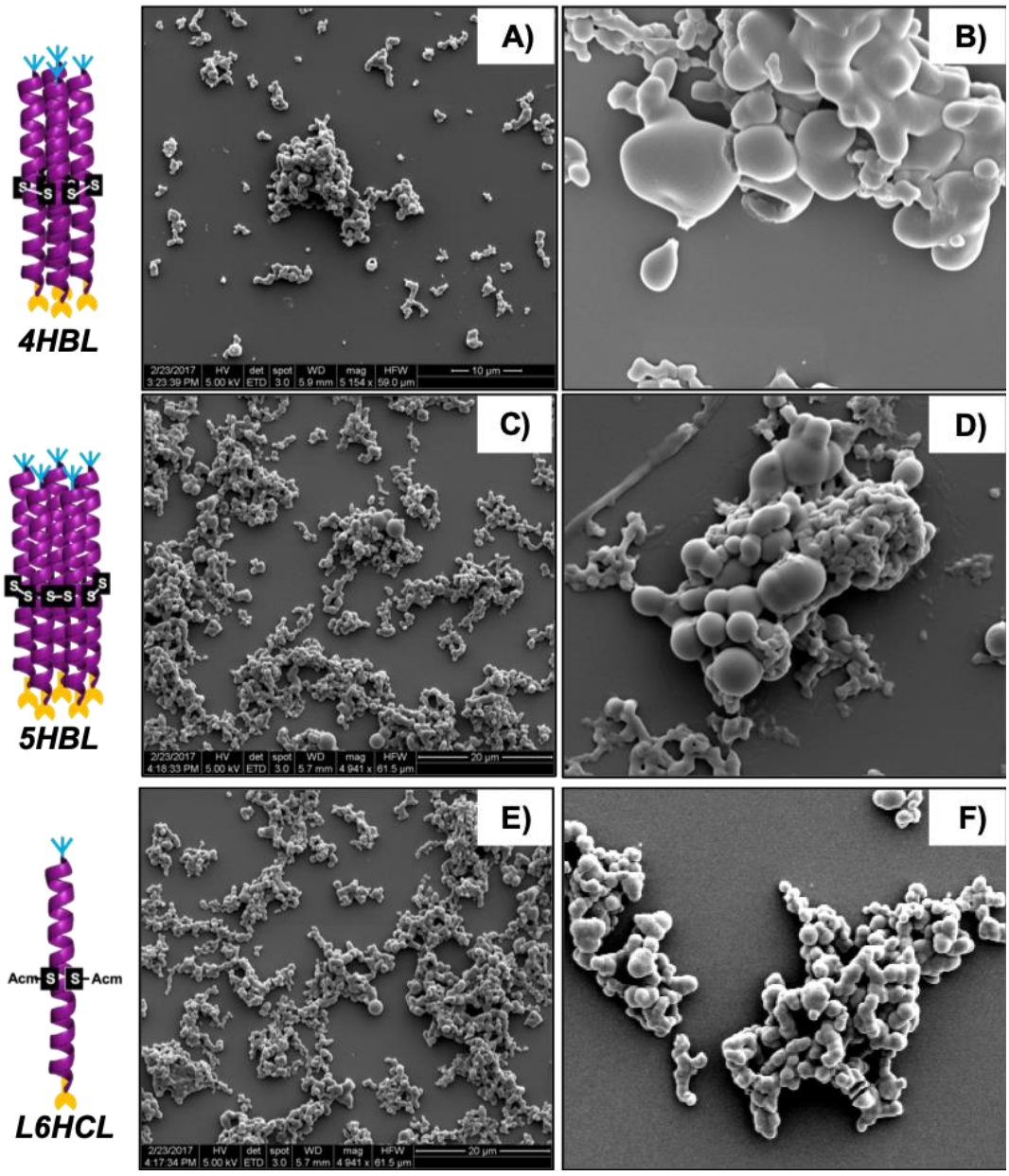

Figure 4.6 Representative SEM micrographs depicting the addition of $ZnCl_2$ (2 mM) to (A,B) **4HBL**, (C,D) **5HBL** and (E,F) **L6HCL** (1 mM peptide), in 25 mM MOPS (pH 7.0) buffer at room temperature.

Since the peptides demonstrated temperature-dependent helicity, we decided to investigate the effects of thermal annealing on the assembly conditions, in an effort to attain more defined structures. The assemblies were subject to thermal annealing, i.e., heated to 90^{o}C for 30 min and rapidly cooled to 4^{o}C. The precipitates were collected via centrifugation and washed. With thermal

annealing, **4HBL** showed no change in morphology (Figure 4.7). In contrast, **5HBL** and the non-crosslinked monomer, **L6HCL,** formed microspheres that are approximately 0.5-4 μm in diameter (Figure 4.8). The exterior of these spheres appear relatively smooth with some ridge-like folds along the surface. The TEM data (Figure 4.8 C & F) did not reveal any finer structural aspects. Instead, the images show areas of high electron density within the sphere region (opaque black color). This potentially suggests that the sphere is solid or possesses a thick outer peptide shell (see Figure 4.13).

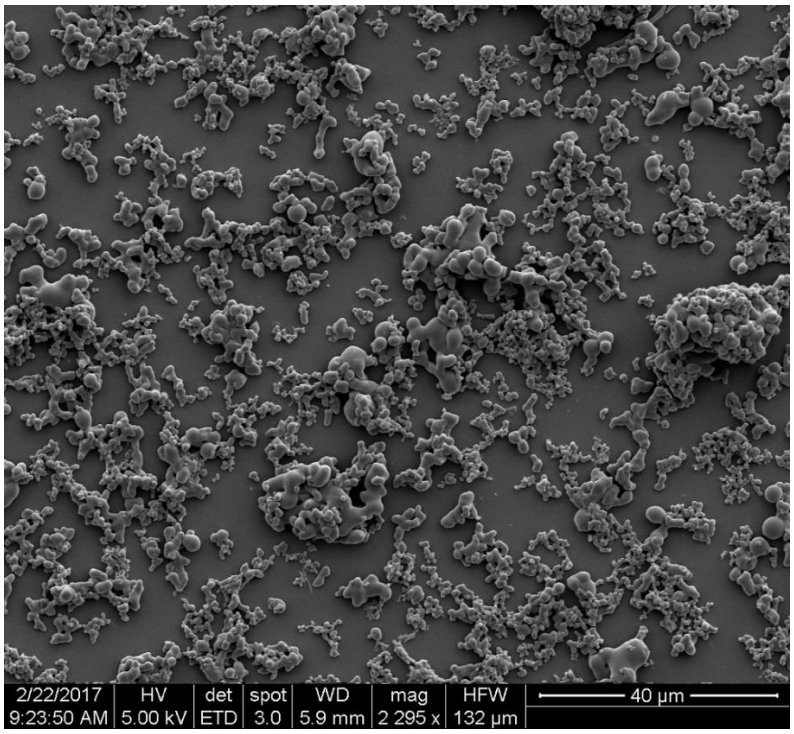

Figure 4.7 Representative SEM micrograph depicting the assembly of **4HBL** (1 mM) with Zn^{2+} (2 mM) in 25 mM MOPS (10 mM) buffer after thermal annealing.

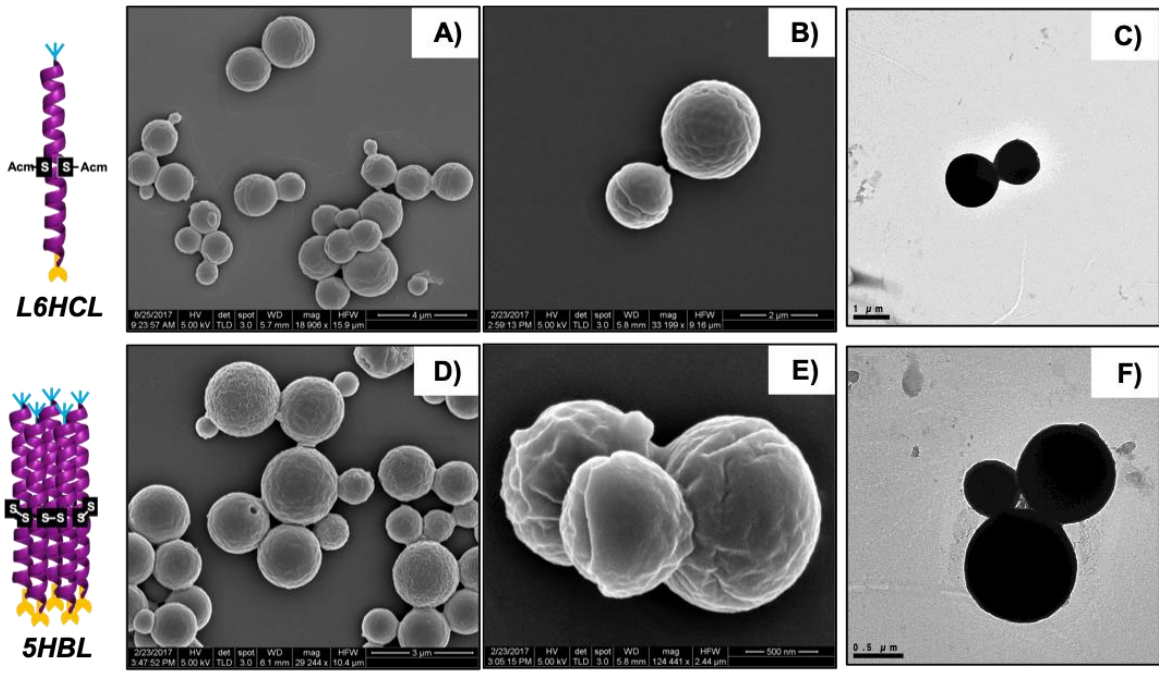

Figure 4.8 Representative SEM (A, B, D & E) and TEM (C & F) micrographs depicting the assembly of **L6HCL** (1 mM) and **5HBL** with Zn^{2+} (2 mM) in 25 mM MOPS buffer after thermal annealing.

In order to gain better insight into the mechanism of sphere formation, the effect of the peptide-metal ratio, as well as the dependence of concentration on the resulting assemblies was investigated. At a peptide:metal ratio of 1:4, 1 mM of **L6HCL** assembled into spheres, but with a broader size distribution of spheres (Figure 4.9 A-B). The diameter of the spheres ranged from 150 nm to 3 microns. At a lower peptide concentration of 0.5 mM and a peptide: metal ratio of 1:2, **L6HCL** still assembled into spheres but with the presence of a lot of amorphous aggregated material in the background (Figure 4.9 E-F). At a peptide: metal ratio of 1:1, 0.5 mM of **L6HCL** produced a sparse assembly (Figure 4.9 C-D). These data suggest that in order to form defined spheres, a minimum peptide concentration of 1 mM is required and an optimal balance between peptide and metal is necessary for a uniform size distribution of the spheres.

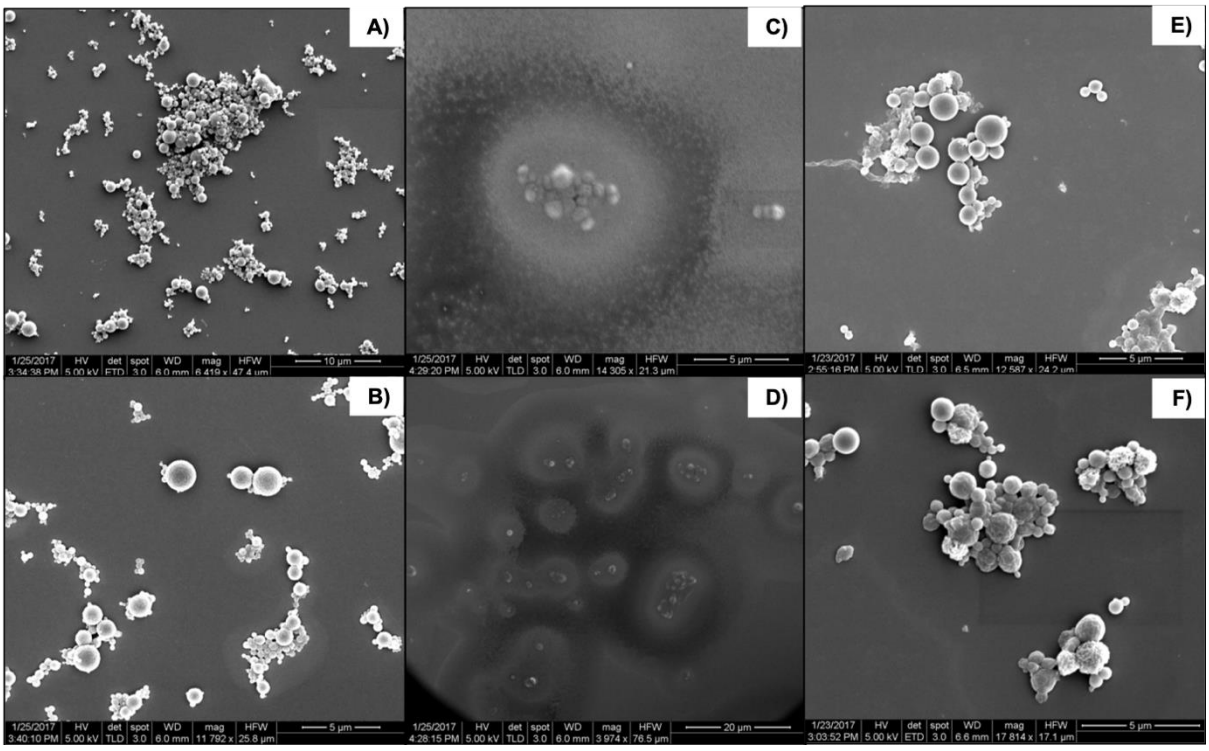

Figure 4.9 Representative SEM micrographs depicting the concentration dependence and the effect of peptide:metal ratio on the resulting assemblies. A-B) 1 mM **L6HCL** with 4 mM Zn^{2+} (1:4), C-D) 0.5 mM **L6HCL** with 0.5 mM Zn^{2+} (1:1) and, E-F) 0.5 mM **L6HCL** with 1 mM Zn^{2+} (1:2).

The possibility of assembly with other metal ions was also explored. **L6HCL** and **5HBL** (1 mM in peptide unit) formed similar spheres in the presence of Cu^{2+} ($CuCl_2$, 2 mM in 25 mM MOPS buffer) under the same annealing conditions. The copper assemblies exhibited greater polydispersity, accompanied by a few large elliptical or elongated spheres (Figure 4.10). Interestingly, metal ions such as Ni^{2+} and Co^{2+}, as well as trivalent metal ions like Gd^{3+} (preserving the same peptide:metal ratios) did not yield any visible precipitates. Dynamic light scattering (DLS) studies also verified the absence of any higher-order assembly (Figure 4.11). This potentially suggests that the arrangement of ligands at the junction of two helical bundles was not suitable for the complexation of the aforementioned metal ions.

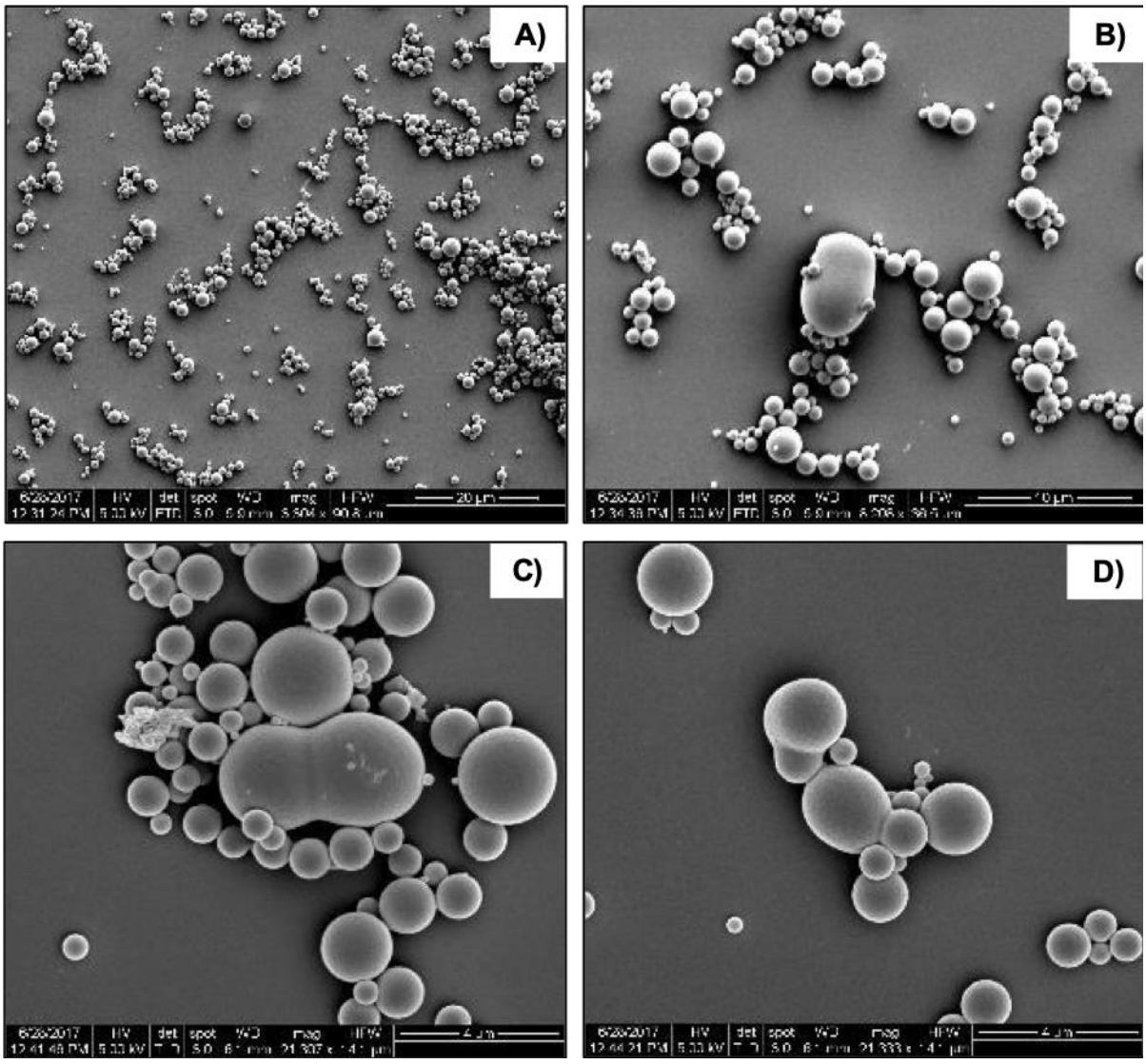

Figure 4.10 Representative scanning electron microscopy images depicting the assembly of A) & C) - **L6HCL** (1 mM) and, B) & D) **5HBL** (1 mM) with Cu^{2+} (2 mM) in 25 mM MOPS (pH 7.0) buffer after thermal annealing.

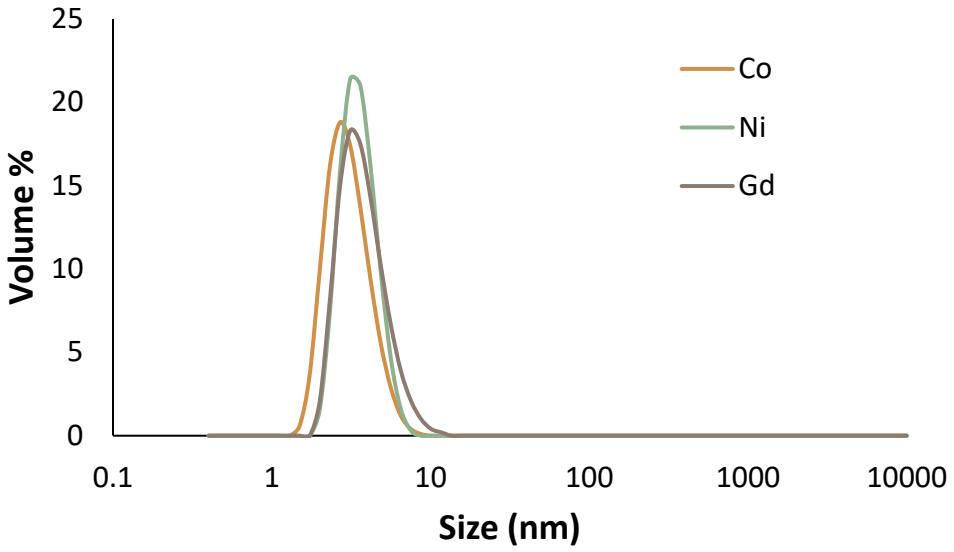

Figure 4.11 DLS size distribution plot depicting the absence of assembly with **L6HCL** (1 mM) bundles with Co^{2+}, Ni^{2+} and Gd^{3+} in MOPS buffer (10 mM).

4.2.7 Structure Elucidation of Microspheres

In order to validate the role of metal in sphere formation, preformed spheres of **5HBL** were treated with EDTA, a known metal chelator. Dynamic light scattering was used to verify the breakdown of these assemblies in the absence of metal. Pre-assembled spheres with an average size of 800 nm were treated with excess EDTA (100 mM), which resulted in the instantaneous breakdown of the assembly to a size of 3.2 nm (Figure 4.12). This value potentially corresponds to the hydrodynamic radius of the bundle in solution. Therefore, the metal plays a vital role in keeping the spherical assembly intact.

Broken spheres, resulting from accidental damage of the **5HBL** material while on the SEM stub, suggest that these spheres may not be hollow (Figure 4.13 A). However, in order to experimentally determine whether these spheres contain a hollow or solid interior, focused ion beam was used in conjunction with SEM, to mill the specimen surface via a sputtering process (Figure 4.13 B-C). There is a visible artifact as a result of the ion mill curtaining at the cutting

surface, indicated by the vertical aperiodic stripes in the image (Figure 4.13 E). This is strongly suggestive of a solid interior.

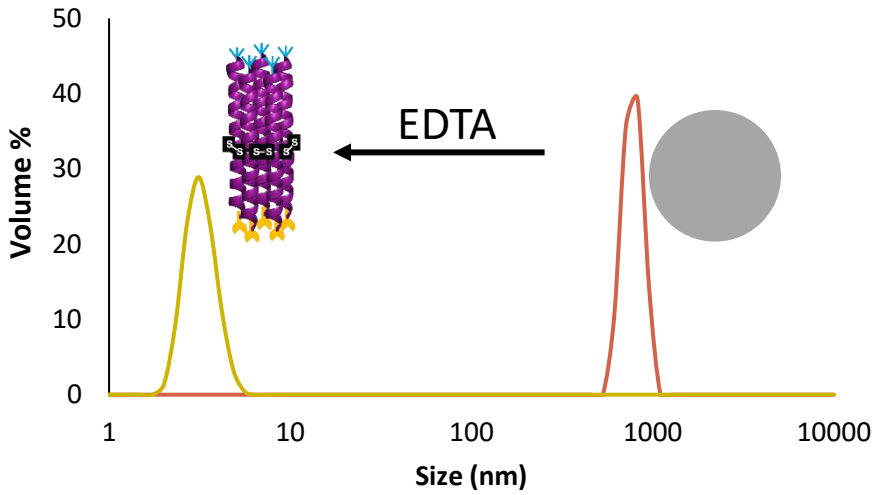

Figure 4.12 DLS size distribution plot depicting the instantaneous disassembly of the microspheres of **5HBL** (1 mM peptide in 25 mM MOPS buffer) (blue) into the protein bundles (orange) upon the addition of excess EDTA (100 mM).

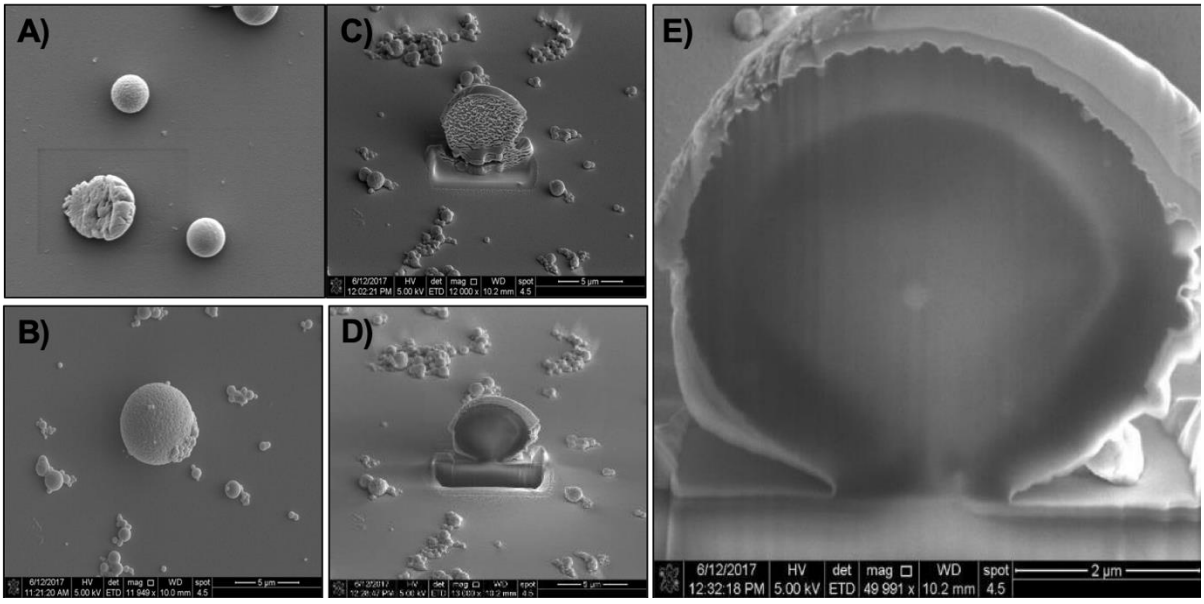

Figure 4.13 A) SEM micrograph depicting a broken **5HBL** sphere and, B-D) different FIB milling stages of a sphere with E) zoom-in of D.

In an attempt to elucidate the structure of these spheres, SWAXS analysis was employed to determine the relative packing of the **5HBL** helical bundles within the spheres. Apart from strong signals for the Kapton film (background not subtracted), the SWAXS spectrum (Figure 4.14) shows a singular moderate signal at a q value of 2.65 nm^{-1}, which corresponds to a d-spacing of 2.37 nm. Incidentally, the theoretical length of the helix bundles, estimated from molecular modelling studies, is 2.5 nm, therefore, it is reasonable to conclude that the experimentally obtained *d* spacing of 2.37 nm does represent the length of the helical bundle. There were no other discernable *d* spacings obtained even at high sample concentrations, which perhaps implies a lack of packing order within the spherical assemblies.

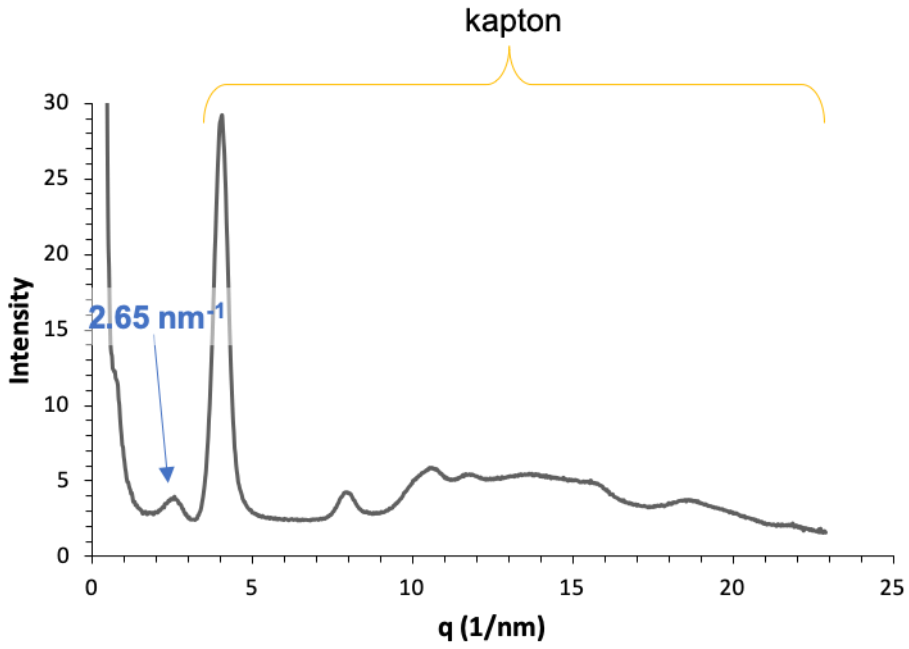

Figure 4.14 SWAXS spectrum of the **5HBL** helical bundle spheres on Kapton film with measurements taken at SDD of 113 mm.

After taking into consideration, the assessment of the SWAXS, DLS and EM data as well as the assembly conditions required for microsphere assembly of **5HBL**, we proposed the

following mechanistic hypothesis. At room temperature, the metal occupies the coordination sites located at the peptide termini, linking the helical bundles by forming head-to-tail connections. The polar faces of each bundle allow for inter-bundle electrostatic interactions, promoting lateral growth. At this stage, globular aggregates, which are kinetically trapped assemblies, are formed by the helical bundles (Figure 4.6). The elevation in temperature disrupts the interhelical electrostatic interactions and simultaneously allows for helical unfolding. During this process, the metal coordination remains intact linking the bundles to form long chains. Subsequent cooling leads to peptide re-folding and lateral re-association between the bundles. This results in the coalescing of the peptide bundle chains into spheres (Figure 4.8). The non-spherical shapes are thermodynamically not favored due to high surface energy. The formation of a sphere, however is favored as it minimizes the surface area for a fixed volume. To fabricate ordered particles at room temperature, kinetic control on the nucleation and growth of the material is necessary.[14-17] The peptide material therefore, undergoes a shape evolution which follows a kinetic-to-thermodynamic control process.

4.2.8 His-Tagged Directed Inclusion of Molecular Guests

Since the helical bundles are presumably assembled in a linear fashion, we postulated the presence of unsatisfied metal-binding ligands on the sphere surface. These ligands, aided by metal ions, could potentially be loaded with His-tagged cargo. To test this hypothesis, pre-formed spheres were treated with $NiCl_2$ (1 mM) and fluorescein-labelled hexahistidine (Fl-His_6) (0.1 mM) for 6 hours. The spheres were subsequently collected via centrifugation, washed and visualized using confocal light microscopy.

Green fluorescence was visibly associated with almost all the spheres, specifically lining the outer rim of each sphere (evident from each cross-section, Figure 4.16 A-F). This explicitly

suggests the presence of uncoordinated NTA ligands on the surface. We also observed the intermittent presence of fluorescence spread throughout the sphere material (Figure 4.16 D-E), which indicates potential diffusion of the Fl-His_6 from the outer surface into the interiors of the sphere. This diffusion of the dye is strongly indicative of the presence of unsatisfied ligands within the volume of the sphere. This is a reasonable conclusion since it has been established that the spheres are predominantly solid. To further substantiate this, we sought to incorporate the Fl-His_6 within the spherical core during the assembly of the microspheres. However, the spheres are formed from thermal annealing and Fl-His_6 is not very stable at elevated temperatures.[18] Interestingly, when the spheres were imaged dry, the consequent fluorescent signal was visible throughout the spherical bulk (Figure 4.17). It would appear that the air-drying causes some diffusion of the Fl-His_6 from the sphere surface to spread within its interior. This suggests the presence of uncoordinated NTA ligands within the interior and the outer sphere surface, further supporting the formation of solid spheres.

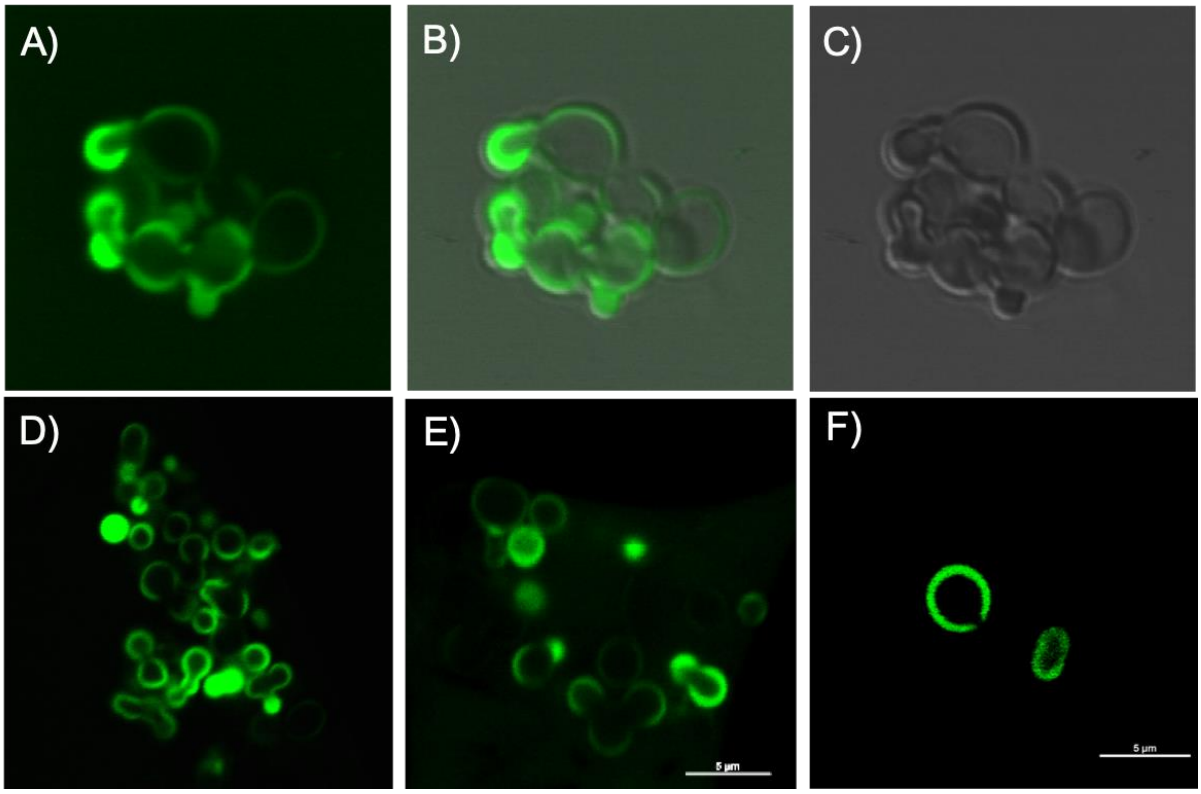

Figure 4.15 Representative confocal microscopy images of a cluster of **5HBL** helical bundle spheres (1 mM in 25 mM MOPS buffer, pH 7.0) labelled with Fl-His_6 (imaged in solution) – A) green channel, B) merged channels and C) transmitted light (TD) channel; D-F) green channel images of different clusters.

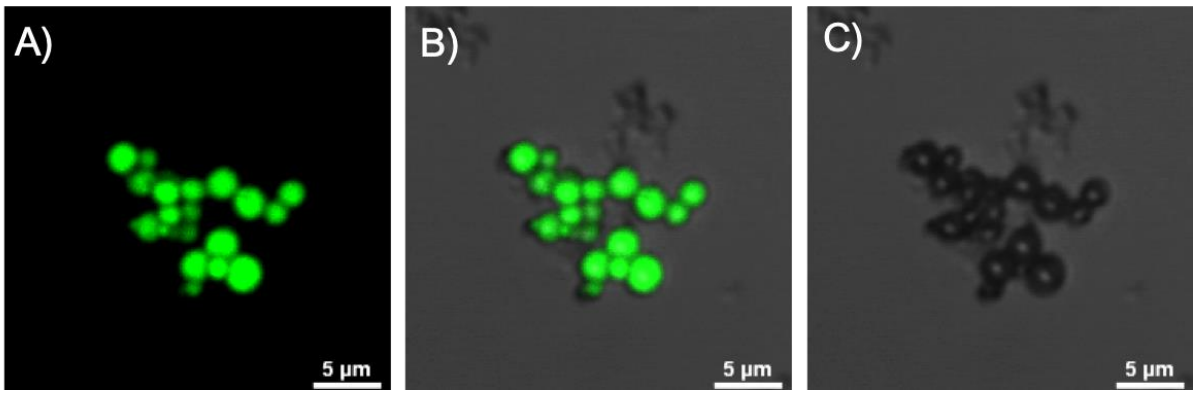

Figure 4.16 Representative confocal microscopy images of **5HBL** helical bundle spheres labelled with Fl-His_6, as above (imaged dry) - A) green channel, B) merged channels and C) transmitted light (TD) channel.

4.3 Conclusion

In summary, we have shown that the leucine-rich helical bundles, **L6HCL**, **4HBL** and **5HBL**, modified with NTA and His-His ligands at the termini, form higher-order assemblies with the addition of Zn^{2+} and Cu^{2+} metal ions. These assemblies were observed to undergo a shape evolution from nanoscale globular aggregates to solid spheres upon thermal annealing. The similar spherical morphologies obtained for both **L6HCL** and **5HBL** potentially suggests a likeness in relative alpha-helical alignment within their bundles. However, in order to verify this, further structural evidence in the form of x-ray crystallography is required. Furthermore, these spheres demonstrated the ability to incorporate His-tagged molecules on the surface of and within the spheres, which presents a versatile strategy for generating novel delivery systems. We envision that such supramolecular inclusion complexes can be further employed as bioimaging agents. Future directions include a modified design approach, with chemical modifications along the backbone of the helical bundle building-blocks, exclusively promoting lateral growth. This would allow access to the inner pore channels of the bundles, which can be harnessed for the trapping of hydrophobic molecules.

4.4 Materials and Methods

4.4.1 Materials

Fmoc-protected amino acids Fmoc-Lys(Boc), Fmoc-Leu, Fmoc-His, Fmoc-Glu(tBu), and activation agent HBTU (O-benzotriazole-N,N,N’,N’-tetramethyl-uronium-hexafluoro-phosphate) were purchased from ChemPep Inc (Wellington, Florda, USA). Fmoc-HCys(Acm) and Diisopropylethylamine (DIEA) was purchased from ChemImpex, Inc (Wood Dale, IL, USA). ChemMatrix rink amide resin was purchased from PCAS Biomatrix Inc (Saint-Jean-sur-Richelieu, Quebec, Canada). Dichloromethane (DCM), N,N-dimethylformamide (DMF), methanol (MeOH),

trifluoroacetic acid (TFA), triisopropylsilane (TIPS), hexane, ethanol, ethyl acetate, diethyl ether, tertbutyl-2-bromoacetate, H-Glu(OBzl)-OtBu and palladium on carbon (10 wt%) were purchased from Sigma-Aldrich (St. Louis, MO). Acetic anhydride was purchased from Macron Fine Chemicals. Dextran, Fluorescein (40,000 MW, anionic) and dextran, TexasRed (40,000 MW, neutral) were purchased from ThermoFisher Scientific.

4.4.2 Synthesis of Compound **2** (NTA intermediate)

Into a 500 mL round-bottom flask was placed H-Glu(OBzl)-OtBu (**1**) (15.15 mmol, 5g) 1, and DMF (100 mL). To this solution, tertbutyl-2-bromoacetate (46.96 mmol, 8 mL) and DIEA (60.6 mmol, 22.5 mL) were added with stirring and heating in an oil bath at 70 °C for 19 h. The mixture was extracted with ethyl acetate (3X), and the combined organic layers were washed with saturated LiCl (3 X 50 mL). The organic layer was dried over sodium sulfate, and the solvent was removed *in vacuo*. Purification of the residue by silica gel flash column chromatography (85:15 hexane:ethyl acetate, detection by UV on TLC) afforded **2** as a light yellow oil with 65% yield. ^{1}H NMR (300 MHz, $CDCl_3$): δ7.33 (m, 5H), δ5.11 (s, 2H), δ3.43 (s, 4H), δ3.34 (d, J = 12 Hz, 1H), δ2.62 (m, 2H), δ1.99 (m, 2H), δ1.48 (s, 27 H). ^{13}C NMR (75 MHz, $CDCl_3$): δ173.36, δ171.66, δ170.34, δ136.06, δ128.35, δ128.05, δ126.83, δ81.17, δ80.53, δ65.96, δ64.19, δ60.27, δ53.68, δ30.39, δ27.89, δ25.22.

4.4.3 Synthesis of Compound **3** (NTA derivative)

In a 250 mL round-bottom flask, compound 2 (10.2 mmol, 5.31g) was dissolved in EtOH (100 mL). To this solution was added Pd/C (0.53 g, 10% by weight). The solution was stirred under an atmosphere of H_2 for 12 h. The reaction was monitored by TLC (85:15 hexane:ethyl acetate). The solution was filtered through celite and gravity filtered to remove any remaining Pd. The solvent was removed *in vacuo*, affording the NTA derivative, **3**, as a light yellow oil with 92%

yield. ^{1}H NMR (300 MHz, $CDCl_3$): δ3.42 (s, 4H), δ3.33 (d, J = 12 Hz, 1H), δ2.56 (m, 2H), δ1.93 (m, 2H), δ1.44 (s, 27 H). ^{13}C NMR (75 MHz, $CDCl_3$): δ171.53, δ170.56, δ81.37, δ80.94, δ64.39, δ60.27, δ53.83, δ30.77, δ28.99, δ27.98, δ25.27. ESI MS Calculated: 445.55. Observed (M+1): 454.54.

4.4.4 Solid Phase Peptide Synthesis of **L6HCL**

L6HCL was synthesized using standard Fmoc protected amino acids on Chemmatrix Rink Amide resin (350 mg, 0.45 mmol/g). The desired amino acid was coupled to the free amine using HBTU (4 eq, 0.9 mmol) and DIEA (8 eq, 1.8 mmol) as coupling reagents dissolved in DMF. The mixture was added to the reaction flask containing the solid support (resin) and this was allowed to agitate for 3 hours at room temperature. After couplings, the solution was drained and the resin was washed with DMF (2 X 10 mL), DCM (2 X 10 mL), MeOH (2 X 10 mL), DCM (2 X 10 mL), and DMF (2 X 10 mL). To remove the Fmoc protecting group, the resin-bound peptide was treated with piperidine (25% in DMF, 15 mL) and reacted for 30 minutes. The piperidine solution was drained and the resin was subsequently washed with DMF, DCM, MeOH, DCM, and DMF (3 X 10 mL each). The coupling and Fmoc deprotection was monitored with the Kaiser (detection of 1° amines) test. This process was repeated until the full-length peptide was synthesized.

The resin bound peptide was then dried under reduced pressure and cleaved from resin by treatment with TFA/TIPS/H_2O (95:2.5:2.5) (15 mL) (v/v) for 2 hours. The TFA cocktail was drained into a 250 ml round bottom flask. The resin was washed twice with TFA (30 mL) and twice with DCM (30 mL). These filtrates were combined and the solvents were removed under reduced pressure. The peptide was precipitated with cold diethyl ether (50 mL). The precipitate was collected via centrifugation. The supernatant was decanted, and to this was added fresh diethyl ether (50 mL). This was centrifuged once more and again the supernatant was decanted. The pellet

was initially dried under flow of nitrogen, followed by drying *in vacuo*. After determination of the weight, the peptide was suspended in water (10 mg/mL) and purified by reverse phase (RP) HPLC on a Luna C18 (250 x 21.20 mm, 100 Å pore size, 10 micron, Phenomenex) column. Eluent conditions consisted of solvent A (CH_3CN/0.1% TFA) and solvent B (H_2O/0.1% TFA) with a 60-minute gradient of 15-90% and a flow rate of 12 mL/min monitored at wavelengths of 214 nm and 254 nm. The peptide was purified to homogeneity (Appendix: A-6) and subsequently characterized using MALDI-TOF (Appendix: A-7).

4.4.5 Cross-linking Using Cyanogen Iodide

A solution of **L6HCL** (10 mg, 4.5 μmol) in water (19 ml) was treated with ICN (68.1 mg, 445 μmol) and stirred at room temperature. The reaction was wrapped in aluminium foil and monitored using analytical HPLC over 24 hours. The solution was dialyzed against water overnight using a dialysis membrane cassette (MWCO = 3500 Da). The dialyzed solution was lyophilized and purified via RP-HPLC on a Luna C18 column (250 x 21.20 mm, 100 Å pore size, 10 micron, Phenomenex) to yield the helical bundle products. Eluent conditions consisted of solvent A (CH_3CN/0.1% TFA) and solvent B (H_2O/0.1% TFA) with a 60-minute gradient of 5-70% and a flow rate of 12 mL/min monitored at wavelengths of 214 nm and 254 nm. The helical bundles, **4HBL** and **5HBL** were isolated and purified to homogeneity (Appendix A-8) and subsequently characterized using MALDI-TOF (Appendix: A-9 and A-10).

4.4.6 Circular Dichroism Measurements

CD analyses was performed using a JASCO J-810 CD spectropolarimeter (Jasco Inc., Easton, MD), equipped with a PFD-425S Peltier temperature control unit. Samples were either suspended in 10 mM MOPS buffer. The spectra were obtained at 4 ^{o}C, obtaining an average of 3 scans for each sample between 190-260 nm at 0.1 nm data pitch with a 1 nm bandwidth. The scan rate was

100 nm/min with a 1 second response time. For the melting curves, the peptides were heated from 4 ^{o}C to 90 ^{o}C at a ramp rate of 0.5 ^{o}C/min with a data pitch of 0.2 ^{o}C, and a bandwidth of 4 nm.

4.4.7 Assembly of Spheres and Globular Aggregates

A solution of either the **L6HCL**, **4HBL** & **5HBL** (1 mM in peptide unit) was mixed with 2 mM $ZnCl_2$ in MOPS buffer (25 mM, pH 7.0) to make up a total sample volume of 100 µL. This mixture was incubated at room temperature for 3 hours, during which a precipitate formed. This precipitate was washed by centrifuging the sample at 10 g for 3 minutes, followed by the removal of the supernatant and addition of water. This process was repeated two more times for each sample, with the final suspension being in water (total sample volume of 100 µL). For annealed samples, the precipitates that formed at room temperature were heated at 90 ^{o}C for 30 minutes and allowed to cool to 4^{o}C for 12 hours, followed by the same centrifugation-based rinsing method. The above procedure was also used to test assembly with Cu(II), Ni(II), Co(II) and Gd(III) metal ions.

4.4.8 Transmission Electron Microscopy

An aliquot of the assembly in water (3.5 µL) was placed directly onto the surface of the grid. This was left to stand for 2 minutes; the water was then wicked away. The grid was rinsed through stain droplets and blotted dry. Staining was done with 2% uranyl acetate. Samples were imaged using a Tecnai T20 TEM (FEI Company, Hillsboro, OR, USA) operated at 100 KV, with a spot size of 3, 200 µm condenser aperture and 70 µm objective aperture. Images were captured using an SIA L3C 4- megapixel CCD camera (Scientific Instruments and Application, Duluth, GA). Samples were fixed on a 400-mesh copper grid coated in formvar with a carbon film (Ted Pella, Redding, CA, USA) which were previously glow discharged.

4.4.9 Scanning Electron Microscopy

Samples were prepared by placing a 5 μL aliquot of the assembly in water, on the surface of a glass cover slip adhered to the specimen stub with double sided copper tape. The samples were left to air dry prior to being coated with platinum for 60 seconds using a sputter coater. Samples were imaged using an FEI NOVA NANO SEM field emission scanning electron microscope using the Everhart-Thornley (ETD) or the high-resolution through the lens (TLD) detectors. Samples were imaged at an accelerating voltage of 5 kV with optimal working distances between 3-5 mm and a 30 μm aperture.

4.4.10 Focused Ion Beam (FIB) analysis

FIB ablation was imaged using an FEI Quanta 3D FEG scanning electron microscope (FEI Company, Hillsboro, Oregon) using ET detector and operating parameters of 5 kV, spot size 4, working distance 10 mm, 4-15K magnifications. The sample was prepared as described above and ablated with a 3 nÅ ion beam.

4.4.11 Assembly with Fl-His_6 labelling

A solution of the **5HBL** (1 mM in peptide unit) was mixed with 2 mM $ZnCl_2$ in MOPS buffer (25 mM, pH 7.0) to make up a total sample volume of 100 μL. This mixture was annealed (heated at 90 ^oC for 30 minutes and allowed to cool to 4^oC for 12 hours). The formed precipitate was washed by centrifuging the sample at 10 g for 3 minutes, followed by the removal of the supernatant and addition of water. This process was repeated two more times with final suspension containing $NiCl_2$ (1 mM) and Fl-His_6 (0.1 mM) and fresh MOPS buffer (25 mM, pH 7.0) within a sample volume of 100 μL. This was incubated for 6 hours followed by a similar centrifugation-based rinsing method outlined above, with the final suspension containing the His-tag labelled spheres in water.

4.4.12 Confocal Light Microscopy

For the fluorescent samples, a 5 μL droplet of each sample was placed on a coverslip and visualized under inverted 60x and 100x oil objectives of a Nikon AIRSi confocal microscope. Fluorescein and Texas Red were excited using 488 nm and 555 nm excitation lasers, respectively.

4.4.13 Small & Wide Angle X-ray Scattering (SWAXS)

For X-ray scattering, samples were prepared by drop-casting a 5 μL aliquot of the assembly in water on kapton tape and the measurements were performed using the Anton-Paar SAXSPoint 2.0 system operated at near-vacuum conditions with a Primux 100 micro microfocus X-ray source (Cu). Diffraction patterns were acquired with an acquisition time of 15 mins (average of 3) by means of a 2D EIGER R series Hybrid Photon Counting (HPC) detectors and High-resolution WAXS module (EIGER2 R series). Measurements were obtained at sample-detector distances of 113 mm and 79 mm.

4.5 References

1. Woolfson, D. N.; Baker, E. G.; Bartlett, G. J. How do miniproteins fold? *Science* **2017,** *357* (6347), 133-134.

2. Henchey, L. K.; Jochim, A. L.; Arora, P. S. Contemporary strategies for the stabilization of peptides in the α-helical conformation. *Curr. Opin. Chem. Biol.* **2008,** *12* (6), 692-697.

3. Makhatadze, G. I. Thermodynamics Of α-Helix Formation. *Adv. Protein Chem.* **2005,** *72*, 199-226.

4. De Vos, A. M.; Ultsch, M.; Kossiakoff, A. A. Human Growth Hormone and Extracellular Domain of its Receptor: Crystal Structure of the Complex. *Science* **1992,** *255* (5042), 306-312.

5. Powers, R.; Garrett, D. S.; March, C. J.; Frieden, E. A.; Gronenborn, A. M.; Clore, G. M. The high-resolution, three-dimensional solution structure of human interleukin-4 determined by multidimensional heteronuclear magnetic resonance spectroscopy. *Biochemistry* **1993,** *32* (26), 6744-6762.

6. Lederer, F.; Glatigny, A.; Bethge, P. H.; Bellamy, H. D.; Mathews, F. S. Improvement of the 2.5 Å resolution model of cytochrome b 562 by redetermining the primary structure and using molecular graphics. *J. Mol. Biol.* **1981,** *148* (4), 427-448.

7. Thomas, K.; Christoph, E.; James, C. S.; Bernt, K. Crystal structure of a plant catechol oxidase containing a dicopper center. *Nat. Struct. Biol.* **1998,** *5* (12), 1084-1090.

8. David, M. L.; Peter, J. A.; Stephen, J. Y.; John, M. A. S.; Livingstone, J. C.; Amyra, T.; Alessandra, L.; Sonia, L.; Paolo, A.; Gianni, C.; Christopher, D. T.; William, V. S.; Pauline, M. H. Solving the structure of human H ferritin by genetically engineering intermolecular crystal contacts. *Nature* **1991,** *349* (6309), 541-544.

9. Friedman, A. M.; Fischmann, T. O.; Steitz, T. A. Crystal structure of lac repressor core tetramer and its implications for DNA looping. *Science* **1995,** *268* (5218), 1721-1727.

10. Adrian, R. F.-D. A.; George, C. P.; Edward, B. Z.; Stephen, K. B. Recognition by Max of its cognate DNA through a dimeric b/HLH/Z domain. *Nature* **1993,** *363* (6424), 38-45.

11. Lutgring, R.; Chmielewski, J. General Strategy for Covalently Stabilizing Helical Bundles: A Novel Five-Helix Bundle Protein. *J. Am. Chem. Soc.* **1994,** *116* (14), 6451-6452.

12. Osterhout, J. J.; Connolly, P. J.; Hoch, J. C.; Handel, T.; DeGrado, W. F.; Na, G.; Toumadje, A.; Johnson, W. C.; Long, R. C.; Live, D. Characterization of the Structural Properties of α_1B, a Peptide Designed To Form a Four-Helix Bundle. *J. Am. Chem. Soc.* **1992,** *114* (1), 331-337.

13. Ho, S. P.; Degrado, W. F. Design of a 4-helix bundle protein: synthesis of peptides which self-associate into a helical protein. *J. Am. Chem. Soc.* **1987,** *109* (22), 6751-6758.

14. Degrado, W.; Wasserman, Z.; Lear, J. Protein design, a minimalist approach. *Science* **1989,** *243* (4891), 622-628.

15. Hill, C.; Anderson, D.; Wesson, L.; Degrado, W.; Eisenberg, D. Crystal Structure of alpha 1: Implications for Protein Design. *Science* **1990,** *249* (4968), 543-546.

16. Handel, T.; Degrado, W. F. De novo design of a Zn^{2+}-binding protein. *J. Am. Chem. Soc.* **1990,** *112* (18), 6710-6711.

17. Raleigh, D. P.; Degrado, W. F. A de novo designed protein shows a thermally induced transition from a native to a molten globule-like state. *J. Am. Chem. Soc.* **1992,** *114* (25), 10079-10081.

18. Raleigh, D. P.; Betz, S. F.; DeGrado, W. F. A de novo designed protein mimics the native state of natural proteins. *J. Am. Chem. Soc.* **1995,** *117* (28), 7558-7559.

19. Lutgring, R. A. The de novo design and stabilization of self-assembling helix bundle proteins and the dissociative inhibition of HIV-1 protease. Ph.D. Dissertation, Purdue University, West Lafayette, IN, 1995.

20. Nambiar, M.; Wang, L.-S.; Rotello, V.; Chmielewski, J. Reversible hierarchical assembly of trimeric coiled-coil peptides into banded nano- and micro- structures. *J. Am. Chem. Soc.* **2018,** *140* (40), 13028-13033.

21. Nepal, M.; Sheedlo, M. J.; Das, C.; Chmielewski, J., Accessing Three-Dimensional Crystals with Incorporated Guests through Metal-Directed Coiled-Coil Peptide Assembly. *J. Am. Chem. Soc.* **2016,** *138* (34), 11051-11057.

22. Nepal, M. Peptides as Tools to Develop Novel Therapeutics and Soft Materials. Ph.D. Dissertation, Purdue University, West Lafayette, IN, 2017.

23. Harbury, P. B.; Kim, P. S.; Alber, T. Crystal structure of an isoleucine-zipper trimer. *Nature* **1994,** *371*, 80-83.

24. Bryson, J.; Betz, S.; Lu, H.; Suich, D. Protein design: A hierarchic approach. *Science* **1995,** *270* (5238), 935-941.

25. Cohen, C.; Parry, D. A. D. α-Helical Coiled Coils and Bundles: How to design an α-helical protein. *Proteins: Struct. Funct., Bioinf.* **1990,** *7* (1), 1-15.

26. Murzin, A. G.; Finkelstein, A. V. General architecture of the α-helical globule. *J. Mol. Biol.* **1988,** *204* (3), 749-769.

27. Przybyla, D. E. Designer metal-triggered collagen peptides. Ph. D. Dissertation, Purdue University, West Lafayette, IN, 2010.

28. Bishop, P.; Chmielewski, J., Cyanogen iodide: A new reagent for disulfide bond formation in peptides. *Tetrahedron Lett.* **1992,** *33* (42), 6263-6266.

29. Murray, R. W. Nanoelectrochemistry: Metal nanoparticles, nanoelectrodes, and nanopores. *Chem. Rev.* **2008,** *108* (7), 2688-2720.

30. Chen, J.; Lim, B.; Lee, E. P.; Xia, Y. Shape-controlled synthesis of platinum nanocrystals for catalytic and electrocatalytic applications. *Nano Today* **2009,** *4* (1), 81-95.

31. Saha, K.; Agasti, S. S.; Kim, C.; Li, X.; Rotello, V. Gold Nanoparticles in Chemical and Biological Sensing. *Chem. Rev.* **2012,** *112* (5), 2739-2779.

32. Goubet, N.; Ding, Y.; Brust, M.; Wang, Z. L.; Pileni, M. P. A way to control the gold nanocrystals size: using seeds with different sizes and subjecting them to mild annealing. *ACS Nano* **2009,** *3* (11), 3622-3628.

33. Banks, P. R.; Paquette, D. M. Comparison of three common amine reactive fluorescent probes used for conjugation to biomolecules by capillary zone electrophoresis. *Bioconjugate Chem.* **1995,** *6* (4), 447-458.

APPENDIX A. FIGURES

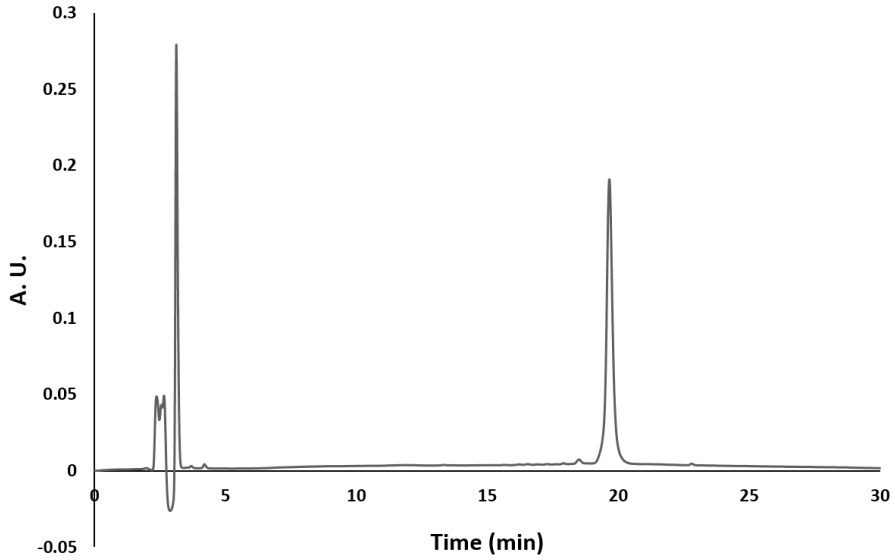

Figure A-1 Analytical chromatogram of **TriByp1** (96% purity). Eluent conditions: 20-90% MeCN/Water; Flow rate: 1.2 ml/min; Column: Luna C18 (250 x 4.60 mm, 100 Å pore size, 5 micron) Phenomenex; Monitored at λ = 214 nm.

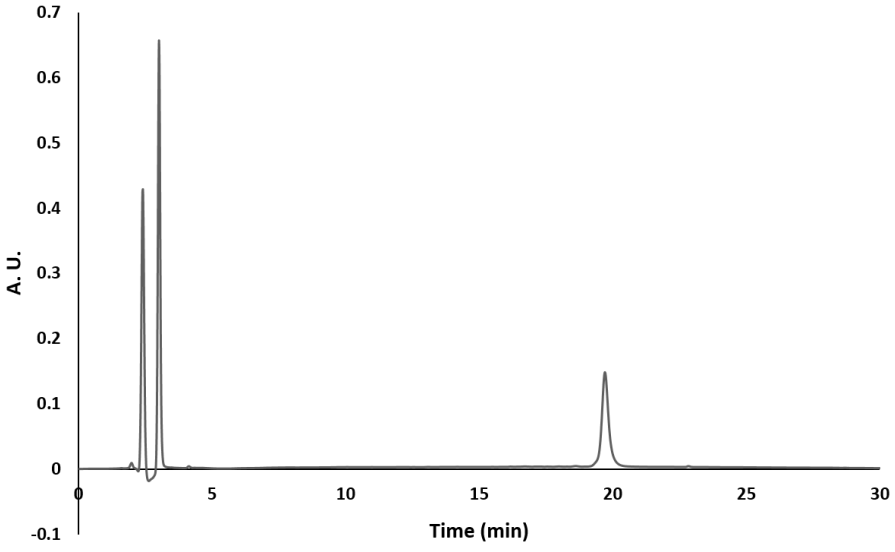

Figure A-2 Analytical chromatogram of **TriByp2** (98% purity). Eluent conditions: 20-90% MeCN/Water; Flow rate: 1.2 ml/min; Column: Luna C18 (250 x 4.60 mm, 100 Å pore size, 5 micron) Phenomenex; Monitored at λ = 214 nm.

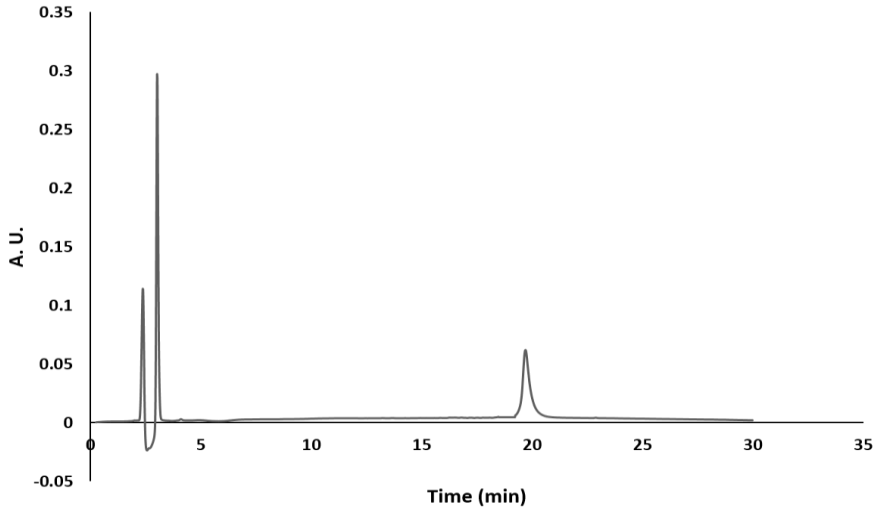

Figure A-3 Analytical chromatogram of **TriByp3** (99% purity). Eluent conditions: 20-90% MeCN/Water; Flow rate: 1.2 ml/min; Column: Luna C18 (250 x 4.60 mm, 100 Å pore size, 5 micron) Phenomenex; Monitored at λ = 214 nm.

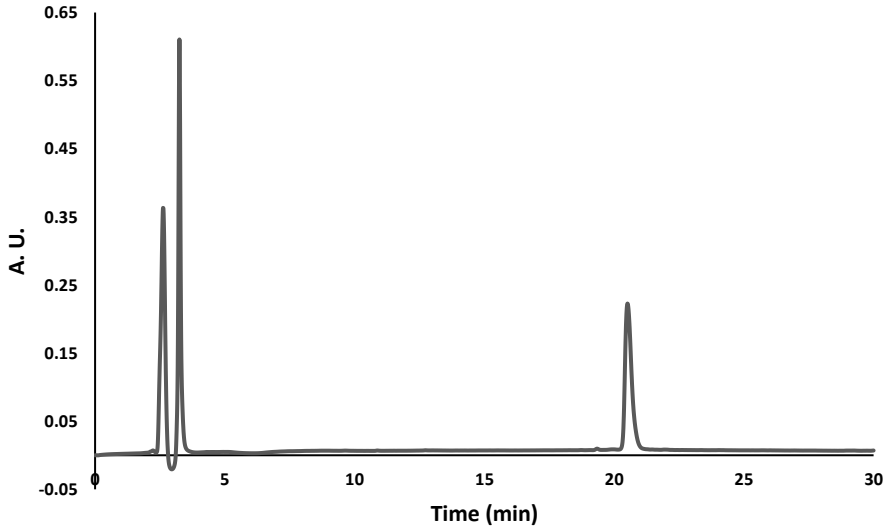

Figure A-4 Analytical chromatogram of **TriNL** (98% purity). Eluent conditions: 15-90% MeCN/Water; Flow rate: 1.2 ml/min; Column: Luna C18 (250 x 4.60 mm, 100 Å pore size, 5 micron) Phenomenex; Monitored at λ = 214 nm.

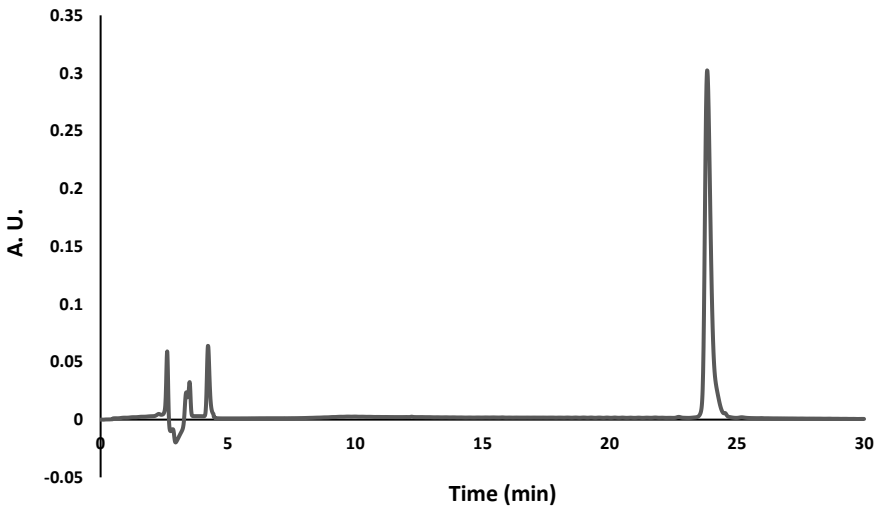

Figure A-5 Analytical chromatogram of **TetByp1** (98% purity). Eluent conditions: 5-95% MeCN/Water; Flow rate: 1.2 ml/min; Column: Luna C18 (250 x 4.60 mm, 100 Å pore size, 5 micron) Phenomenex; Monitored at λ = 214 nm.

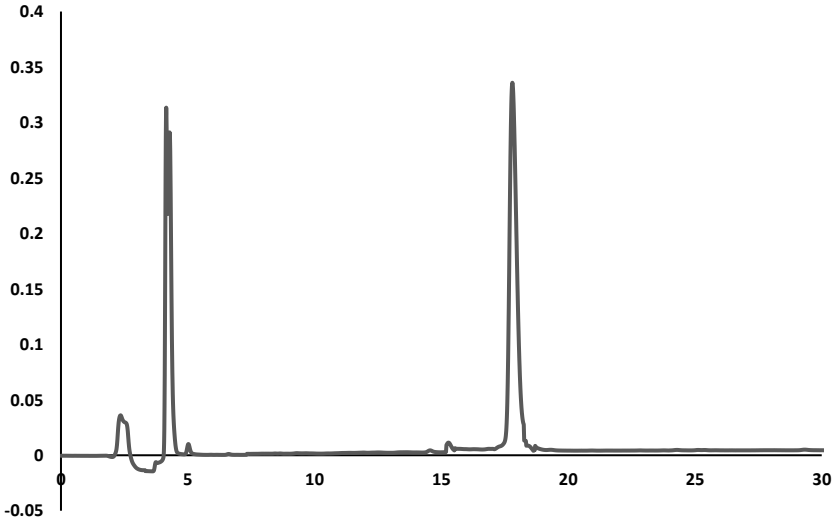

Figure A-6 Analytical chromatogram of **L6HCL** (95% purity). Eluent conditions: 15-90% MeCN/Water; Flow rate: 1.2 ml/min; Column: Luna C18 (250 x 4.60 mm, 100 Å pore size, 5 micron) Phenomenex; Monitored at λ = 214 nm.

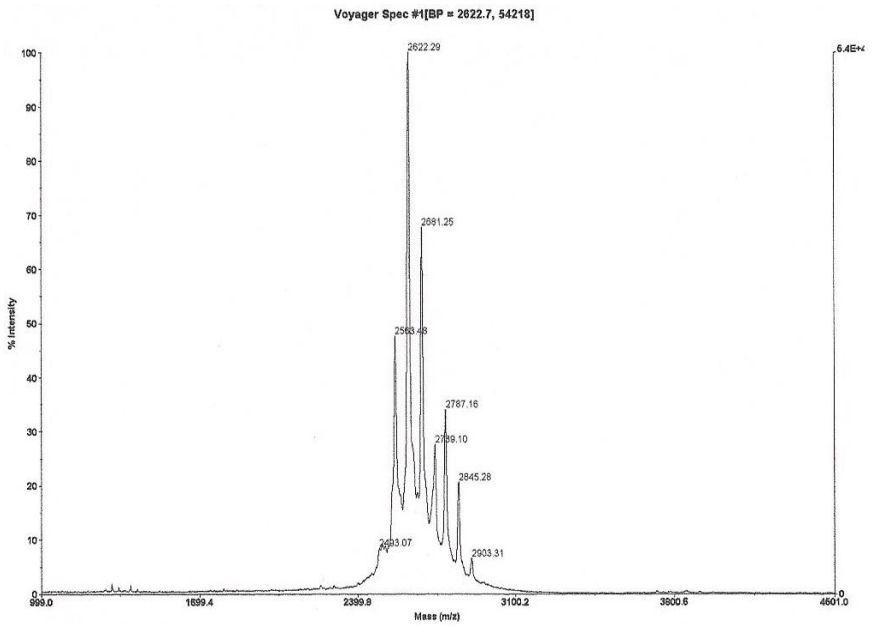

Figure A-7 MALDI-TOF spectrum of **L6HCL** (Expected mass: 2621 Da; Obtained mass: 2622 Da)

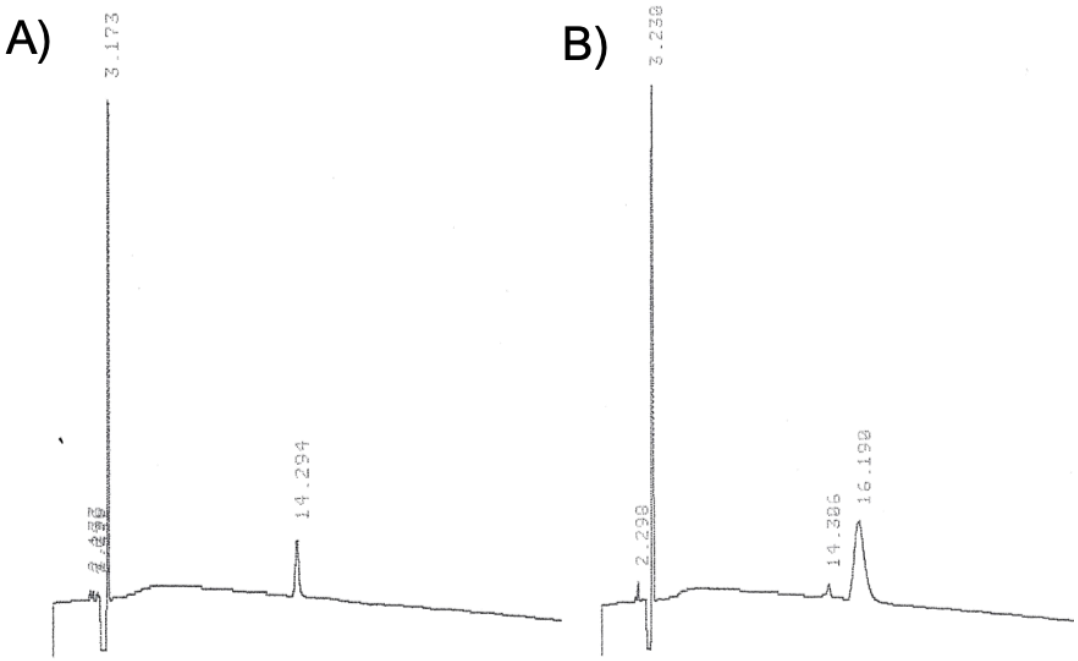

Figure A-8 Analytical chromatograms of A) **4HBL** (96% purity) and B) **5HBL** (95% purity). Eluent conditions: 5-70% MeCN/Water; Flow rate: 1.2 ml/min; Column: Luna C18 (250 x 4.60 mm, 100 Å pore size, 5 micron) Phenomenex; Monitored at λ = 214 nm.

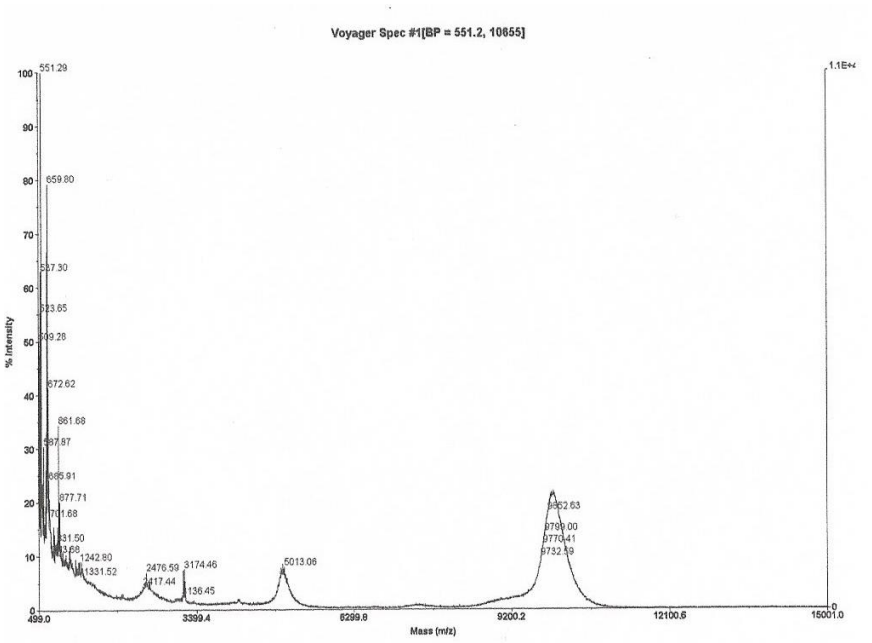

Figure A-9 MALDI-TOF spectrum of **4HBL** (Expected mass: 9907.8 Da; Obtained mass: 9852 Da)

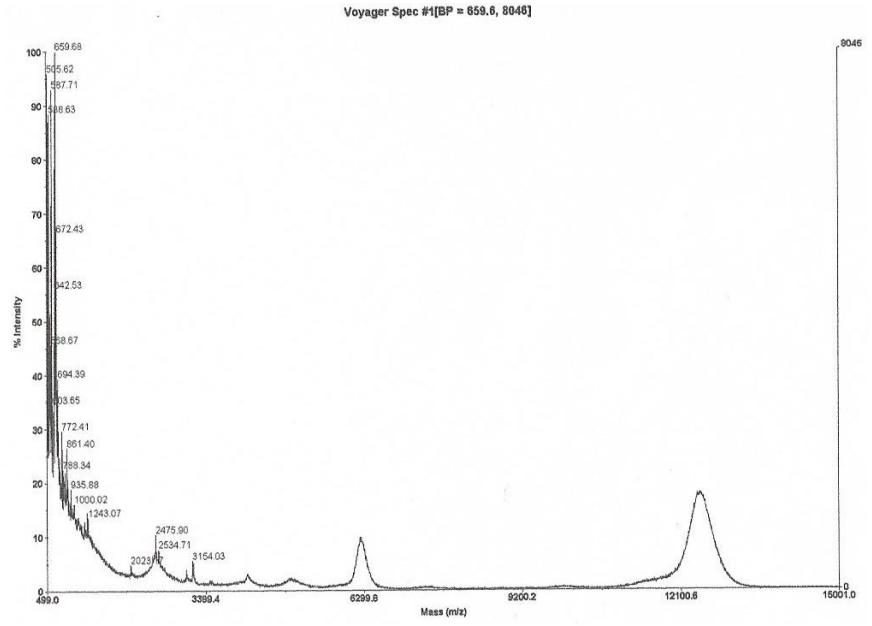

Figure A-10 MALDI-TOF spectrum of **5HBL** (Expected mass: 12384 Da; Obtained mass: 12465 Da)

VITA

Monessha was born on July 6th, 1987 in Chennai, India. She grew up in the city of Hyderabad, where she completed her schooling at the Hyderabad Public School (HPS)-Begumpet. She went on to pursue her undergraduate education at the Flinders University of South Australia. During this time, she worked with Prof. Joe Shapter on the design of carbon nanotube arrays for metal-ion detection. She commenced her graduate studies at Purdue in 2014 and joined Prof. Jean Chmielewski's lab in Spring 2015. Here, she acquired skills in peptide design, synthesis and assembly for biomaterial applications. She obtained her Doctor of Philosophy degree in September 2019 and subsequently commenced research as a postdoctoral fellow at the National Cancer Institute in Frederick, MD.

JACS JOURNAL OF THE AMERICAN CHEMICAL SOCIETY
Article
Cite This: J. Am. Chem. Soc. 2018, 140, 13028−13033
pubs.acs.org/JACS

Reversible Hierarchical Assembly of Trimeric Coiled-Coil Peptides into Banded Nano- and Microstructures

Monessha Nambiar,[†] Li-Sheng Wang,[‡] Vincent Rotello,[‡] and Jean Chmielewski*[,†]

[†]Department of Chemistry, Purdue University, 560 Oval Drive, West Lafayette, Indiana 47907-2084, United States
[‡]Department of Chemistry, University of Massachusetts−Amherst, 710 N. Pleasant Street, Amherst, Massachusetts 01002, United States

Supporting Information

ABSTRACT: We report a set of coiled-coil peptides, radially functionalized with bipyridines, that demonstrate hierarchical assembly into banded rectangular nano- and microstructures, the dimensions of which vary with the strategic placement and number of aromatic groups on the monomer backbone. Finer structural aspects of the hexagonal packing of the individual trimers were determined by X-ray scattering, including intertrimer aromatic interactions between bipyridine moieties. The ease of formation of these biomaterials under physiological conditions and the use of pH to reversibly modulate assembly demonstrate future potential for a range of biological applications, such as drug delivery in a pH-controlled manner.

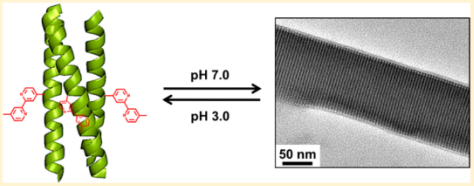

INTRODUCTION

A key attribute of synthetic biomaterials is their ability to mimic naturally occurring biological molecules and systems. The challenge, however, is to generate materials with hierarchical assemblies down to the atomic level that have precisely tailored chemical heterogeneities and external stimuli-responsiveness. Self-assembling peptides have emerged as a promising avenue for the creation of novel biomaterials. For instance, coiled-coil peptide materials comprising fibers[1−13] and hydrogels[14−24] have been described, some of which are capable of supporting cell growth and differentiation for tissue regeneration. Additionally, nanotubes,[25−29] cages,[30] films,[31] and crystals[32] have also been created for ultimate applications in drug delivery and biosensing.

Whereas the sequential building blocks of most self-assembling peptide systems are different, the hierarchical molecular assemblies are generally held together by weak intermolecular forces. These interactions can be triggered by an external stimulus[23,33−35] and are, in some instances, reversible with pH,[3,17,36,37] temperature,[14,38−47] and enzyme action.[48,49] This type of molecular control justifies the appeal of such systems for the creation of stimuli-responsive materials. A limited number of pH-switchable coiled-coil systems have been previously described, where in fibers[3] and hydrogels[17] they have exhibited reversible assembly on cue. Such materials can further be harnessed toward creating targeted therapies. Coiled-coil peptides also offer benefits that include well-established design principles, facile synthesis, and accessibility to multiple oligomeric states. Herein, we describe bipyridine-modified coiled-coil peptides that demonstrate self-assembly that can be reversibly controlled as a function of pH.

RESULTS AND DISCUSSION

Peptide Design. Our choice of peptide sequence is based on the well-studied GCN4 leucine zipper motif.[50,51] It has been established that the substitution of leucine residues with isoleucine in the *a* and *d* positions of the GCN4 sequence (Figure 1A, helical wheel diagram) affords a trimeric coiled-coil, with all three helices in a parallel orientation relative to each other.[51] We strategically placed hydrophobic groups on the polar face of the coiled-coil, in the solvent-exposed *f* position, to permit intertrimer interactions across coiled-coils. Specifically, we employed bipyridine moieties to mediate these interactions to promote higher-order assembly. The use of bipyridines enables a potential dual use of this moiety for aromatic interactions as well as enabling pH-sensitive control of assembly.

The design used in these studies features three peptide sequences, each with a varying number of bipyridines along the peptide backbone: **TriByp1**, with one bipyridine at position 13; **TriByp2**, with bipyridines at positions 13 and 20; and **TriByp3**, with bipyridines at positions 6, 13, and 20 (Figure 1B). Each of these monomers would fold into trimers with 3, 6, and 9 bipyridines, respectively. We hypothesized that with an increase in the number of bipyridines along the length of the coiled-coil, there would be a corresponding increase in the degree of radially directed intercoil interactions.

Synthesis of Bipyridine-Modified Coiled-Coil Peptides. The peptides were synthesized using Fmoc-based solid phase peptide synthesis with the ChemMatrix resin containing a Rink-amide linker. We implemented an on-resin modification

Received: July 31, 2018
Published: September 17, 2018

DOI: 10.1021/jacs.8b08163
J. Am. Chem. Soc. 2018, 140, 13028−13033

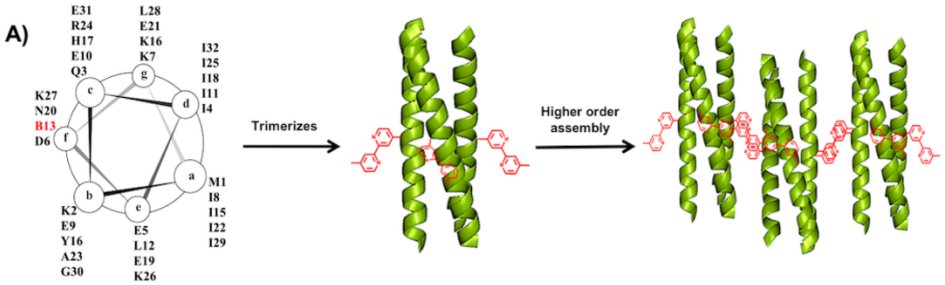

B)

Monomer	*abcdefg*	*abcdefg*	*abcdefg*	*abcdefg*	*abc*
TriByp1	Ac-MKQIEDK	IEEILBK	IYHIENE	IARIKKL	IGE-NH_2
TriByp2	Ac-MKQIEDK	IEEILBK	IYHIEBE	IARIKKL	IGE-NH_2
TriByp3	Ac-MKQIEBK	IEEILBK	IYHIEBE	IARIKKL	IGE-NH_2

B = Lysine functionalized with bipyridine

Figure 1. Design of coiled-coil peptide assembly depicting (A) helical wheel arrangement of an individual α helix leading to coiled-coil folding with subsequent higher-order assembly and (B) sequential representation of amino acids for each monomer sequence.

strategy for functionalization with the bipyridine moieties. The amino acid residues of the parent sequence, Asp 6, Ser 13, and Asn 20, were substituted with methyltrityl-functionalized lysines (Mtt-Lys). The Mtt protecting groups were selectively removed, followed by treatment with 4′-methyl-2,2′-bipyridine-4-carboxylic acid[52] and *O*-(benzotriazol-1-yl)-*N*,*N*,*N*′,*N*′-tetramethyluronium hexafluorophosphate (HBTU), to incorporate the bipyridines. The peptides were cleaved from resin with a trifluoroacetic acid cocktail, purified to homogeneity, and characterized with matrix-assisted laser desorption ionization time-of-flight (MALDI-ToF) mass spectrometry.

Structural Characterization of Bipyridine-Modified Coiled-Coils. The decoration of the coiled-coil peptides with bulky bipyridine groups could potentially disrupt their ability to fold into a helical coiled-coil trimer. To determine the secondary structure of the peptides, circular dichroism spectra were obtained, with an emphasis on the far-UV (190−250 nm) region. The CD measurement was performed at low pH (10 mM citrate buffer, pH 3.0) to avoid the possibility of assembly at higher pH values. All four peptides displayed a helical structure, indicated by the two negative absorption bands at 222 and 208 nm and a positive absorption band at 194 nm (Figure 2). It is worth noting that the magnitude of absorption at 222 nm is higher than that at 208 nm ($\theta_{222}/\theta_{208} \geq 1$), which has been shown to be indicative of the presence of a coiled-coil.[53] The level of helicity, as determined by the mean residue ellipticity value at 222 nm, was approximately 50−60% for all peptides.[54,55] The native GCN4 trimer has been shown to be about 90% helical (Figure S4),[56,57] suggesting that the incorporation of bipyridines decreases helical content, but does not preclude the formation of the α helix.

The oligomerization state of the trimers was further corroborated using sedimentation velocity analytical ultracentrifugation. Sedimentation coefficient distribution analysis indicates that the predominant oligomer (>80%) in all three peptide samples is a trimer (Figure S5). These results indicate that, despite the bipyridine functionalization of the peptides,

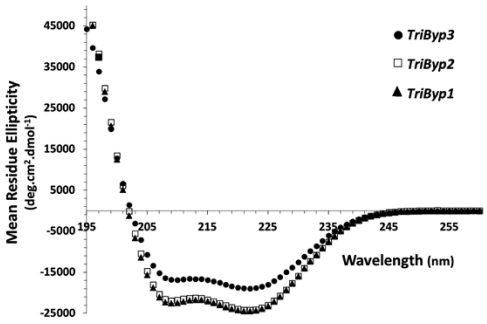

Figure 2. CD spectra of the coiled-coil peptides (100 μM) measured at pH 3.0 (10 mM citrate buffer).

the modified coiled-coil trimers maintained their structural integrity.

Formation and Visualization of the Coiled-Coil Trimer Assemblies. To achieve higher-order assembly, the peptides **TriByp1**, **TriByp2**, and **TriByp3** (250 μM) were suspended in 10 mM MOPS buffer (pH 7.0) and incubated for 48 h at room temperature. A colorless precipitate was formed in each case, which was collected by centrifugation, washed, and suspended in water. The assemblies were visualized using scanning electron microscopy (SEM) and transmission electron microscopy (TEM). The trimers were observed to collectively adopt the appearance of striated rectangular blocks (Figure 3). The striation manifests itself in a repetitive banding pattern, noticeable from the TEM data (Figure 3D−F). The banding distance, measured by performing fast Fourier transform (FFT) analysis, was 4.4 nm (Figure S6). This value was consistent across all trimer assemblies.

Varying dimensions were observed for the three different peptide assemblies with a noticeable difference in the aspect

DOI: 10.1021/jacs.8b08163
J. Am. Chem. Soc. 2018, 140, 13028−13033

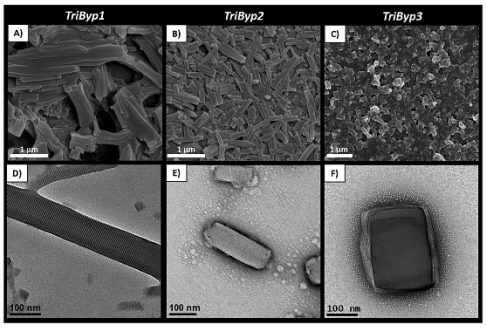

Figure 3. SEM images (A–C) and TEM micrographs (D–F) of the coiled-coil assemblies formed from **TriByp1**, **TriByp2**, and **TriByp3** (250 μM), formed in 10 mM MOPS buffer (pH 7.0) at room temperature.

ratio of these structures across the trimers. For instance, **TriByp1** assemblies containing three bipyridines per trimer (Figure 3A,D) were in the range of 30–150 nm wide (parallel to the direction of banding) and 200 nm to 4 μm in length (the direction perpendicular to the banding), with an aspect ratio (length:width) of 16:1. **TriByp2**, consisting of six bipyridines within the coiled-coil, assumed a similar morphology to **TriByp1** (Figure 3B,E), but the nanoassemblies were significantly shorter in the direction perpendicular to the banding, with the length in the range of 90–400 nm and an aspect ratio of 4:1. Correspondingly, with an increase in the number of bipyridines to nine per trimer, the **TriByp3** nanoassemblies (Figure 3C,F) displayed a slight overall decrease in length compared to **TriByp2**, but with a more significant increase in block width. Structures as wide as 300 nm were observed with the overall shape being more square-like. Thus, it is evident that with the sequential increase in the number of bipyridines from three to nine for each coiled-coil, the dimensions of the assembly change from rectangular microblocks to square-shaped nanoblocks (Table 1). This

Table 1. Dimensional Aspect Ratios and Height Measurements of the Assemblies[a]

	length (l), nm	width (w), nm	aspect ratio (l:w)	height (h), nm
TriByp1	200–4000 (n = 15)	30–150 (n = 15)	16:1	72 ± 47 (n = 5)
TriByp2	90–400 (n = 15)	45–70 (n = 15)	4:1	30 ± 20 (n = 5)
TriByp3	90–200 (n = 15)	50–300 (n = 15)	0.9:1	75 ± 35 (n = 5)

[a] n = no. of structures for which measurements were taken.

change in aspect ratio supports our initial design that a higher number of radially positioned interacting sites would have a higher propensity for individual coiled-coils to associate alongside each other (lateral assembly). For instance, enhanced lateral assembly of the trimeric coiled-coils with increased number of bipyridines was observed.

Tapping-mode atomic force microscopy (AFM) also suggests a similar morphology for the assemblies, as obtained with TEM and SEM (Figure S7). Cross-sectional analysis of the AFM images was conducted to measure the height or thickness of these structures (Table 1). The broad distribution and similar range of measured thickness across the three types of assemblies suggest a limited variation in thickness, except for a somewhat smaller height observed for the **TriByp2** nanostructures. There is definite stacking morphology that is observed in the **TriByp3** structures (Figure 3f), perhaps due to the additional bipyridine groups on the coiled-coil trimer, that is not observed with **TriByp2**.

Bipyridines are well known to chelate a variety of metal ions. Hence, arguably metal-ion coordination could potentially instigate the higher-order assembly observed. To confirm that the formation of these hierarchical structures take place in the absence of metal, the three assemblies were treated with EDTA, a metal-chelating ligand. After treatment, the assemblies remained intact with no change in morphology. Additionally, energy-dispersive X-ray spectroscopy (EDX) analysis of the nanostructures obtained with **TriByp2**, for instance, further substantiated the lack of metal ions in the assembly, with only baseline levels of metals such as iron and cobalt observed (Figure S8). The bipyridine-modified coiled-coil assemblies were also observed to be stable in the presence of metal ions and phosphate buffer conditions, without undergoing any appreciable change, thus, substantiating its potential for biological applications (Figure S9).

Structure Elucidation of Assemblies. For all three peptide assemblies, the coiled-coils are the building block for hierarchical growth. Therefore, to determine the coiled-coil packing within these assemblies, medium- and wide-angle X-ray scattering profiles (MAXS and WAXS, respectively) were obtained. In the MAXS data (Figure 4A), a peak with a q value was observed that corresponds to a d-spacing of 4.4 nm. This spacing corresponds to the length of the coiled-coil trimer as shown in Figure 4B. This spacing also corresponds to the banding distance of 4.4 nm obtained from the FFT analysis of the TEM data (Figure S6). The q value of 0.25 is also observed as the second-order signal in the TEM analysis (Figure S6). The q values 0.33, 0.58, and 0.67 Å^{-1} obtained from both the MAXS and WAXS data (Figure 4A and 4B) correspond to d-spacings of 1.85, 1.07, and 0.93 nm, respectively. Each of these represents the (100), (110), and (200) lattice planes, with a lattice parameter of 2.19 nm. These values suggest two possible packing arrangements: (i) a hexagonal close-packed (hcp) model (Figure 4D) or (ii) a hexagonal honeycomb model (Figure S10). The latter model, however, has been reported to have a larger lattice parameter (3.5 to 3.8 nm).[32,58] The small lattice parameter of 2.19 nm suggests the more compact hcp arrangement, similar to that observed for fibers formed from coiled-coil dimers (1.8 nm).[59] Sub-nanometer d-spacings of 0.5 and 0.45 nm were also obtained from the WAXS data (Figure 4B). It is possible that these values could correspond to electrostatic and cation–π interactions between adjacent coiled-coils, within the assemblies.[32]

Dynamic Light Scattering (DLS) Analysis. In the proposed hexagonal close-packed model, bipyridines and complementary charged residues in adjacent trimers would be in close proximity. The peptide assemblies have the potential to be disrupted by protonation of these groups at acidic pH. To probe if the assembly could be controlled by pH, DLS measurements of the assemblies under both acidic and neutral conditions were performed (Figure 5). At pH 7.0, the peptides suspended in 10 mM MOPS buffer exhibited higher-order assembly with hydrodynamic radii ranging from several hundred nanometers to about a micrometer. At pH 3.0 (10

DOI: 10.1021/jacs.8b08163
J. Am. Chem. Soc. 2018, 140, 13028–13033

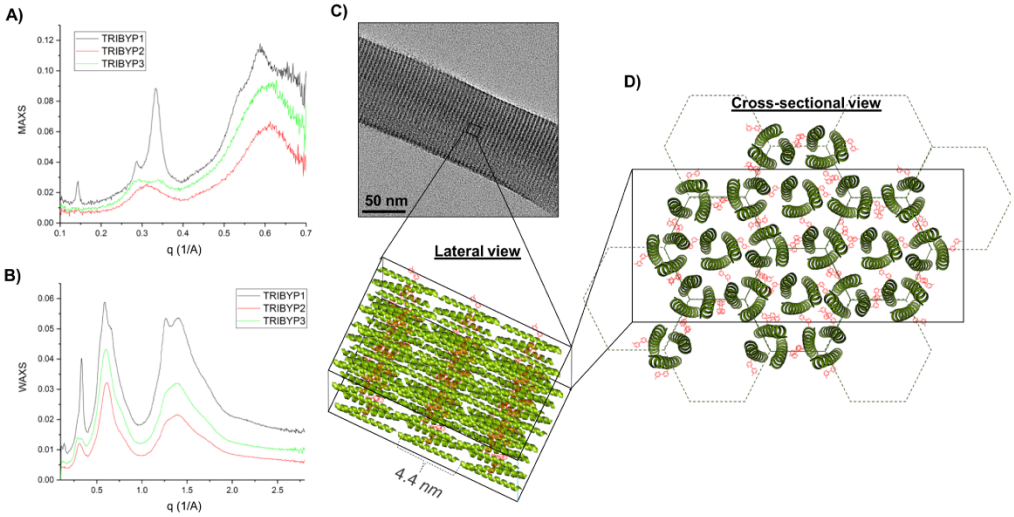

Figure 4. MAXS and WAXS analysis of the coiled-coil trimers to determine helical packing within the assemblies: (A) MAXS profile of coiled-coil trimer assemblies, (B) WAXS profile of coiled-coil trimer assemblies, (C) TEM image of **TriByp1** with inset depicting the coiled-coil trimer packing within the microstructure, and (D) cross-sectional view depicting hexagonal close-packing of coiled-coils.

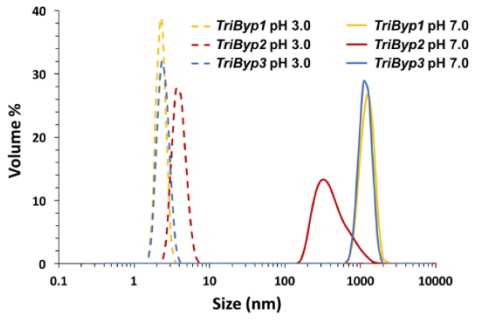

Figure 5. Dependence of modified coiled-coil peptide assembly (250 μM) on pH (10 mM MOPS, pH 7.0, and 10 mM glycine-HCl, pH 3.0).

mM glycine-HCl buffer), the hydrodynamic radius of each coiled-coil trimer was about 2−3 nm, a value that is consistent with other trimeric peptides in their unassembled state. This result may be due to protonation of the bipyridines in the more acidic environment, disfavoring trimer−trimer interactions and, thereby, perturbing higher-order assembly.

It is worth noting that these DLS measurements were acquired within minutes of initiating the assembly with buffer, which indicates that at pH 7.0 these microstructures grow rapidly. This rapid formation was further verified with TEM, which showed clear formation of well-ordered rectangular microstructures taken 2 h after initiating assembly (Figure S11). The size distribution for the **TriByp2** assemblies at pH 7.0 is relatively smaller in comparison to that of **TriByp1** and **TriByp3**. This size difference is also corroborated by the electron microscopy and AFM data for **TriByp2** assemblies, which exhibited smaller overall dimensions.

We further investigated pH as a reversible control element in a coiled-coil hierarchical assembly. We wished to probe if the assembly was reversible with pH over several cycles. As such, we monitored the change in size of the assembly by DLS, by shuttling the pH from neutral to acidic pH and back, over the course of 2 min. As an illustration, **TriByp3** was subjected to these pH changes (Figure 6). Interestingly, preformed

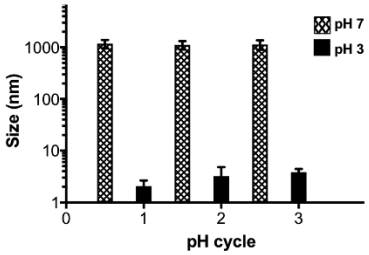

Figure 6. Reversible assembly of **TriByp3** demonstrated by repeated shuttling of pH from 7.0 to 3.0 over three cycles.

assemblies quickly reverted to monomeric coiled-coils when subjected to acidic pH. Cycling back to neutral pH allowed the assemblies to re-form, with greater than 99% sample recovery at the end of each cycle. These data demonstrate successful regeneration of the nanostructures with repeated disassembly and re-formation over three pH cycles (Figure S12).

■ CONCLUSION

In summary, coiled-coil trimers radially modified with bipyridine moieties successfully self-assembled into striated

DOI: 10.1021/jacs.8b08163
J. Am. Chem. Soc. 2018, 140, 13028−13033

micro- and nanostructures in buffer at pH 7.0. Facile modification of the coiled-coil peptides with varied number of bipyridines at the three positions provided morphological control, as demonstrated by variation in shape from rectangular to square. This is evident from the higher propensity for lateral growth observed with an increase in the number of aromatic groups, leading to wider assemblies. Additionally, nanoscale banding was also observed that corresponds to the length of the coiled-coil trimers within each assembly. Interestingly, the formation of nano- to microstructures was controlled both rapidly and reversibly as a function of pH over a number of cycles. The aromatic interactions could be harnessed to incorporate planar aromatic drugs, with delivery to cells. The ability to control assembly makes these structures attractive targets for docking a range of molecules, including pH-controlled release of therapeutics at target sites.

■ ASSOCIATED CONTENT

Supporting Information

The Supporting Information is available free of charge on the ACS Publications website at DOI: 10.1021/jacs.8b08163.

HPLC analytical chromatograms, AUC analysis, AFM images, and TEM-FFT and EDX analysis (PDF)

■ AUTHOR INFORMATION

Corresponding Author

*chml@purdue.edu

ORCID

Vincent Rotello: 0000-0002-5184-5439

Jean Chmielewski: 0000-0003-4958-7175

Notes

The authors declare no competing financial interest.

■ ACKNOWLEDGMENTS

This work was supported by the National Science Foundation through Grant 1609406-CHE. The authors thank Dr. Jia Ma of the Bindley Bioscience Facility at Purdue University for his assistance with analytical ultracentrifugation experiments and analysis.

■ REFERENCES

(1) Zhou, M.; Bentley, D.; Ghosh, I. *J. Am. Chem. Soc.* **2004**, *126*, 734.

(2) Smith, A. M.; Banwell, E. F.; Edwards, W. R.; Pandya, M. J.; Woolfson, D. N. *Adv. Funct. Mater.* **2006**, *16*, 1022.

(3) Zimenkov, Y.; Dublin, S. N.; Ni, R.; Tu, R. S.; Breedveld, V.; Apkarian, R. P.; Conticello, V. P. *J. Am. Chem. Soc.* **2006**, *128*, 6770.

(4) Tsurkan, M. V.; Ogawa, M. Y. *Biomacromolecules* **2007**, *8*, 3908−3913.

(5) Dublin, S. N.; Conticello, V. P. *J. Am. Chem. Soc.* **2008**, *130*, 49.

(6) Gribbon, C.; Channon, K. J.; Zhang, W.; Banwell, E. F.; Bromley, E. H. C.; Chaudhuri, J. B.; Oreffo, R. O. C.; Woolfson, D. N. *Biochemistry* **2008**, *47*, 10365.

(7) Papapostolou, D.; Bromley, E. H. C.; Bano, C.; Woolfson, D. N. *J. Am. Chem. Soc.* **2008**, *130*, 5124.

(8) Boyle, A. L.; Bromley, E. H. C.; Bartlett, G. J.; Sessions, R. B.; Sharp, T. H.; Williams, C. L.; Curmi, P. M. G.; Forde, N. R.; Linke, H.; Woolfson, D. N. *J. Am. Chem. Soc.* **2012**, *134*, 15457.

(9) Gunasekar, S. K.; Anjia, L.; Matsui, H.; Montclare, J. K. *Adv. Funct. Mater.* **2012**, *22*, 2154.

(10) Anzini, P.; Xu, C.; Hughes, S.; Magnotti, E.; Jiang, T.; Hemmingsen, L.; Demeler, B.; Conticello, V. P. *J. Am. Chem. Soc.* **2013**, *135*, 10278.

(11) Xu, C.; Liu, R.; Mehta, A. K.; Guerro-Ferreira, R. C.; Wright, E. R.; Dunin-Horkawicz, S.; Morris, L.; Serpell, L. C.; Zuo, X.; Wall, J. S.; Conticello, V. P. *J. Am. Chem. Soc.* **2013**, *135*, 15565.

(12) Hume, J.; Sun, J.; Jacquet, R.; Renfrew, P. D.; Martin, J. A.; Bonneau, R.; Gilchrist, M. L.; Montclare, J. K. *Biomacromolecules* **2014**, *15*, 3503.

(13) More, H. T.; Zhang, K. S.; Srivastava, N.; Frezzo, J. A.; Montclare, J. K. *Biomacromolecules* **2015**, *16*, 1210.

(14) Petka, W. A.; Harden, J. L.; McGrath, K. P.; Wirtz, D.; Tirrell, D. A. *Science* **1998**, *281*, 389.

(15) Shen, W.; Zhang, K.; Kornfield, J. A.; Tirrell, D. A. *Nat. Mater.* **2006**, *5*, 153.

(16) Xu, C.; Kopecek, J. *Pharm. Res.* **2008**, *25*, 674.

(17) Fletcher, N. L.; Lockett, C. V.; Dexter, A. F. *Soft Matter* **2011**, *7*, 10210.

(18) Huang, C. C.; Ravindra, S.; Yin, Z.; George, A. *Biomaterials* **2014**, *35*, 5316.

(19) Wang, C.; Stewart, R. J.; Kopecek, J. *Nat. Lett.* **1999**, *297*, 417.

(20) Banwell, E. F.; Abelardo, E. S.; Adams, D. J.; Birchell, M. A.; Corrigan, A.; Donald, A. M.; Kirkland, M.; Serpell, L. C.; Butler, M. F.; Woolfson, D. N. *Nat. Mater.* **2009**, *8*, 596.

(21) Kopecek, J.; Yang, J. *Angew. Chem., Int. Ed.* **2012**, *30*, 7396.

(22) Mehrban, N.; Zhu, B.; Tamagnini, F.; Young, F. L.; Wasmuth, A.; Hudson, K. L.; Thomas, A. R.; Birchall, M. A.; Randall, A. D.; Song, B.; Woolfson, D. N. *ACS Biomater. Sci. Eng.* **2015**, *1*, 431.

(23) Yao, M.-H.; Yang, J.; Du, M.-S.; Song, J.-T.; Yu, Y.; Chen, W.; Zhao, Y.-D.; Liu, Y.-D. *J. Mater. Chem. B* **2014**, *2*, 3123.

(24) Dånmark, S.; Aronsson, C.; Aili, D. *Biomacromolecules* **2016**, *17*, 2260.

(25) Jiang, T.; Xu, C.; Liu, Y.; Liu, Z.; Wall, Z. S.; Zuo, X.; Lian, T.; Salaita, L.; Ni, C.; Pochan, D.; Conticello, V. P. *J. Am. Chem. Soc.* **2014**, *136*, 4300.

(26) Burgess, N. C.; Sharp, T. H.; Thomas, F.; Wood, C. W.; Thomson, A. R.; Zaccai, N. R.; Brady, R. L.; Serpell, L. C.; Woolfson, D. N. *J. Am. Chem. Soc.* **2015**, *137*, 10554.

(27) Egelman, E. H.; Xu, C.; DiMaio, F.; Magnotti, E.; Modlin, C.; Yu, X.; Wright, E.; Baker, D.; Conticello, V. P. *Structure* **2015**, *23*, 280.

(28) Jiang, T.; Vail, O. A.; Jiang, Z.; Zuo, X.; Conticello, V. P. *J. Am. Chem. Soc.* **2015**, *137*, 7793.

(29) Thomas, F.; Burgess, N. C.l; Thomson, A. R.; Woolfson, D. N. *Angew. Chem., Int. Ed.* **2016**, *55*, 987.

(30) Fletcher, J. M.; Harniman, R. L.; Barnes, F. R.; Boyle, A. L.; Collins, A.; Mantell, J.; Sharp, T. H.; Antognozzi, M.; Booth, P. J.; Linden, N.; Miles, M. J.; Sessions, R. B.; Verkade, P.; Woolfson, D. N. *Science* **2013**, *340*, 595.

(31) Gormley, A. J.; Chandrawati, R.; Christofferson, A. J.; Loynachan, C.; Jumeaux, C.; Artzy-Schnirman, A.; Aili, D.; Yarovsky, I.; Stevens, M. M. *Chem. Mater.* **2015**, *27*, 5820.

(32) Nepal, M.; Sheedlo, M. J.; Das, C.; Chmielewski, J. *J. Am. Chem. Soc.* **2016**, *138*, 11051.

(33) Ulijn, R. V.; Smith, A. M. *Chem. Soc. Rev.* **2007**, *37*, 664.

(34) Haines, L. A.; Rajagopal, K.; Ozbas, D.; Salick, D. A.; Pochan, D. J.; Schneider, J. P. *J. Am. Chem. Soc.* **2005**, *127*, 17025.

(35) Li, X.; Gao, Y.; Kuang, Y.; Xu, B. *Chem. Commun.* **2010**, *46*, 5364.

(36) Schneider, J. P.; Pochan, D. J.; Ozbas, B.; Rajagopal, K.; Pakstis, L.; Kretsinger, J. *J. Am. Chem. Soc.* **2002**, *124*, 15030.

(37) Aggeli, A.; Bell, M.; Carrick, L. M.; Fishwick, C. W. G.; Harding, R.; Mawer, P. J.; Radford, S. E.; Strong, A. E.; Boden, N. *J. Am. Chem. Soc.* **2003**, *125*, 9619−9628.

(38) Wright, E. R.; Conticello, V. P. *Adv. Drug Delivery Rev.* **2002**, *54*, 1057.

(39) Pochan, D. J.; Schneider, J. P.; Kretsinger, J.; Ozbas, B.; Rajagopal, K.; Haines, L. *J. Am. Chem. Soc.* **2003**, *125*, 11802.

(40) Ozbas, B.; Rajagopal, K.; Haines-Butterick, L.; Schneider, J. P.; Pochan, D. *J. Phys. Chem. B* **2007**, *111*, 13901.

DOI: 10.1021/jacs.8b08163
J. Am. Chem. Soc. 2018, 140, 13028−13033

(41) Lv, S.; Cao, Y.; Li, H. *Langmuir* **2012**, *28*, 2269.
(42) Huang, H.; Ganguly, D.; Chen, J.; Sun, X. S. *J. Nanosci. Nanotechnol.* **2015**, *15*, 10598.
(43) Gleaton, J.; Chmielewski, J. *ACS Biomater. Sci. Eng.* **2015**, *1*, 1002.
(44) Luo, T.; He, L.; Theato, P.; Kiick, K. L. *Macromol. Biosci.* **2015**, *15*, 111.
(45) Luo, T.; Kiick, K. L. *J. Am. Chem. Soc.* **2015**, *137*, 15362.
(46) Huang, R. L.; Wang, Y. F.; Qi, W.; Su, R. X.; He, Z. M. *Nanoscale Res. Lett.* **2014**, *9*, 9.
(47) De Leon-Rodriguez, L. M.; Hemar, Y.; Mo, G.; Mitra, A. K.; Cornish, J.; Brimble, M. A. *Acta Biomater.* **2016**, *47*, 40.
(48) Toledano, S.; Williams, R. J.; Jayawarna, V.; Ulijn, V. *J. Am. Chem. Soc.* **2006**, *128*, 1070.
(49) Yang, Z. M.; Liang, G. L.; Wang, L.; Xu, B. *J. Am. Chem. Soc.* **2006**, *128*, 3038.
(50) Harbury, P. B.; Zhang, T.; Kim, P. S.; Alber, T. *Science* **1993**, *262*, 1401.
(51) Harbury, P. B.; Kim, P. S.; Alber, T. *Nature* **1994**, *371*, 80.
(52) Aldridge, W. S., III; Hornstein, B. J.; Serron, S.; Dattelbaum, D. M.; Schoonover, J.; Meyer, T. J. *J. Org. Chem.* **2006**, *71*, 5186.
(53) Lau, S. Y. M.; Taneja, A. K.; Hodges, R. S. *J. Bio. Chem.* **1984**, *259*, 13253−13261.
(54) Holzwarth, D.; Doty, P. *J. Am. Chem. Soc.* **1965**, *87*, 218.
(55) Greenfield, N. J. *Nat. Protoc.* **2006**, *1*, 2876.
(56) O'Shea, E. K.; Rutkowski, R.; Kim, P. S. *Science* **1989**, *243*, 538.
(57) Ciani, B.; Bjelic, S.; Honnappa, S.; Jawhari, H.; Jaussi, R.; Payapilly, A.; Jowitt, T.; Steinmetz, M. O.; Kammerer, R. A. *Proc. Natl. Acad. Sci. U. S. A.* **2010**, *107*, 19850.
(58) Lanci, C. J.; MacDermaid, C. M.; Kang, S.; Acharya, R.; North, B.; Yang, X.; Qiu, X. J.; DeGrado, W. F.; Saven, J. G. *Proc. Natl. Acad. Sci. U. S. A.* **2012**, *109*, 7304.
(59) Papapostolou, D.; Smith, A. M.; Atkins, E. D. T.; Oliver, S. J.; Ryadnov, M.G.; Serpell, L. C.; Woolfson, D. N. *Proc. Natl. Acad. Sci. U. S. A.* **2007**, *104*, 10853.

DOI: 10.1021/jacs.8b08163
J. Am. Chem. Soc. 2018, 140, 13028−13033